

# The *Herschel*<sup>★</sup> PEP/HerMES luminosity function – I. Probing the evolution of PACS selected Galaxies to $z \simeq 4$

C. Gruppioni,<sup>1†</sup> F. Pozzi,<sup>2</sup> G. Rodighiero,<sup>3</sup> I. Delvecchio,<sup>2</sup> S. Berta,<sup>4</sup> L. Pozzetti,<sup>1</sup> G. Zamorani,<sup>1</sup> P. Andreani,<sup>5</sup> A. Cimatti,<sup>2</sup> O. Ilbert,<sup>6</sup> E. Le Floch,<sup>7</sup> D. Lutz,<sup>4</sup> B. Magnelli,<sup>4</sup> L. Marchetti,<sup>3,8</sup> P. Monaco,<sup>9</sup> R. Nordon,<sup>4</sup> S. Oliver,<sup>10</sup> P. Popesso,<sup>4</sup> L. Riguccini,<sup>7</sup> I. Roseboom,<sup>10,11</sup> D. J. Rosario,<sup>4</sup> M. Sargent,<sup>7</sup> M. Vaccari,<sup>3,12</sup> B. Altieri,<sup>13</sup> H. Aussel,<sup>7</sup> A. Bongiovanni,<sup>14</sup> J. Cepa,<sup>14</sup> E. Daddi,<sup>7</sup> H. Domínguez-Sánchez,<sup>1,14</sup> D. Elbaz,<sup>7</sup> N. Förster Schreiber,<sup>4</sup> R. Genzel,<sup>4</sup> A. Iribarrem,<sup>5,15</sup> M. Magliocchetti,<sup>16</sup> R. Maiolino,<sup>17</sup> A. Poglitsch,<sup>4</sup> A. Pérez García,<sup>13</sup> M. Sanchez-Portal,<sup>13</sup> E. Sturm,<sup>4</sup> L. Tacconi,<sup>4</sup> I. Valtchanov,<sup>13</sup> A. Amblard,<sup>18</sup> V. Arumugam,<sup>11</sup> M. Bethermin,<sup>7</sup> J. Bock,<sup>19,20</sup> A. Boselli,<sup>6</sup> V. Buat,<sup>6</sup> D. Burgarella,<sup>6</sup> N. Castro-Rodríguez,<sup>14,21</sup> A. Cava,<sup>22</sup> P. Chanial,<sup>7</sup> D. L. Clements,<sup>23</sup> A. Conley,<sup>24</sup> A. Cooray,<sup>25,19</sup> C. D. Dowell,<sup>19,20</sup> E. Dwek,<sup>26</sup> S. Eales,<sup>27</sup> A. Franceschini,<sup>3</sup> J. Glenn,<sup>28,24</sup> M. Griffin,<sup>27</sup> E. Hatziminaoglou,<sup>5</sup> E. Ibar,<sup>29</sup> K. Isaak,<sup>30</sup> R. J. Ivison,<sup>29,11</sup> G. Lagache,<sup>31</sup> L. Levenson,<sup>19,20</sup> N. Lu,<sup>19,32</sup> S. Madden,<sup>7</sup> B. Maffei,<sup>33</sup> G. Mainetti,<sup>3</sup> H. T. Nguyen,<sup>20,19</sup> B. O’Halloran,<sup>23</sup> M. J. Page,<sup>34</sup> P. Panuzzo,<sup>7</sup> A. Papageorgiou,<sup>27</sup> C. P. Pearson,<sup>35,36</sup> I. Pérez-Fournon,<sup>14,21</sup> M. Pohlen,<sup>27</sup> D. Rigopoulou,<sup>35,37</sup> M. Rowan-Robinson,<sup>23</sup> B. Schulz,<sup>19,32</sup> D. Scott,<sup>38</sup> N. Seymour,<sup>34,39</sup> D. L. Shupe,<sup>19,32</sup> A. J. Smith,<sup>10</sup> J. A. Stevens,<sup>40</sup> M. Symeonidis,<sup>34</sup> M. Trichas,<sup>41</sup> K. E. Tugwell,<sup>34</sup> L. Vigroux,<sup>42</sup> L. Wang,<sup>10</sup> G. Wright,<sup>29</sup> C. K. Xu,<sup>19,32</sup> M. Zemcov,<sup>19,20</sup> S. Bardelli,<sup>1</sup> M. Carollo,<sup>43</sup> T. Contini,<sup>44</sup> O. Le Fèvre,<sup>6</sup> S. Lilly,<sup>43</sup> V. Mainieri,<sup>5</sup> A. Renzini,<sup>45</sup> M. Scodggio<sup>46</sup> and E. Zucca<sup>1</sup>

<sup>1</sup>INAF – Osservatorio Astronomico di Bologna, via Ranzani 1, I-40127 Bologna, Italy

<sup>2</sup>Dipartimento di Astronomia, Università di Bologna, via Ranzani 1, I-40127 Bologna, Italy

<sup>3</sup>Dipartimento di Astronomia, Università di Padova, vicolo dell’Osservatorio 3, I-35122 Padova, Italy

<sup>4</sup>Max-Planck-Institut für Extraterrestrische Physik (MPE), Postfach 1312, D-85741 Garching, Germany

<sup>5</sup>ESO, Karl-Schwarzschild-Strasse 2, D-85748 Garching, Germany

<sup>6</sup>Laboratoire d’Astrophysique de Marseille, CNRS-Université de Provence, rue Frédéric Joliot-Curie 38, F-13388 Marseille Cedex 13, France

<sup>7</sup>CEA-Saclay, Service d’Astrophysique, F-91191 Gif-sur-Yvette, France

<sup>8</sup>Department of Physical Sciences, The Open University, Milton Keynes MK7 6AA, UK

<sup>9</sup>Dipartimento di Fisica, Università di Trieste, Sezione di Astronomia, Via Tiepolo 11, I-34131 Trieste, Italy

<sup>10</sup>Astronomy Centre, Department of Physics and Astronomy, University of Sussex, Brighton BN1 9QH, UK

<sup>11</sup>Institute for Astronomy, University of Edinburgh, Royal Observatory, Blackford Hill, Edinburgh EH9 3HJ, UK

<sup>12</sup>Astrophysics Group, Department of Physics, University of Western Cape, Bellville 7535, Cape Town, South Africa

<sup>13</sup>ESA Herschel Science Center, Villafranca del Castillo, E-28692 Madrid, Spain

<sup>14</sup>Instituto de Astrofísica de Canarias, E-38205 La Laguna, Spain

<sup>15</sup>Observatório do Valongo, Universidade Federal do Rio de Janeiro, Brazil

<sup>16</sup>INAF–IFSI, Via Fosso del Cavaliere 100, I-00133 Roma, Italy

<sup>17</sup>Cavendish Laboratory, University of Cambridge, 19 J. J. Thomson Ave., Cambridge CB3 0HE, UK

<sup>18</sup>NASA, Ames Research Center, Moett Field, CA 94035, USA

<sup>19</sup>California Institute of Technology, 1200 E. California Blvd., Pasadena, CA 91125, USA

<sup>20</sup>Jet Propulsion Laboratory, 4800 Oak Grove Drive, Pasadena, CA 91109, USA

<sup>★</sup>*Herschel* is an ESA space observatory with science instruments provided by European-led Principal Investigator consortia and with important participation from NASA.

†E-mail: carlotta.gruppioni@oabo.inaf.it

- <sup>21</sup>Departamento de Astrofísica, Universidad de La Laguna (ULL), E-38205 La Laguna, Tenerife, Spain  
<sup>22</sup>Departamento de Astrofísica, Facultad de CC. Físicas, Universidad Complutense de Madrid, E-28040 Madrid, Spain  
<sup>23</sup>Astrophysics Group, Imperial College London, Blackett Laboratory, Prince Consort Road, London SW7 2AZ, UK  
<sup>24</sup>Center for Astrophysics and Space Astronomy 389-UCB, University of Colorado, Boulder, CO 80309, USA  
<sup>25</sup>Department of Physics and Astronomy, University of California, Irvine, CA 92697, USA  
<sup>26</sup>Observational Cosmology Lab, Code 665, NASA Goddard Space Flight Center, Greenbelt, MD 20771, USA  
<sup>27</sup>School of Physics and Astronomy, Cardiff University, Queens Buildings, The Parade, Cardiff CF24 3AA, UK  
<sup>28</sup>Department of Astrophysical and Planetary Sciences, CASA 389-UCB, University of Colorado, Boulder; CO 80309, USA  
<sup>29</sup>UK Astronomy Technology Centre, Royal Observatory, Blackford Hill, Edinburgh EH9 3HJ, UK  
<sup>30</sup>ESA Research and Scientific Support Department, ESTEC/SRE-SA, Keplerlaan 1, 2201 AZ Noordwijk, the Netherlands  
<sup>31</sup>Institut d'Astrophysique Spatiale, bâtiment 121, Université Paris-Sud 11 and CNRS (UMR 8617), F-91405 Orsay, France  
<sup>32</sup>Infrared Processing and Analysis Center, MS 100-22, California Institute of Technology, JPL, Pasadena, CA 91125, USA  
<sup>33</sup>School of Physics and Astronomy, The University of Manchester, Alan Turing Building, Oxford Road, Manchester M13 9PL, UK  
<sup>34</sup>Mullard Space Science Laboratory, University College London, Holmbury St. Mary, Dorking, Surrey RH5 6NT, UK  
<sup>35</sup>RAL Space, Rutherford Appleton Laboratory, Chilton, Didcot, Oxfordshire OX11 0QX, UK  
<sup>36</sup>Institute for Space Imaging Science, University of Lethbridge, Lethbridge, Alberta T1K 3M4, Canada  
<sup>37</sup>Department of Astrophysics, Denys Wilkinson Building, University of Oxford, Keble Road, Oxford OX1 3RH, UK  
<sup>38</sup>Department of Physics and Astronomy, University of British Columbia, 6224 Agricultural Road, Vancouver, BC V6T 1Z1, Canada  
<sup>39</sup>CSIRO Astronomy and Space Science, PO Box 76, Epping, NSW 1710, Australia  
<sup>40</sup>Centre for Astrophysics Research, University of Hertfordshire, College Lane, Hatfield, Hertfordshire AL10 9AB, UK  
<sup>41</sup>Harvard-Smithsonian Center for Astrophysics, 60 Garden Street, Cambridge, MA 02138, USA  
<sup>42</sup>Institut d'Astrophysique de Paris, UMR 7095, CNRS, UPMC Univ. Paris 06, 98bis boulevard Arago, F-75014 Paris, France  
<sup>43</sup>Institute of Astronomy, Swiss Federal Institute of Technology (ETH Hönggerberg), CH-8093 Zürich, Switzerland  
<sup>44</sup>Institut de Recherche en Astrophysique et Plantologie, CNRS, Université de Toulouse, 14 avenue E. Belin, F-31400 Toulouse, France  
<sup>45</sup>INAF Osservatorio Astronomico di Padova, vicolo dell Osservatorio 5, I-35122 Padova, Italy  
<sup>46</sup>INAF IASF Milano, via Bassini 15, I-20133 Milano, Italy

Accepted 2013 February 18. Received 2013 February 13; in original form 2012 October 23

## ABSTRACT

We exploit the deep and extended far-IR data sets (at 70, 100 and 160  $\mu\text{m}$ ) of the *Herschel* Guaranteed Time Observation (GTO) PACS Evolutionary Probe (PEP) Survey, in combination with the *Herschel* Multi-tiered Extragalactic Survey data at 250, 350 and 500  $\mu\text{m}$ , to derive the evolution of the rest-frame 35-, 60-, 90- and total infrared (IR) luminosity functions (LFs) up to  $z \sim 4$ . We detect very strong luminosity evolution for the total IR LF ( $L_{\text{IR}} \propto (1+z)^{3.55 \pm 0.10}$  up to  $z \sim 2$ , and  $\propto (1+z)^{1.62 \pm 0.51}$  at  $2 < z \lesssim 4$ ) combined with a density evolution ( $\propto (1+z)^{-0.57 \pm 0.22}$  up to  $z \sim 1$  and  $\propto (1+z)^{-3.92 \pm 0.34}$  at  $1 < z \lesssim 4$ ). In agreement with previous findings, the IR luminosity density ( $\rho_{\text{IR}}$ ) increases steeply to  $z \sim 1$ , then flattens between  $z \sim 1$  and  $z \sim 3$  to decrease at  $z \gtrsim 3$ . Galaxies with different spectral energy distributions, masses and specific star formation rates (SFRs) evolve in very different ways and this large and deep statistical sample is the first one allowing us to separately study the different evolutionary behaviours of the individual IR populations contributing to  $\rho_{\text{IR}}$ . Galaxies occupying the well-established SFR–stellar mass main sequence (MS) are found to dominate both the total IR LF and  $\rho_{\text{IR}}$  at all redshifts, with the contribution from off-MS sources ( $\geq 0.6$  dex above MS) being nearly constant ( $\sim 20$  per cent of the total  $\rho_{\text{IR}}$ ) and showing no significant signs of increase with increasing  $z$  over the whole  $0.8 < z < 2.2$  range. Sources with mass in the range  $10 \leq \log(M/M_{\odot}) \leq 11$  are found to dominate the total IR LF, with more massive galaxies prevailing at the bright end of the high- $z$  ( $\gtrsim 2$ ) LF. A two-fold evolutionary scheme for IR galaxies is envisaged: on the one hand, a starburst-dominated phase in which the Super Massive Black Holes (SMBH) grows and is obscured by dust (possibly triggered by a major merging event), is followed by an AGN-dominated phase, then evolving towards a local elliptical. On the other hand, moderately star-forming galaxies containing a low-luminosity AGN have various properties suggesting they are good candidates for systems in a transition phase preceding the formation of steady spiral galaxies.

**Key words:** galaxies: active – galaxies: evolution – galaxies: luminosity function, mass function – galaxies: starburst – cosmology: observations – infrared: galaxies.

## 1 INTRODUCTION

Understanding the origin and growth of the galaxies we observe today is one of the main problems of current cosmology. The luminosity function (LF) provides one of the fundamental tools to probe the distribution of galaxies over cosmological time, since it allows us to assess the statistical nature of galaxy formation and evolution. When computed at different redshifts, the LF constitutes the most direct method for exploring the evolution of a galaxy population, describing the relative number of sources of different luminosities counted in representative volumes of the Universe. The LF computed for different samples of galaxies can provide a crucial comparison between the distribution of different galaxy types, i.e. galaxies at different redshifts, in different environments or selected at different wavelengths.

It has now become clear that we cannot understand galaxy evolution without accounting for the energy absorbed by dust and re-emitted at longer wavelengths (i.e. Genzel & Cesarsky 2000), in the infrared (IR) or sub-millimetre (sub-mm). Dust is responsible for obscuring the ultraviolet (UV) and optical light from galaxies: since star formation (SF) occurs within dusty molecular clouds, far-IR and sub-mm data, where the absorbed radiation is re-emitted, are essential for providing a complete picture of the history of SF through cosmic time, which is one of the fundamental instruments we have to reconstruct how galaxies have evolved since their formation epoch. For these reasons, extragalactic surveys in the rest-frame IR represent a key tool for understanding galaxy formation and evolution.

Surveys of dust emission performed with the former satellites exploring the Universe in the mid- and far-IR domain, i.e. the *Infrared Astronomical Satellite* (IRAS; Neugebauer et al. 1984) and the *Infrared Space Observatory* (Kessler et al. 1996), allowed the first studies of the IR-galaxy LF at  $z \lesssim 0.3$  (Saunders et al. 1990) and  $z \lesssim 1$  (Pozzi et al. 2004), respectively. With *Spitzer* 24- $\mu\text{m}$  data, it was possible to study the evolution of the mid-IR LF up to  $z \sim 2$  (e.g. Le Floch et al. 2005; Caputi et al. 2007; Rodighiero et al. 2010a), while, even with the deepest *Spitzer Space Telescope* (Werner et al. 2004) 70- $\mu\text{m}$  data, only  $z \sim 1\text{--}1.2$  could be reached in the far-IR (Magnelli et al. 2009; Patel et al. 2013) – though Magnelli et al. (2011) reached  $z \sim 2$  through stacking. Since the rest-frame IR spectral energy distributions (SEDs) of star-forming galaxies and AGN peak at 60–200  $\mu\text{m}$ , to measure their bolometric luminosity and evolution with  $z$  we need to observe in the far-IR/sub-mm regime. However, the detection of large numbers of high- $z$  sources at the peak of their IR SED was not achievable before the *Herschel Space Observatory* (Pilbratt et al. 2010), due to source confusion and/or low detector sensitivity, and our knowledge of the far-IR LF in the distant Universe is still affected by substantial uncertainties. Ground-based and balloon-borne observations in the mm/sub-mm range, probing the evolution of the most distant ( $z \gtrsim 2$ ) and luminous dusty galaxies, have so far been limited to the identification of sources at the very bright end of the LF (e.g. Chapman et al. 2005). All of these works detected strong evolution in both luminosity and/or density, indicating that IR galaxies were more luminous and/or more numerous in the past. Strong observational evidence of high rates of evolution for IR galaxies has been obtained also through the detection of a large amount of energy contained in the Cosmic Infrared Background (CIRB; Hauser & Dwek 2001), and the source counts from several deep cosmological surveys (from 15 to 850  $\mu\text{m}$ ) largely exceeding the no-evolution expectations (e.g. Smail, Ivison & Blain 1997; Elbaz et al. 1999; Gruppioni et al. 2002; Papovich et al. 2004; Bethermin et al. 2010; Marsden et al. 2011).

Both the CIRB and the source counts require a strong increase in the IR energy density between the present time and  $z \sim 1\text{--}2$ . At higher redshifts the total emissivity of IR galaxies is poorly constrained, due to the scarcity of *Spitzer* galaxies at  $z > 2$ , the large spectral extrapolations to derive the total IR luminosity from the mid-IR (see e.g. Elbaz et al. 2010, Nordon et al. 2010, 2012 for descriptions of the failure, at least at  $z > 1.5$ , of previous total IR luminosity extrapolations from the mid-IR, although we must note that this failure mainly affects luminosity-dependent methods like, e.g., that of Chary & Elbaz 2001) and the incomplete information on the  $z$ -distribution of sub-mm sources (Chapman et al. 2005).

*Herschel*, with its 3.5-m mirror, is the first telescope which allows us to detect the far-IR population to high redshifts ( $z \sim 4\text{--}5$ ) and to derive its rate of evolution through a detailed LF analysis. The new extragalactic surveys provided by *Herschel* in the far-IR/sub-mm domain, like the wide and shallow *Herschel*-Astrophysical Terahertz Large Area Survey (ATLAS) (Eales et al. 2010; Dunne et al. 2011), the complementary *Herschel* Multi-tiered Extragalactic Survey (HerMES; Oliver et al. 2012) and PACS Evolutionary Probe (PEP; Lutz et al. 2011) covering the most popular cosmological fields, and the deep, pencil beam, *Herschel*-Great Observatories Origin Deep Survey (GOODS) project (Elbaz et al. 2011), will be crucial to assess galaxy and AGN evolution in the IR at  $z > 2$ . They will give us the opportunity to study in detail the population of IR galaxies and their evolution with cosmic time since the Universe was about a billion years old. In particular, the Photodetector Array Camera and Spectrometer (PACS; Poglitsch et al. 2010), with its high sensitivity and resolution at 70-, 100- and 160- $\mu\text{m}$ , is the best-suited instrument to detect faint IR sources by overcoming the source confusion and blending problems that affected the previous far-IR missions.

This is the first of two papers aiming at deriving the far-IR and total IR LFs from the *Herschel* PACS+Spectral and Photometric Imaging Receiver (SPIRE; Griffin et al. 2010) data obtained within the PEP and HerMES extragalactic survey projects. In this paper, we derive the rest-frame 35-, 60-, 90- and total IR (8–1000  $\mu\text{m}$ ) LFs from a sample selected at PACS 70, 100 and 160  $\mu\text{m}$  wavelengths in the GOODS (GOODS-S and GOODS-N), Extended Chandra Deep Field South (ECDFS) and Cosmic Evolution Survey (COSMOS) areas. We use the full 70–500  $\mu\text{m}$  PACS+SPIRE data to determine  $L_{\text{IR}}$  and SED properties of the PACS-selected sources. In a related paper, Vaccari et al. (in preparation) derive rest-frame 100-, 160- and 250- $\mu\text{m}$  and total IR LFs for a SPIRE-selected sample. In addition, a third work aimed at studying the total IR LF based on the 24- $\mu\text{m}$ -selected sample, using all the PEP+HerMES data in the COSMOS field, is ongoing (Le Floch et al., in preparation).

PEP is one of the major *Herschel* Guaranteed Time extragalactic key-projects, designed specifically to determine the cosmic evolution of dusty SF and of the IR LF. It is structured as a ‘wedding cake’, based on four different layers covering different areas to different depths at 100 and 160  $\mu\text{m}$  (in the GOODS-S field also at 70  $\mu\text{m}$ ), from the large and shallow COSMOS field to the deep, pencil beam GOODS-S field. PEP includes the most popular and widely studied extragalactic fields with extensive multiwavelength coverage available, in particular deep optical, near-IR and *Spitzer* imaging and spectroscopic and photometric redshifts: COSMOS, Lockman Hole, Extended Groth Strip, ECDFS, GOODS-N and GOODS-S (see Berta et al. 2010, 2011 and Lutz et al. 2011 for a detailed description of the fields and observations). Coordinated observations of the PEP fields at 250, 350 and 500  $\mu\text{m}$  with SPIRE have been obtained by the HerMES (Oliver et al. 2012). HerMES, analogously to PEP but extending to a much wider area, is a legacy

programme designed to map a set of nested fields ( $\sim 380 \text{ deg}^2$  in total) of different sizes and depths, using SPIRE (at 250, 350 and 500  $\mu\text{m}$ ), and PACS (at 100 and 160  $\mu\text{m}$ , shallower than PEP), with the widest component of 270  $\text{deg}^2$  with SPIRE alone. In the fields covered by PEP, the two surveys are closely coordinated to provide an optimized sampling over wavelength.

In Gruppioni et al. (2010), we started to determine the evolution with redshift of the galaxy and AGN LF in the far-IR domain by exploiting the PEP data obtained in GOODS-N by the PEP Science Demonstration Programme (SDP). Here, we extend the analysis to the wider and shallower fields – COSMOS and ECFDS – and to the deepest field – GOODS-S – observed by PEP, and we also take advantage of the HerMES sub-mm data in the same fields to derive improved SED classifications and accurate total IR luminosities for our sources. This allows us to have statistically significant samples of IR galaxies at different redshifts and over a broad range of luminosities, to make a detailed study of the LF at several  $z$  intervals, all the way from  $z = 0$  to  $z \simeq 4$ . The measure of the total IR luminosity obtained by integrating the SEDs, well constrained over the entire mid-IR and far-IR domain (and also in the sub-mm thanks to the available SPIRE data), allows us to derive the total IR LF and its evolution directly from far-IR data for unbiased samples selected at wavelengths close to the peak of dust emission. Moreover, the availability of deep multiwavelength catalogues in the PEP fields is crucial for analysing the SEDs, obtaining  $k$ -corrections and total IR luminosities, and classifying the PEP sources into different IR populations, in order to separately study their LFs and evolutionary behaviour. This is the first study ever based on such a statistically wide and deep far-IR sample, to be able to provide LFs for different IR populations of galaxies and AGN. Here, the evolution of the far-IR and total IR LFs (and luminosity density, hereafter  $\rho_{\text{IR}}$ ) is derived up to unprecedented high redshifts ( $\sim 4$ ) both globally (e.g. for all the populations together) and separately, for each SED class.

Despite the abundance of information available in the literature about the stellar mass function (MF; Fontana et al. 2004; Pozzetti et al. 2010; Ilbert et al. 2010; Dominguez-Sanchez et al. 2011), very little is known about the corresponding total IR LFs and SF rate (SFR) densities at different masses (an attempt based on *Spitzer* data was made by Pérez-González et al. 2005). From stellar MF studies, one finds a clear increase with  $z$  of the relative fraction of massive [ $\log(M/M_{\odot}) > 11$ ] star-forming objects, starting to contribute significantly to the massive-end of the MFs at  $z > 1$  (Fontana et al. 2004; Ilbert et al. 2010). Their evolution and contribution to the total SFR history are however still uncertain, since only a few studies have tried to reconstruct the evolution of the SF history of massive objects from optical/near-IR or mid-IR surveys (Juneau et al. 2005; Pérez-González et al. 2005; Santini et al. 2009; Fontanot et al. 2012) but none from far-IR-selected surveys (providing a more direct indicator of the galaxy SF activity). In this work, we have derived the IR LF and density in three different mass ranges [from  $\log(M/M_{\odot}) = 8.5$  to  $\log(M/M_{\odot}) = 12$ ], extending previous studies (limited to  $z = 1.8$ – $2$  for the most massive galaxies) to  $z \sim 4$ .

Finally, our PEP data sets have allowed us to quantify the relative contribution of the two main modes of SF (a relatively steady one in disc-like galaxies, defining a tight SFR–stellar mass sequence, and a starburst mode in outliers) to the total IR LF and  $\rho_{\text{IR}}$  in three redshift intervals ( $0.8 < z < 1.25$ ,  $1.25 < z < 1.8$  and  $1.8 < z < 2.2$ ) and to test the SED-classes belonging to each mode.

This paper is structured as follows. The PEP Survey with the far-IR and multiwavelength data, together with the SED characterization and redshift distribution of the PEP sources, are described in Section 2. The LFs (rest-frame 35-, 60-, 90- $\mu\text{m}$  and total IR) and

their evolution [derived for different SED-classes, mass and specific SFR (sSFR) intervals] are discussed in Section 3. In Section 4, we present the number and IR luminosity densities of the different galaxy types, while in Section 5, we discuss our results. In Section 6, we present our conclusions.

Throughout this paper, we use a Chabrier initial mass function (IMF) and we assume a  $\Lambda$  cold dark matter cosmology with  $H_0 = 71 \text{ km s}^{-1} \text{ Mpc}^{-1}$ ,  $\Omega_m = 0.27$  and  $\Omega_{\Lambda} = 0.73$ .

## 2 THE DATA

The PEP fields where we computed the LFs are COSMOS, 2  $\text{deg}^2$  observed down to  $3\sigma$  depths of  $\sim 5$  and 10.2 mJy at 100 and 160  $\mu\text{m}$ , respectively; ECFDS,  $\sim 700 \text{ arcmin}^2$  down to  $3\sigma$  depths of  $\sim 4.5$  and 8.5 mJy at 100 and 160  $\mu\text{m}$ , respectively; GOODS-N,  $\sim 300 \text{ arcmin}^2$  to 3 and 5.7 mJy at 100 and 160  $\mu\text{m}$ , respectively; and GOODS-S,  $\sim 300 \text{ arcmin}^2$  to 1.2, 1.2 and 2.4 mJy at 70, 100 and 160  $\mu\text{m}$ , respectively. Our reference samples are the blind catalogues at 70 (in GOODS-S only), 100 and 160  $\mu\text{m}$  to the  $3\sigma$  level, which contain 373 (all in GOODS-S), 7176 (GOODS-S: 717, GOODS-N: 291, ECFDS: 813, COSMOS: 5355) and 7376 (GOODS-S: 867, GOODS-N: 316, ECFDS: 688, COSMOS: 5105) sources at 70, 100 and 160  $\mu\text{m}$ , respectively. We refer to Berta et al. (2010, 2011) for a detailed description of the data catalogues and source counts.

### 2.1 Multiwavelength identification

The PEP fields benefit from an extensive multiwavelength coverage. We have therefore associated our sources to the ancillary catalogues by means of a multiband likelihood ratio technique (Sutherland & Saunders 1992; Ciliegi et al. 2001), starting from the longest available wavelength (160  $\mu\text{m}$ , PACS) and progressively matching 100  $\mu\text{m}$  (PACS), 70  $\mu\text{m}$  (PACS, GOODS-S only) and 24  $\mu\text{m}$  (*Spitzer*/Multi-band Imaging Photometer – MIPS). In the GOODS-S field, we have associated with our PEP sources the 24- $\mu\text{m}$  catalogue by Magnelli et al. (2009) that we have matched with the optical+near-IR+IRAC Multiwavelength Southern Infrared Catalogue (MUSIC) catalogue of Grazian et al. (2006), revised by Santini et al. (2009), which includes spectroscopic and photometric redshifts. To maximize the fraction of identifications, we limited our study to the area covered by the MUSIC catalogue ( $\sim 196 \text{ arcmin}^2$ ), obtaining 233, 468 and 492 sources at 70, 100 and 160  $\mu\text{m}$ , respectively, with flux density greater than the flux limits reported above (all with either spectroscopic or photometric redshifts). In the GOODS-N field, as described in Berta et al. (2010, 2011) and Gruppioni et al. (2010), a PSF-matched multiwavelength catalogue<sup>1</sup> was created, including photometry from the far-UV (*GALEX*) to the mid-IR (*Spitzer*). As in GOODS-S, to maximize the identifications, we limited our study in GOODS-N to the area covered by the Advanced Camera for Surveys (ACS) on the Hubble Space Telescope ( $\sim 150 \text{ arcmin}^2$ ), obtaining 176 and 186 sources with flux density greater than the flux limit at 100 and 160  $\mu\text{m}$ , respectively (all with redshifts). We have matched our sources in the ECFDS with the Multiwavelength Survey by Yale-Chile by Cardamone et al. (2010), obtaining 687 sources at 100  $\mu\text{m}$  and 625 sources at 160  $\mu\text{m}$  (578 and 547 with redshifts,  $\sim 45$  per cent spectroscopic). Finally, in COSMOS, we have matched our catalogue with the deep 24- $\mu\text{m}$  sample of Le Floc’h et al. (2009) and with the IRAC-based catalogue of Ilbert et al. (2010), including optical and near-IR photometry and

<sup>1</sup> Publicly available at [http://www.mpe.mpg.de/ir/Research/PEP/public\\_data\\_releases.php](http://www.mpe.mpg.de/ir/Research/PEP/public_data_releases.php).



photometric redshifts. After the removal of PEP sources within flagged areas of the optical and/or IRAC COSMOS catalogues, we ended up with two catalogues consisting of 4110 and 4118 sources, with flux densities  $\geq 5.0$  and  $\geq 10.2$  mJy at 100 and 160  $\mu\text{m}$ , respectively (3817 and 3849 with either spectroscopic or photometric redshifts). Throughout this paper and specifically for the SED fits described in Section 2.2, we adopt these spectroscopic or rest-frame UV to near-IR photometric redshifts for the various fields.

The HerMES extragalactic survey (Oliver et al. 2012) performed coordinated observations with SPIRE at 250, 350 and 500  $\mu\text{m}$  in the same fields covered by PEP. In particular, in HerMES a prior source extraction was performed using the method presented in Roseboom et al. (2010), based on MIPS-24  $\mu\text{m}$  positions. The 24- $\mu\text{m}$  sources used as priors for SPIRE source extraction are the same as those associated with our PEP sources through the likelihood ratio technique. We have therefore associated the HerMES sources with the PEP sources by means of the 24- $\mu\text{m}$  sources matched to both samples. For most of our PEP sources ( $\sim 87$  per cent on average, though the SPIRE identification rates vary from  $\sim 84$  per cent in GOODS-S to 96 per cent in ECDFS), we found a  $>3\sigma$  SPIRE counterpart in the HerMES catalogues.

## 2.2 Galaxy classification

We made use of all the available multiwavelength data to derive the SEDs of our PEP sources, which we interpreted and classified by performing a  $\chi^2$  fit (using the LE PHARE code;<sup>2</sup> Arnouts et al. 2002 and Ilbert et al. 2006) with the semi-empirical template library of Polletta et al. (2007), representative of different classes of IR galaxies and AGN. To this library we added some templates modified in their far-IR part to better reproduce the observed *Herschel* data (see Gruppioni et al. 2010), and three starburst templates from Rieke et al. (2009). If required to improve the fit, different extinction values [ $E(B - V)$  from 0.0 to 0.5] have been applied to the templates, by letting the code free to choose the most suitable extinction curve. The considered set of templates included SEDs of elliptical galaxies of different ages, lenticular, spirals (from Sa to Sdm), starburst galaxies (SB), type 1 QSOs, type 2 QSOs, Seyferts, LINERs and composite Ultra Luminous Infrared Galaxies (ULIRGs, containing both starburst and obscured AGN component), in the wavelength range 0.1–1000  $\mu\text{m}$ . The latter templates are empirical ones created to reproduce the SEDs of the heavily obscured AGN. Two of these SEDs [the broad absorption-line QSO Markarian 231 (Berta 2005) and the Seyfert 2 galaxy IRAS 19254–7245 South (Berta et al. 2003)] are similar in shape, containing a powerful starburst component, mainly responsible for their far-IR emission, and an AGN component that contributes to – and dominates – the mid-IR (Farrah et al. 2003), reproducing the SEDs of ‘obscured’ AGN regardless of their optical spectra (i.e. broad or narrow lines in the optical; Gruppioni et al. 2008). Hereafter, we will refer to this class of templates and to the sources reproduced by them as to type 2 AGN (AGN2). Three other empirical templates, reproducing the observed SEDs of nearby ULIRGs containing an obscured AGN (i.e. IRAS 20551–4250; IRAS 22491–1808; NGC 6240) have been associated with the Seyfert 1.8/2, LINER ones, since they all contain an AGN, but this AGN does not dominate the observed energetic output at any wavelength (from UV to far-IR/sub-mm), showing up just in the range where the host galaxy SED has a minimum (i.e. the mid-IR). The AGN in these objects is either obscured or of low luminosity. We refer to this class as to star-forming galaxies

containing an AGN (SF-AGN), since their IR luminosity is largely dominated by SF.

In our analysis, we make the basic assumption that the SED shapes seen at low redshifts are also able to represent the higher redshift objects. In any case, to further increase the range of SEDs in the fit, we have applied additional extinction with different extinction curves to our templates. All SED fits adopt spectroscopic or photometric redshifts described in Section 2.1.

The template library used to fit our data contains a finite number of SEDs (38), representative of given classes of local infrared objects, which do not vary with continuity from one class to another (there are large gaps in the parameter space). Therefore, the quality of the fit depends not only on the photometric errors, but also on the template SED uncertainties. For this reason, in our fitting procedure, in addition to the photometric errors on data, we need to take into account also the uncertainties due to the template SEDs discretization and additional extinction. To do this, we have proceeded as described in detail by Gruppioni et al. (2008) and summarized as follows. First, we have run LE PHARE on our PEP SEDs considering the nominal errors from catalogues, computing the distributions of the  $(S_{\text{object}} - S_{\text{template}})_{\text{band}} / (\sigma_{\text{object}})_{\text{band}}$  values in each of the considered photometric band (where  $S_{\text{object}}$  and  $\sigma_{\text{object}}$  are the flux density and the relative error of the source, and  $S_{\text{template}}$  the flux density of the template in the considered band), iteratively increasing the photometric errors until we have obtained a Gaussian distribution with  $\sigma \sim 1$ . This corresponds to reduced  $\chi^2$  distributions peaked around 1 (as expected in the case of good fit). With the new photometric uncertainties (on average, significantly increased mainly in the optical/near-IR and SPIRE bands), we have run LE PHARE on our sources for the second time, obtaining what we have taken as the final SED-fitting results.

The majority of our PEP sources are reproduced by templates of normal spiral galaxies (spiral), SB galaxies (starburst) and Seyfert2/1.8/LINERs/ULIRGs+AGN (SF-AGN), although different classes prevail at different redshifts and luminosities. The spiral SEDs show no clear signs of enhanced SF or nuclear activity (see Fig. 1), the far-IR bump being characterized by relatively cold dust ( $T_{\text{dust}} \sim 20$  K). On the other hand, SB templates are characterized by warmer ( $T_{\text{dust}} \sim 40\text{--}45$  K), more pronounced far-IR bumps and significant UV extinction, indicative of intense SF activity. Templates of star-forming galaxies containing either a low-luminosity or obscured AGN (SF-AGN) are characterized by a ‘flattening’ in the 3–10  $\mu\text{m}$  spectrum (suggesting detection of an AGN in the wavelength range where the host galaxy SED has a minimum) and a far-IR bump dominated by SF, which is intermediate (in terms of both energy and  $T_{\text{dust}}$ ) between spirals and SBs. Although they can be considered as star-forming galaxies at the wavelengths relevant to this work, we prefer to refer to them as SF-AGN throughout the paper, to keep in mind that they probably contain an AGN, whose presence, though not dominant in the far-IR, might be very important for analysis in other bands (e.g., in the X-rays or the mid-IR).

We note that the well-studied high- $z$  ( $\simeq 2.3$ ) SED of the strongly lensed sub-mm galaxy SMM J2135–0102, known as ‘the Cosmic Eyelash’ (Ivison et al. 2010; Swinbank et al. 2010), best fitted with our procedure by an extinct [ $E(B - V) \sim 0.2$ ] IRAS 22491–1808 template (though rather poorly in the near-IR), does not represent the bulk of our population at high- $z$  ( $> 1.5$ ), whose SEDs are indeed well reproduced by our library of templates.

In fact, the considered template set provides very good fits to the SEDs of our PEP sources. In Fig. 1, we show the rest-frame SEDs (black dots) of the PEP sources belonging to the different ‘broad’ SED classes (spiral, starburst, SF-AGN, AGN1 and AGN2),

<sup>2</sup> Available at <http://www.cfht.hawaii.edu/~arnouts/LEPHARE/lephare.html>.

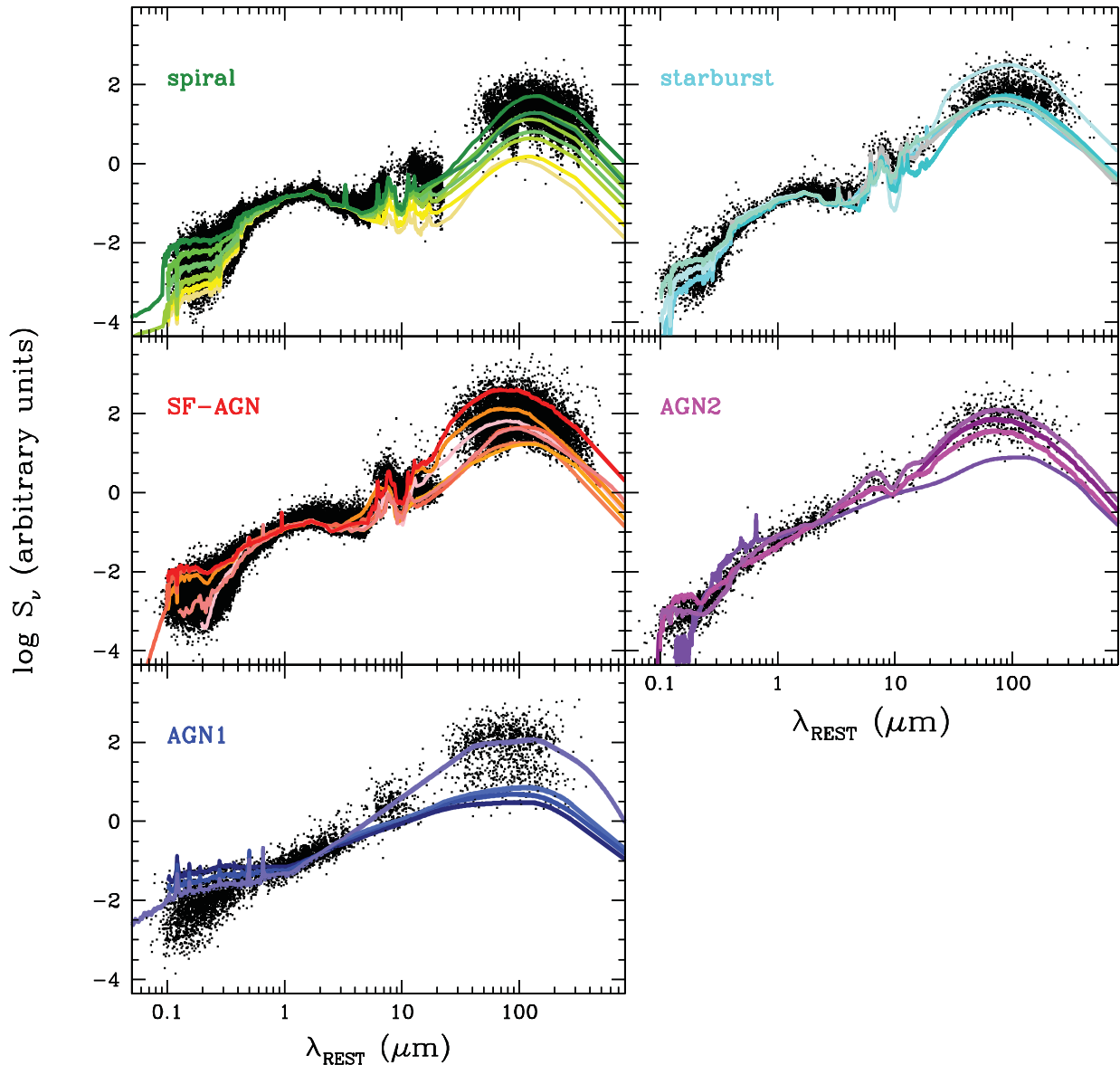


**Figure 1.** Observed rest-frame SEDs of the PEP sources (black dots) divided by population (as shown in the plot) and normalized to the  $K_s$  band. The more representative templates for each SED-class have been overplotted in different colours.

compared to the template SEDs of those classes normalized to the  $K_s$ -band flux density. In Table 1, we report the fraction of sources belonging to each SED class: we find that in all the fields  $\sim 41(38)$  per cent of the  $100(160)\text{-}\mu\text{m}$  sources are reproduced by a spiral template SED,  $7(7)$  per cent with a starburst template SED,  $45(48)$  per cent with an SF-AGN template SED,  $2(3)$  per cent with an AGN2 SED and  $5(4)$  per cent with an AGN1 SED. We note that the fraction of SF-AGN derived in this work is in agreement with results from mid-IR spectroscopy (with *Spitzer*-InfraRed Spectrograph) of local star-forming galaxies from the Spitzer Infrared Nearby Galaxies Survey (SINGS) sample by Smith et al. (2007), who found that  $\sim 50$  per cent of local galaxies (though of lower luminosities than ours) do harbour low-luminosity AGN (of LINER or Seyfert types). Recently, Sajina et al. (2012) found an even higher fraction ( $\sim 70$  per cent) of objects hosting an AGN in the mid-IR (*Spitzer*  $24\text{-}\mu\text{m}$ ) selected samples ( $\sim 23$  per cent AGN-dominated and  $\sim 47$  per cent showing both AGN and starburst activity). However, since the far-IR SED of the SF-AGN is dominated by SF and at these wavelengths

resembles either starburst or spiral galaxy templates, we have also divided the SF-AGN class into SF-AGN(SB) and SF-AGN(Spiral) sub-classes, based of their far-IR/near-IR colours (e.g.  $S_{100}/S_{1.6}$ ) and SED resemblance (apart from the rest-frame mid-IR flattening, which is detected in all of the SF-AGN SEDs). Specifically, galaxies best-fitted by the Seyfert 2/Seyfert 1.8 templates (either the original ones from Polletta et al. 2007 or those modified by Gruppioni et al. 2010) have been classified as SF-AGN(Spiral), while galaxies best-fitted by the NGC 6240, IRAS 205511-4250 or IRAS 22491-1808 templates have been classified as SF-AGN(SB). The number of sources belonging to the former and the latter sub-classes are also reported in Table 1 as additional information.

### 2.3 Redshift distribution

A large number of spectroscopic redshifts have been measured in the GOODS, ECDFS and COSMOS regions. In the GOODS-S and ECDFS area, a collection of more than 5000 spectroscopic redshifts

**Table 1.** SED classification.

Field	Spiral	Starburst	SF-AGN	AGN2	AGN1	SF-AGN(SB)	SF-AGN(Spiral)
GOODS-S	<i>N</i>	<i>N</i>	<i>N</i>	<i>N</i>	<i>N</i>	<i>N</i>	<i>N</i>
70 $\mu\text{m}$	53 (23 per cent)	22 (9 per cent)	142 (61 per cent)	5 (2 per cent)	12 (5 per cent)	26	116
100 $\mu\text{m}$	117 (25 per cent)	60 (13 per cent)	250 (53 per cent)	10 (2 per cent)	31 (7 per cent)	54	96
160 $\mu\text{m}$	123 (25 per cent)	55 (11 per cent)	277 (56 per cent)	11 (2 per cent)	26 (6 per cent)	73	204
GOODS-N	<i>N</i>	<i>N</i>	<i>N</i>	<i>N</i>	<i>N</i>	<i>N</i>	<i>N</i>
100 $\mu\text{m}$	68 (39 per cent)	20 (11 per cent)	78 (44 per cent)	7 (4 per cent)	3 (2 per cent)	21	57
160 $\mu\text{m}$	67 (36 per cent)	21 (11 per cent)	85 (46 per cent)	10 (5 per cent)	3 (2 per cent)	21	64
ECDFS	<i>N</i>	<i>N</i>	<i>N</i>	<i>N</i>	<i>N</i>	<i>N</i>	<i>N</i>
100 $\mu\text{m}$	253 (44 per cent)	49 (9 per cent)	245 (42 per cent)	8 (1 per cent)	23 (4 per cent)	83	162
160 $\mu\text{m}$	233 (43 per cent)	49 (9 per cent)	231 (42 per cent)	12 (2 per cent)	22 (4 per cent)	99	132
COSMOS	<i>N</i>	<i>N</i>	<i>N</i>	<i>N</i>	<i>N</i>	<i>N</i>	<i>N</i>
100 $\mu\text{m}$	1637 (43 per cent)	232 (6 per cent)	1689 (44 per cent)	76 (2 per cent)	183 (5 per cent)	580	1109
160 $\mu\text{m}$	1483 (39 per cent)	243 (6 per cent)	1847 (48 per cent)	103 (3 per cent)	173 (4 per cent)	777	1070
TOTAL	<i>N</i>	<i>N</i>	<i>N</i>	<i>N</i>	<i>N</i>	<i>N</i>	<i>N</i>
100 $\mu\text{m}$	2075 (41 per cent)	361 (7 per cent)	2262 (45 per cent)	101 (2 per cent)	240 (5 per cent)	738	1424
160 $\mu\text{m}$	1906 (38 per cent)	368 (7 per cent)	2440 (48 per cent)	136 (3 per cent)	224 (4 per cent)	970	1470

are available (Cristiani et al. 2000; Croom, Warren & Glazebrook 2001; Bunker et al. 2003; Dickinson et al. 2004; Stanway et al. 2004; Strolger et al. 2004; Szokoly et al. 2004; van der Wel et al. 2004; Doherty et al. 2005; Le Fèvre et al. 2005; Mignoli et al. 2005; Vanzella et al. 2008; Popesso et al. 2009; Santini et al. 2009; Balestra et al. 2010; Cooper et al. 2012). In the GOODS-N area, more than 2000 spectroscopic redshifts come from various observations (Cohen et al. 2000; Cowie et al. 2004; Wirth et al. 2004; Barger, Cowie & Wang 2008). Finally, in COSMOS we could use a collection of  $\sim 3000$  spectroscopic redshifts from either the public  $z$ COSMOS bright data base or the non-public  $z$ COSMOS deep data base (Lilly et al. 2007, 2009). For the PEP sources without spectroscopic redshift available, we have adopted the photometric redshifts derived from multi-wavelength (UV to near-IR) photometry by different authors in the different fields, as mentioned in Section 2.1. In the GOODS-S field, the MUSIC photometric redshift catalogue (Grazian et al. 2006; Santini et al. 2009) provided photo- $z$ s for most of our PEP sources without spectroscopic data, while in the GOODS-N field, photo- $z$ s were obtained by Berta et al. (2010) for almost all the PEP sources within the ACS area. The Cardamone et al. (2010) and Ilbert et al. (2009) catalogues provided photometric redshifts for a large fraction of the PEP sources in the ECDFS and COSMOS areas, respectively. When considering both the spectroscopic and photometric redshifts, in our PEP fields the redshift incompleteness is very low. In particular, in the GOODS-S field we have either a spec- $z$  or a photo- $z$  for  $\sim 100$  per cent of the PEP sample within the MUSIC areas ( $\sim 80$  per cent spectroscopic, though most of them lie at  $z < 2.5$ ; see Berta et al. 2011). In the

GOODS-N field, we have a redshift completeness of  $\sim 100$  per cent of sources (70 per cent spectroscopic) within the ACS area. In the ECDFS and COSMOS fields, we have a redshift completeness of 88 and 93 per cent, respectively (45 and 40 per cent spectroscopic).

The uncertainty in the photometric redshifts has been evaluated by means of a comparison with the available spec- $z$ s by the different authors providing photo- $z$  catalogues in the PEP fields. In particular, Berta et al. (2011) have compared the photometric and the available spectroscopic redshifts in GOODS-S, GOODS-N and COSMOS, finding a fraction of outliers, defined as objects having  $\Delta z / (1 + z_{\text{spec}}) > 0.2$ , of  $\sim 2$  per cent for sources with a PACS detection. Most of these outliers are sources with few photometric points available, or SEDs not well reproduced by the available templates. The median absolute deviation of the  $\Delta z / (1 + z_{\text{spec}})$  distribution in the three fields analysed by Berta et al. (2011) is 0.04 for the whole catalogue, and 0.038 for PACS-detected objects. In GOODS-S, Grazian et al. (2006) found excellent agreement between photometric and spectroscopic redshifts over the fully accessible redshift range  $0 < z < 6$  ( $\sigma[\Delta z / (1 + z)] \simeq 0.045$ ), with a very limited number of catastrophic errors. In COSMOS, Ilbert et al. (2010) estimated the photometric redshift uncertainties of their 3.6- $\mu\text{m}$  catalogue matched with the COSMOS photo- $z$  multiwavelength catalogue of Ilbert et al. (2009), finding  $\sigma[\Delta z / (1 + z)] = 0.008$  (and  $< 1$  per cent of catastrophic failures) at  $i_{\text{AB}}^+ < 22.5$ ,  $\sigma[\Delta z / (1 + z)] = 0.011$  at  $22.5 < i_{\text{AB}}^+ < 24$  and  $\sigma[\Delta z / (1 + z)] = 0.053$  at  $24 < i_{\text{AB}}^+ < 25$ . In the ECDFS, by comparing non-X-ray sources with high-quality spectroscopic redshifts, Cardamone et al. 2010 found  $\sigma[\Delta z / (1 + z)] = 0.008$  to  $z \sim 1.2 = 0.027$  at  $1.2 \leq$

$z \leq 3.7$  and  $= 0.016$  at  $z > 3.7$ . Note that we have checked all the  $z > 2.5$  photometric redshifts through LE PHARE, assigning the LE PHARE-derived value in case of significant disagreement with that from the catalogue (though most resulted in very good agreement). The fractions of spectroscopic redshifts in the  $2.5 < z < 3.0$  interval amount to just  $\sim 6$  and  $\sim 25$  per cent in COSMOS and GOODS, respectively, dropping to  $\sim 4$  and  $\sim 6$  per cent at  $3.0 < z < 4.2$ . We note that from our comparison between photo- and spec- $z$  (when available) we find a general good agreement in all fields.

Photometric redshift errors may, in principle, affect the shape of the LF at the bright end: by scattering objects to higher redshifts, they make the steep fall-off at high luminosities appear shallower (e.g. Drory et al. 2003). To study the impact of redshift uncertainties on the inferred infrared LF, we have performed Monte Carlo simulations, as discussed in detail in Section 3.3. It is indeed very difficult to estimate the effect of catastrophic failures at  $z > 2.5$ , where mainly photometric redshifts are available and no reliable spectroscopic data can be used to validate them. Moreover, for the limited high- $z$  samples with spectroscopic information, different results are found in the different fields: i.e. in GOODS-S, Berta et al. (2011) found that up to 25 per cent of PACS detected sources above  $z \sim 2$  might have a higher than real photometric redshift, while in COSMOS the catastrophic failures (20 per cent) found by Ilbert et al. (2009) for MIPS-selected sources at  $2 < z < 3$  were mostly for photo- $z$  smaller than spectroscopic ones. In addition to that, sometimes high- $z$  spectroscopic redshifts can be even more uncertain than photometric ones and great care must be taken when selecting spec- $z$ s for comparison (i.e. we need to choose those with high-quality flags). For all these reasons, we limited our analysis of photo- $z$  uncertainties to the Monte Carlo simulations described in Section 3.3, without trying to derive uncertainties also due to catastrophic failures. In Section 3.2 we also note that the different (far-IR) photo- $z$  approach of Lapi et al. (2011) produces consistent LF results in the common part of the parameter space.

The median redshift of the 70- $\mu\text{m}$  sample in GOODS-S is  $z_{\text{med}}(70) = 0.67$  (the mean is  $\langle z \rangle_{70} = 0.86$ ), while those of the 100- and 160- $\mu\text{m}$  samples are different in each of the fields, given the different flux density depths reached by PEP in each area. In Table 2, we report the median and the mean redshifts found for the different fields (and for the combined sample) at the different selection wavelengths. As expected, GOODS-S reaches the highest redshifts, while the surveys in the COSMOS and ECDFS fields are shallower and sample lower redshifts. On average, the 160- $\mu\text{m}$  selection favours higher redshifts than the 100- $\mu\text{m}$  one (see also Berta et al. 2011).

In Fig. 2, we show the redshift distribution of the PEP sources selected at 100 and 160  $\mu\text{m}$  in the four different fields. The black solid histogram is the total redshift distribution in the field (one for each row of the plot), while the filled histograms in different colours represent the redshift distributions of the different populations (green, spiral; cyan, starburst; red, SF-AGN; magenta, AGN2;

blue, AGN1). The line-filled dashed histograms shown in the spiral and starburst panels represent the redshift distributions of the SF-AGN(Spiral) and SF-AGN(SB) sub-classes, respectively. In addition to the principal redshift peak, in GOODS-S a secondary peak centred at  $z \sim 2$  is clearly visible at both 100 and 160  $\mu\text{m}$ . A similar result has been shown and discussed also by Berta et al. (2011), while an extensive analysis of PACS GOODS-S large-scale structure at  $z = 2-3$  and of a  $z \sim 2.2$  filamentary overdensity have been presented by Magliocchetti et al. (2011).

### 3 THE LUMINOSITY FUNCTION

The sizes and depths of the PEP samples are such as to allow a direct and accurate determination of the far-IR LF in several redshift bins, from  $z \simeq 0$  up to  $z \sim 4$ . PEP+HerMES is the unique *Herschel* survey to allow such analysis over such a wide redshift and luminosity range, sampling both the faint and bright ends of the far-IR and total IR LFs with sufficient statistics. Because of the redshift range covered by PEP, we would need to make significant extrapolations in wavelength when computing the rest-frame LFs at any chosen wavelengths. In order to apply the smallest extrapolations for the majority of our sources, we choose to derive the far-IR LFs at the rest-frame wavelengths corresponding to the median redshift of each sample. Given the median redshift of the 70- $\mu\text{m}$  sample in GOODS-S ( $\sim 0.67$ , see Table 2), we use that sample to derive the rest-frame LF at 35  $\mu\text{m}$ . With the 100- and 160- $\mu\text{m}$  PEP samples (whose median redshifts are  $\sim 0.64$  and  $0.73$ , respectively), we derived the rest-frame LFs at 60 and 90  $\mu\text{m}$ . Note that, given the excellent multiwavelength coverage available for most of our sources (thanks also to the HerMES data available in all the PEP fields and providing reliable counterparts for most of our PEP sources), their SEDs are very well determined from the UV to the sub-mm. The extrapolations are therefore well constrained by accurately defined SEDs, even at high redshifts (i.e. at  $z \sim 3.5$  the rest-frame 90- $\mu\text{m}$  luminosity corresponds to  $\lambda_{\text{observed}} \sim 400 \mu\text{m}$ , which is still in the range covered by HerMES).

#### 3.1 Method

The LFs are derived using the  $1/V_{\text{max}}$  method (Schmidt 1968). This method is non-parametric and does not require any assumptions on the LF shape, but derives the LF directly from the data. We have first derived the LFs in each field separately, in order to check for consistency and to test the role of cosmic variance. Successively, we have made use of the whole data sets to derive the monochromatic and total IR LFs, by means of the Avni & Bahcall (1980) method for coherent analysis of independent data sets. We have divided the samples into different redshift bins, over the range  $0 \lesssim z \lesssim 4$ , selected to be almost equally populated, at least up to  $z \sim 2.5$ . In each redshift bin, we have computed the comoving volume available to each source belonging to that bin, defined as  $V_{\text{max}} = V_{z_{\text{max}}} - V_{z_{\text{min}}}$ , where  $z_{\text{max}}$  is the minimum between the maximum redshift at which a source would still be included in the sample given the limiting flux of the survey (different for each field) and the upper boundary of the considered redshift bin, while  $z_{\text{min}}$  is just the lower boundary of the considered redshift bin.

When combining the four samples, we have constructed a complete sample over the whole GOODS-S+GOODS-N+ECDFS(-GOODS-S)+COSMOS region, including all the observed objects (see details in Section 3.2). The depth of the sample is not constant throughout the region, but an object with a given flux density (included in the list of observed objects irrespective of the

**Table 2.** Average redshifts in the PEP Survey fields.

Field	70 $\mu\text{m}$		100 $\mu\text{m}$		160 $\mu\text{m}$	
	$z_{\text{med}}$	$\langle z \rangle$	$z_{\text{med}}$	$\langle z \rangle$	$z_{\text{med}}$	$\langle z \rangle$
GOODS-S	0.67	0.86	0.85	1.07	0.98	1.16
GOODS-N			0.73	0.84	0.84	0.94
ECDFS			0.66	0.76	0.69	0.85
COSMOS			0.59	0.74	0.70	0.88
ALL FIELDS	0.67	0.86	0.64	0.78	0.73	0.91



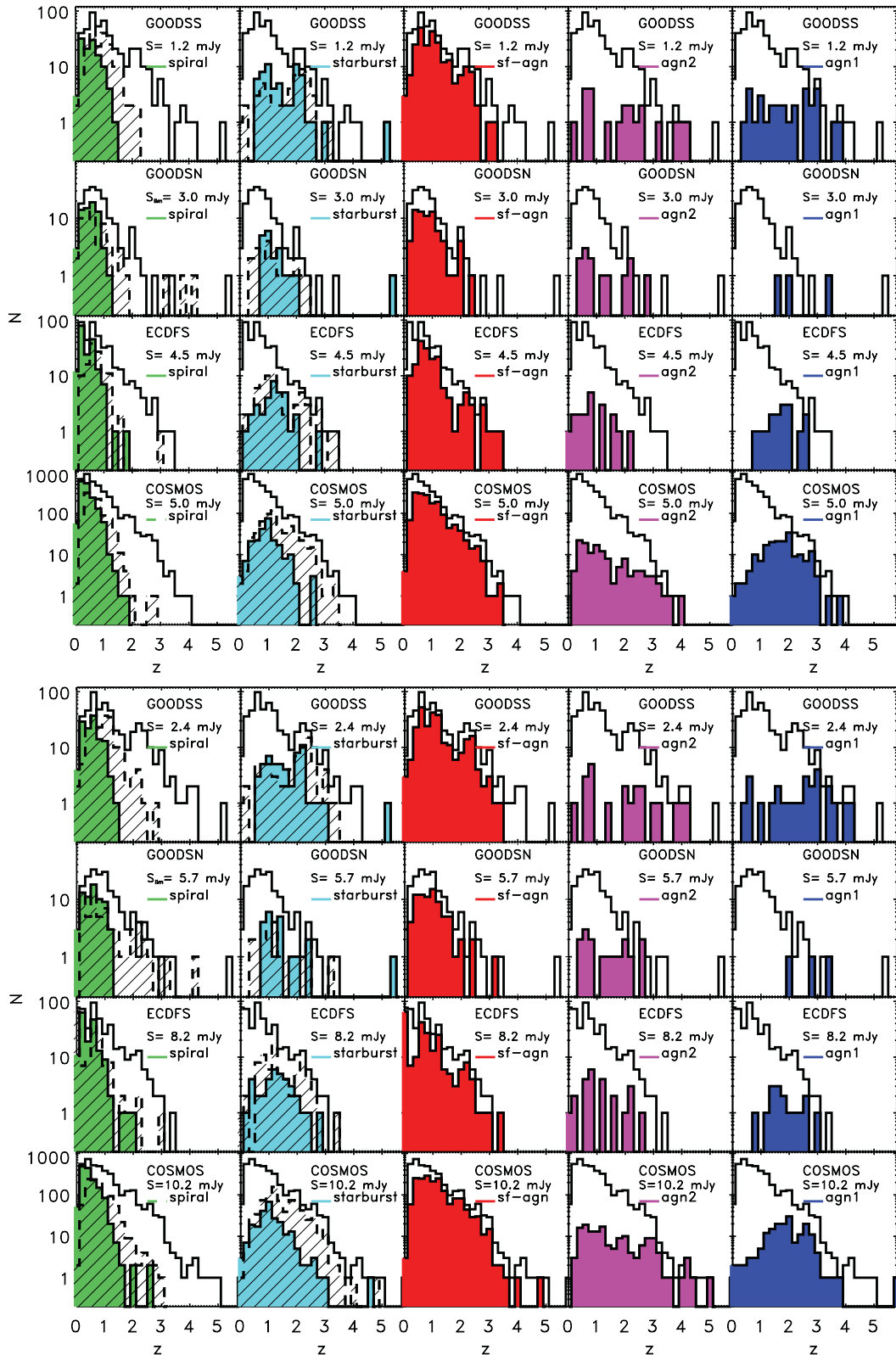


**Figure 2.** Redshift distributions of 100- $\mu\text{m}$  (top) and 160- $\mu\text{m}$  (bottom) sources in the four PEP fields (first row from top, GOODS-S; second row, GOODS-N; third row, ECDFS; bottom row, COSMOS) to different limiting fluxes (as shown in the plot). The redshift distributions of the five different populations have been plotted in different colours (green, spiral; cyan, starburst; red, SF-AGN; magenta, AGN2; blue, AGN1) and compared to the total distribution (black solid histogram). The line-filled dashed histograms shown in the spiral and starburst panels represent the redshift distributions of the SF-AGN(Spiral) and SF-AGN(SB) sub-classes, respectively.

identity of its parent sample) can a priori be found in one (or more) region if its redshift is  $\leq z_{\max}^{\text{fld}}(S_{\text{limit}})$  of that region (e.g. sources detected in the COSMOS area are detectable over the whole joint area, while the fainter sources detected in GOODS-S are detectable in GOODS-S only). The maximum volume of space which is available to such an object to be included in the joint sample is then defined by

$$\begin{aligned}
 V_{z_{\max,i}} &= \frac{\Omega_{\text{GS}}}{4\pi} V_{z_{\max}}^{\text{GS}} + \frac{\Omega_{\text{GN}}}{4\pi} V_{z_{\max}}^{\text{GN}} + \frac{\Omega_{\text{E}}}{4\pi} V_{z_{\max}}^{\text{E}} + \frac{\Omega_{\text{C}}}{4\pi} V_{z_{\max}}^{\text{C}} \\
 &\quad (\text{if } z_{\max,i} \leq z_{\max}^{\text{C}}) \\
 &= \frac{\Omega_{\text{GS}}}{4\pi} V_{z_{\max}}^{\text{GS}} + \frac{\Omega_{\text{GN}}}{4\pi} V_{z_{\max}}^{\text{GN}} + \frac{\Omega_{\text{E}}}{4\pi} V_{z_{\max}}^{\text{E}} \\
 &\quad (\text{if } z_{\max}^{\text{C}} < z_{\max,i} \leq z_{\max}^{\text{E}}) \\
 &= \frac{\Omega_{\text{GS}}}{4\pi} V_{z_{\max}}^{\text{GS}} + \frac{\Omega_{\text{GN}}}{4\pi} V_{z_{\max}}^{\text{GN}} \\
 &\quad (\text{if } z_{\max}^{\text{E}} < z_{\max,i} \leq z_{\max}^{\text{GN}}) \\
 &= \frac{\Omega_{\text{GS}}}{4\pi} V_{z_{\max}}^{\text{GS}} \\
 &\quad (\text{if } z_{\max}^{\text{GN}} < z_{\max,i}), \tag{1}
 \end{aligned}$$

where  $V_{z_{\max}}^{\text{fld}}$  (with fld = GS, GN, E, C corresponding to GOODS-S, GOODS-N, ECDFS and COSMOS, respectively) is the comoving volume available to each source in that field, in a given redshift bin, while  $\Omega_{\text{fld}}$  is the solid angle subtended by that field sample on the sky.

For each luminosity and redshift bin, the LF is given by

$$\Phi(L, z) = \frac{1}{\Delta L} \sum_i \frac{1}{w_i \times V_{\max,i}}, \tag{2}$$

where  $V_{\max,i}$  is the comoving volume over which the  $i$ th galaxy could be observed,  $\Delta L$  is the size of the luminosity bin and  $w_i$  is the completeness correction factor of the  $i$ th galaxy. These completeness correction factors are a combination of the completeness corrections given by Berta et al. (2010, 2011), derived as described in Lutz et al. (2011), to be applied to each source as a function of its flux density, together with a correction for redshift incompleteness (for the ECDFS and COSMOS only, see Section 2.3). Since, as mentioned in Section 2.3, the redshift incompleteness in the COSMOS and ECDFS areas is independent on PACS flux density, in these fields we have applied the corrections regardless of the source luminosity and redshift (i.e. by multiplying  $\Phi(L, z)$  by 1.07 and 1.14 in COSMOS and ECDFS, respectively). However, the redshift incompleteness does not affect our conclusions, since  $\gtrsim 95$  per cent of all our sources do have a redshift.

Uncertainties in the infrared LF values depend on photometric redshift uncertainties. To quantify the effects of the uncertainties in photometric redshifts on our luminosity functions, we performed a set of Monte Carlo simulations, as described in Section 3.3.

### 3.2 The rest-frame 35-, 60- and 90- $\mu\text{m}$ LF

By following the method described above, we have derived the 35-, 60- and 90- $\mu\text{m}$  rest-frame LFs from the 70- (in GOODS-S only), 100- and 160- $\mu\text{m}$  samples, respectively. In order to check the consistency between the catalogues and the effects of cosmic variance, we have first derived the monochromatic LFs in each field separately. Note that, since the 70- $\mu\text{m}$  data are available in the GOODS-S field only, to have a better sampling of the LF especially

at the bright-end, we have also computed the rest-frame 35- $\mu\text{m}$  LF from the 100- $\mu\text{m}$  samples in the four fields and compared them with that obtained from the 70- $\mu\text{m}$  sample (see Fig 3; Table 3). The agreement between the two derivations is very good, implying correct extrapolations in wavelength due to the good and complete SED coverage.

We have divided the samples into seven redshift bins:  $0.0 < z \leq 0.4$ ;  $0.4 < z \leq 0.8$ ;  $0.8 < z \leq 1.2$ ;  $1.2 < z \leq 1.8$ ;  $1.8 < z \leq 2.5$ ;  $2.5 < z \leq 3.5$  and  $3.5 < z \leq 4.5$ . The results of the computation of our 35- (reported in Table 3), 60- and 90- $\mu\text{m}$  LFs are shown in Figs 3, 4 and 5, respectively. The LFs in the four different fields appear to be consistent with each other within the error bars ( $\pm 1\sigma$ ) in most of the common luminosity bins. The COSMOS and GOODS-S Surveys are complementary, with the faint end of the LFs being mostly determined by data in GOODS-S, and the bright end by COSMOS data. After having checked the field-to-field consistency, we have combined the 100- and 160- $\mu\text{m}$  samples in all fields, obtaining the global rest-frame 60- and 90- $\mu\text{m}$  LFs (reported in Tables 4 and 5, respectively).

The data from each field in each  $z$ -bin have been plotted (and considered in the combination) only in the luminosity bins where we expect our sample to be complete, given that at fainter luminosities not all galaxy types are observable (depending on their SEDs; Ilbert et al. 2004). For comparison, we overplot the LFs at 35  $\mu\text{m}$  from Magnelli et al. (2009, 2011), the local LFs at 60  $\mu\text{m}$  from Saunders et al. (1990) and those at 90  $\mu\text{m}$  from Serjeant et al. (2004) and Sedgwick et al. (2011) and at 100  $\mu\text{m}$  from Lapi et al. (2011), respectively. The comparison between the 35- $\mu\text{m}$  LF, derived from the 70- $\mu\text{m}$  PEP sample in GOODS-S, and the results of Magnelli et al. (2009, 2011), based on a 24- $\mu\text{m}$  prior extraction and stacking analysis on *Spitzer* maps, shows very good agreement, both with the data and with the double power-law fit. The  $1.8 < z < 2.5$  PEP LF is consistent within  $\pm 1\sigma$  with the Magnelli et al. (2011) data points, though the power-law fit at bright  $L_{35} (> 10^{12} L_{\odot})$  seems to be slightly lower than our data. At  $z > 2.5$  no comparison data from *Spitzer* are available, while our LF derivation can provide hints of evolution at the bright end of the LF. In the common redshift intervals (between  $z \sim 1$  and 3.5), our 90- $\mu\text{m}$  LF is in very good agreement with the 100- $\mu\text{m}$  Lapi et al. (2011) derivation from the H-ATLAS survey (although their redshift bins are somewhat different than ours:  $1.2 < z < 1.6$ ;  $1.6 < z < 2.0$ ;  $2.0 < z < 2.4$  and  $2.4 < z < 4.0$ ) and with the previous PEP-SDP derivation (Gruppioni et al. 2010). The consistency between our 90- $\mu\text{m}$  LFs and the Lapi et al. (2011) ones (derived from a different sample, using a different template SED to fit the data and a rest-frame far-IR based method to derive photometric redshifts) gives us confidence that, at least up to  $z \sim 3.5$ , our computation is not significantly affected by incompleteness or by photo- $z$  uncertainties.

### 3.3 The total infrared LF

We integrate the best-fitting SED of each source over  $8 \leq \lambda_{\text{rest}} \leq 1000 \mu\text{m}$  to derive the total IR luminosities ( $L_{\text{IR}} = L[8-1000 \mu\text{m}]$ ) in 11 redshift bins (0.0–0.3; 0.3–0.45; 0.45–0.6; 0.6–0.8; 0.8–1.0; 1.0–1.2; 1.2–1.7; 1.7–2.0; 2.0–2.5; 2.5–3.0 and 3.0–4.2), selected to be almost equally populated, at least up to  $z \sim 2.5$ . Our approach is similar to that of other studies based on mid-IR-selected galaxy samples (e.g. Le Floc'h et al. 2005; Rodighiero et al. 2010a; Magnelli et al. 2011), but this is the first time that the SEDs have been accurately constrained by sufficiently deep data in the far-IR/sub-mm domain and not simply extrapolated from the mid-IR to the longer wavelengths or from average flux density ratios.

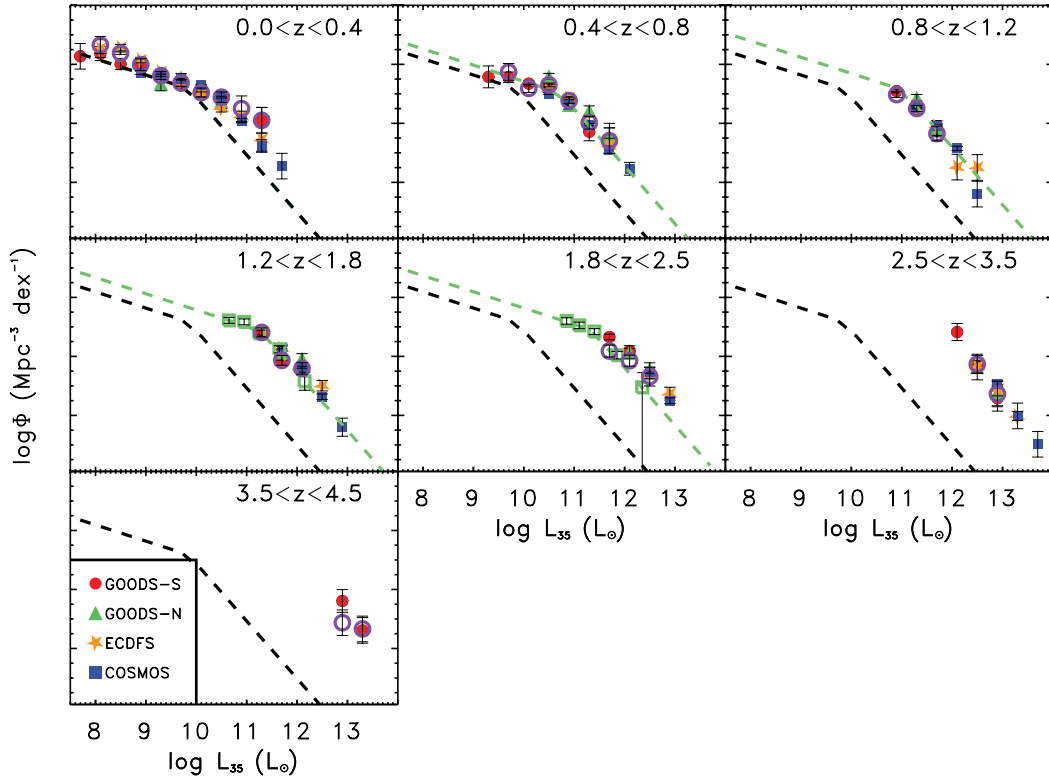


**Figure 3.** Rest-frame 35- $\mu\text{m}$  LF estimated with the  $1/V_{\text{max}}$  method from the PEP 70- $\mu\text{m}$  sample in the GOODS-S field (purple open circles) and independently in the four PEP fields from the 100- $\mu\text{m}$ -selected samples (red filled circles, GOODS-S; green filled triangles, GOODS-N; orange filled stars, ECDFS; blue filled squares, COSMOS). The error bars in the data points represent the Poissonian uncertainties. For comparison, we also plot the determination of Magnelli et al. (2011) at  $1.2 < z < 2.5$ , shown as green open squares, and the double power-law fit of Magnelli et al. (2009, 2011), shown as a green dashed line. The black dashed line represents the  $z = 0$  determination of Magnelli et al. (2009).

As mentioned in Section 2.3, we have studied the impact of redshift uncertainties on the total IR LF by performing Monte Carlo simulations. As test cases, we used the COSMOS and GOODS-S samples (which are basically defining the bright and faint ends of the LF in an almost complementary way), and we checked the effect on the total IR LF. We iterated the computation of the total IR LF by each time varying the photometric redshift of each source (assigning a randomly selected value, according to a Gaussian distribution, within the 68 per cent confidence interval). Each time, we then recomputed the monochromatic and total IR luminosities, as well as the  $V_{\text{max}}$  value, but we did not perform the SED fitting again, keeping the previously found best-fitting template for each object (the effect on the  $k$ -correction is not relevant in the far-IR wavelength range). The results of this Monte Carlo simulation are reported in Fig. 6, where we show the total IR LFs derived in each of the PEP fields independently: the red and blue filled circles represent the estimates of the GOODS-S and COSMOS LFs, with their range of values derived with 20 iterations by allowing a change in photo- $z$  represented by the pink and sky-blue shaded areas, respectively. The comparison shows that the effect of the uncertainty of the photometric redshifts on the error bars is slightly larger than the simple Poissonian value ( $1/\sqrt{N}$ ), and affects mainly the lower and the higher redshift bins (especially at low and high luminosities). Using these Monte Carlo simulations, we find no evident systematic offsets caused by the photometric redshift uncertainties (see Fig. 6). This is due to the very accurate photometric redshifts available in these fields. For the total uncertainty in each luminosity bin in GOODS-S and COSMOS, we have therefore assumed the dispersion given by the Monte Carlo simulations (as shown in

Fig. 7). We note that at the higher  $z$  ( $> 2.5$ ), where we must rely on a majority of photometric redshifts, the true uncertainties (taking into account also catastrophic failures or incompleteness effects) might be larger than derived with simulations. The unavailability of a ‘true’ comparison sample (i.e. a large comparison sample with accurate spectroscopic redshifts and fully representative for the PACS flux selection) at high  $z$  does not allow us to properly quantify this statement.

In Fig. 7, the total IR LFs obtained by combining the 160- $\mu\text{m}$ -selected samples with the Avni & Bahcall (1980) technique is plotted and compared with other derivations available in the literature. The total IR LF of Sanders et al. (2003) is plotted as a local reference, in addition to the LFs of Le Floch et al. (2005), Rodighiero et al. (2010a), Caputi et al. (2007) and Magnelli et al. (2009, 2011) in various redshift intervals. Globally, data from surveys at different wavelengths agree relatively well over the common  $z$ -range. No data for comparison are available at  $z > 2.5$ , apart from the IR LF of sub-mm galaxies from Chapman et al. (2005) and Wall, Pope & Scott (2008) at  $z \sim 2.5$ , which represent reasonably well just the very bright end of the total IR LF. Our derivation is the first at such high redshifts, especially in the  $3 < z \leq 4.2$  range. Note the good agreement between our PEP-based total IR LF and the HerMES-based one derived by Vaccari et al. (in preparation), shown by the red open squares in Fig. 7. Though consistent within the error bars, in the highest redshift bin the HerMES LF is slightly higher than ours. Since the 250- $\mu\text{m}$  HerMES selection favours the detection of higher redshift sources than the PEP one, it is more likely that the PEP LF in the higher- $z$  bin is affected by some flux/redshift incompleteness rather than by the presence of low- $z$

**Table 3.** Rest-frame 35- $\mu\text{m}$  LF.

$\log(L_{35}/L_{\odot})$	$\log(\Phi/\text{Mpc}^{-3} \text{ dex}^{-1})$						
	$0.0 \leq z < 0.4$	$0.4 \leq z < 0.8$	$0.8 \leq z < 1.2$	$1.2 \leq z < 1.8$	$1.8 \leq z < 2.5$	$2.5 \leq z < 3.5$	$3.5 \leq z < 4.5$
From the GOODS-S 70- $\mu\text{m}$ sample							
7.9–8.3	$-1.34 \pm 0.29$						
8.3–8.7	$-1.62 \pm 0.04$						
8.7–9.1	$-2.01 \pm 0.20$						
9.1–9.5	$-2.38 \pm 0.14$						
9.5–9.9	$-2.63 \pm 0.12$	$-2.26 \pm 0.29$					
9.9–10.3	$-2.96 \pm 0.15$	$-2.81 \pm 0.14$					
10.3–10.7	$-3.11 \pm 0.18$	$-2.70 \pm 0.06$					
10.7–11.1	$-3.50 \pm 0.43$	$-3.23 \pm 0.09$	$-3.03 \pm 0.09$				
11.1–11.5	$-3.90 \pm 0.43$	$-3.98 \pm 0.22$	$-3.50 \pm 0.10$	$-3.19 \pm 0.15$			
11.5–11.9		$-4.59 \pm 0.43$	$-4.35 \pm 0.25$	$-4.14 \pm 0.17$	$-3.82 \pm 0.20$		
11.9–12.3				$-4.41 \pm 0.19$	$-4.14 \pm 0.19$		
12.3–12.7					$-4.68 \pm 0.32$	$-4.27 \pm 0.30$	
12.7–13.1						$-5.27 \pm 0.43$	$-5.13 \pm 0.43$
13.1–13.5							$-5.34 \pm 0.43$
From the combined 100- $\mu\text{m}$ sample							
7.5–7.9	$-1.74 \pm 0.43$						
7.9–8.3	$-1.64 \pm 0.23$						
8.3–8.7	$-2.00 \pm 0.19$						
8.7–9.1	$-2.01 \pm 0.09$						
9.1–9.5	$-2.37 \pm 0.03$	$-2.43 \pm 0.37$					
9.5–9.9	$-2.53 \pm 0.02$	$-2.48 \pm 0.19$					
9.9–10.3	$-2.73 \pm 0.02$	$-2.66 \pm 0.08$					
10.3–10.7	$-3.14 \pm 0.03$	$-2.56 \pm 0.03$	$-2.79 \pm 0.10$				
10.7–11.1	$-3.91 \pm 0.07$	$-3.34 \pm 0.02$	$-2.91 \pm 0.06$				
11.1–11.5	$-4.73 \pm 0.18$	$-4.03 \pm 0.04$	$-3.46 \pm 0.03$	$-3.13 \pm 0.07$	$-3.24 \pm 0.32$		
11.5–11.9	$-5.51 \pm 0.43$	$-4.90 \pm 0.10$	$-4.09 \pm 0.03$	$-3.77 \pm 0.04$	$-3.38 \pm 0.10$		
11.9–12.3		$-5.60 \pm 0.22$	$-4.90 \pm 0.07$	$-4.37 \pm 0.03$	$-3.98 \pm 0.07$	$-3.18 \pm 0.29$	
12.3–12.7			$-6.16 \pm 0.31$	$-5.34 \pm 0.09$	$-4.54 \pm 0.04$	$-4.30 \pm 0.12$	
12.7–13.1				$-6.46 \pm 0.31$	$-5.48 \pm 0.09$	$-4.99 \pm 0.07$	$-4.40 \pm 0.39$
13.1–13.5						$-6.03 \pm 0.15$	$-5.91 \pm 0.26$
13.5–13.9						$-7.04 \pm 0.43$	

sources erroneously placed at high- $z$  by incorrect photometric redshift assignment (catastrophic failures). The values of our total IR LF for each redshift and luminosity bin are reported in Table 6.

### 3.4 Evolution

In order to study the evolution of the total IR LF, we derive a parametric estimate of the LF at different redshifts. For the shape of the LF, we assume a modified-Schechter function (i.e. Saunders et al. 1990), where  $\Phi(L)$  is given by

$$\Phi(L)d\log L = \Phi^* \left(\frac{L}{L^*}\right)^{1-\alpha} \exp\left[-\frac{1}{2\sigma^2} \log_{10}^2\left(1 + \frac{L}{L^*}\right)\right] d\log L, \quad (3)$$

behaving as a power law for  $L < L^*$  and as a Gaussian in  $\log L$  for  $L > L^*$ . The adopted LF parametric shape depends on four parameters ( $\alpha$ ,  $\sigma$ ,  $L^*$  and  $\Phi^*$ ), whose best-fitting values and uncertainties have been found using a non-linear least-squares fitting procedure. In detail, while in the first  $z$ -bin all the parameters have been estimated, starting from the second  $z$ -bin, the values of  $\alpha$  and  $\sigma$  have been frozen at the values found at lower redshift, leaving only  $L^*$  and  $\Phi^*$  free to vary (see Table 7). Note that, in the highest redshift bin ( $3.0 < z < 4.2$ ) we are not able to constrain the LF break, while we are up to  $\sim 3$ . Therefore, the results found at this redshift are affected by larger uncertainties than the  $z \lesssim 3$  ones. However, although there is some degeneracy in the values of  $L^*$  and  $\Phi^*$  at

$3.0 < z < 4.2$ , the range of allowed value combinations still giving a reasonable fit to the three observed data points (constraining the bright-end of the LF) is limited and do not significantly affect our results.

In Fig. 8, we plot the total IR LFs at all redshifts with the  $\pm 1\sigma$  Poissonian uncertainty regions (different colours for different  $z$ -intervals). There is a clear luminosity evolution with redshift, at least up to  $z \sim 3$ . The apparent ‘fall’ of the  $z > 3$  LF with respect to those at lower redshifts, if real, might imply a global negative evolution of the IR galaxies and/or AGN starting at  $z \gtrsim 3$ . However, as mentioned above, we must point out that in the highest redshift bin PACS data could be affected by incompleteness, since with increasing redshift (and for intrinsically ‘cold’ sources) the true PACS fluxes might fall below the detection limit (i.e. faint sources should be missed even if completeness corrections are perfect), while, if luminous enough, they can still be detectable by SPIRE. This effect is expected to be more relevant in COSMOS, where SPIRE data are quite deep relatively to PACS, while it should not happen in GOODS-S, where PACS data are very deep compared to the SPIRE ones (which are limited by confusion). The high- $z$  incompleteness of PACS surveys might also be emphasized by the redshift incompleteness of the COSMOS sample, which could affect the highest redshift bins more than the lower ones (although the redshift incompleteness seems to be independent of redshift; see Berta et al. 2011). However, we must point out that a decrease at  $z \gtrsim 2.7$ – $3$ , similar to that observed in our data, is also observed in the



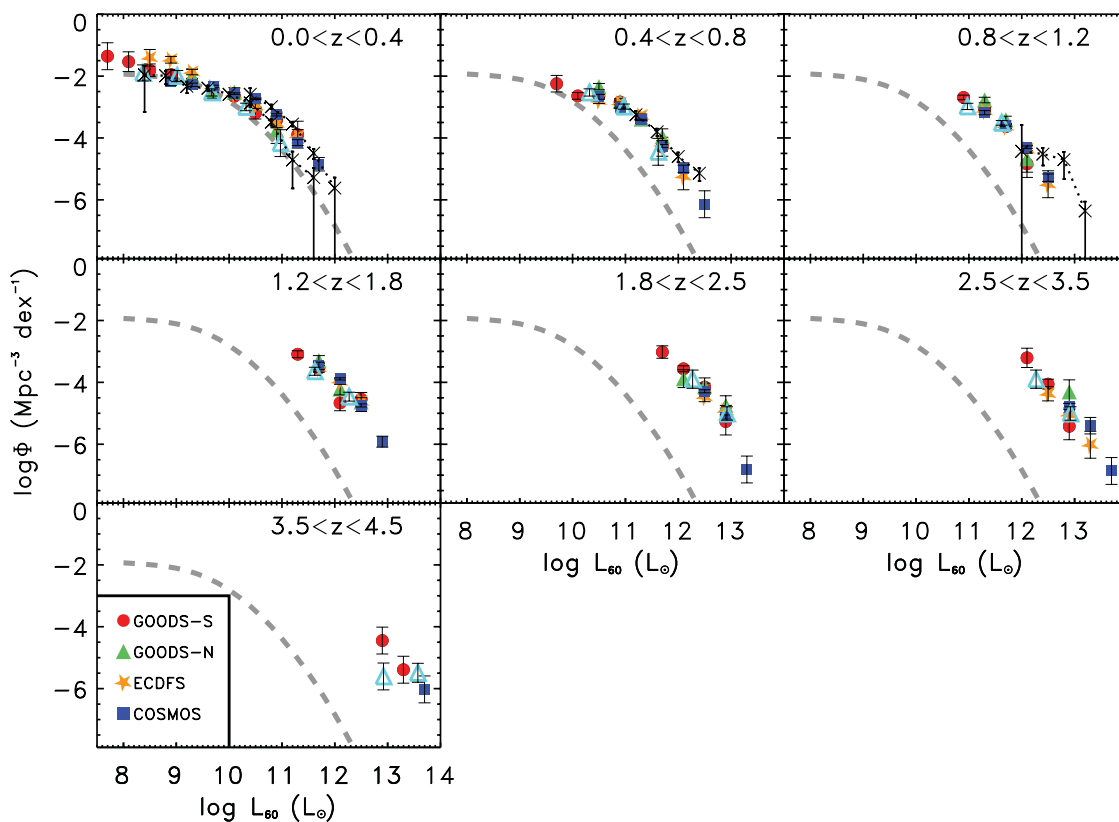


**Figure 4.** Rest-frame 60- $\mu\text{m}$  LF estimated independently from the 100- $\mu\text{m}$ -selected samples in the four PEP fields (red filled circles, GOODS-S; green filled triangles, GOODS-N; orange filled stars, ECFDS; blue filled squares, COSMOS). The diagonal crosses connected by the dotted line are the *Spitzer* 70- $\mu\text{m}$  derivations of Patel et al. (2013) (in the lower  $z$ -bin we report their LFs derived both at  $0.0 < z < 0.2$  and at  $0.2 < z < 0.4$ ). The cyan open triangles show the PEP 60- $\mu\text{m}$  LF from the SDP data in GOODS-N by Gruppioni et al. (2010) (the redshift bins are not exactly the same). The grey dashed line shows the Saunders et al. (1990) local LF.

space density of X-ray (see Brusa et al. 2009; Civano et al. 2011) and optically selected AGN (Richards et al. 2006), and of sub-mm galaxies (Wall, Pope & Scott 2008), as well as in the HerMES total IR LF – though less evident (from 250- $\mu\text{m}$  data; Vaccari et al., in preparation; see Fig. 7). Moreover, our result is in agreement with the recent finding of Smit et al. (2012) that the characteristic value of the galaxy SFR exhibits a substantial, linear decrease as a function of redshift from  $z \sim 2$  to  $z \sim 8$ .

In Fig. 9, we show the values of  $L^*$  and  $\Phi^*$  at different redshifts, with the best curve  $[\propto (1+z)^k]$  fit to the data points. The values of the curve slopes and of the redshifts corresponding to evolutionary breaks have been chosen to be those which minimize the  $\chi^2$  of the fit with two power laws. We find a significant variation of  $L^*$  with  $z$ , which increases as  $(1+z)^{3.55 \pm 0.10}$  up to  $z \sim 1.85$ , and as  $(1+z)^{1.62 \pm 0.51}$  between  $z \sim 1.85$  and  $z \sim 4$ . The variation of  $\Phi^*$  with redshift starts with a slow decrease as  $(1+z)^{-0.57 \pm 0.22}$  up to  $z \sim 1.1$ , followed by a rapid decrease  $\propto (1+z)^{-3.92 \pm 0.34}$  at  $z \gtrsim 1.1$  and up to  $z \sim 4$ .

Previous estimations of the evolution of  $L^*$  and  $\Phi^*$  in the past (i.e. Caputi et al. 2007, Bethermin et al. 2011 and Marsden et al. 2011) discussed a decrease in the density of far-IR sources between  $z = 1$  and  $z = 2$ . In particular, Bethermin et al. (2011) and Marsden et al. (2011), by evolving a parametrized far-IR LF, explored the evolution required by the source counts in the parameter space. The results of these works (especially those of Bethermin et al. 2011, showing a decrease of  $\Phi^*$  at  $z > 1$  and a flatter trend on the evolution of  $L^*$  at  $z > 2$ ) are close to ours, though with the source counts only it was not possible to constrain the evolution of IR sources at  $z > 2$ .

### 3.5 Evolution of the different IR populations

The PEP survey, given its size and its coverage in luminosity and redshift, allows us to go further in investigating the evolution of the total IR LF: it gives us the opportunity to study the evolution of the different galaxy classes that compose the global IR population. To investigate the different evolutionary paths of the various IR populations, we have computed the  $1/V_{\text{max}}$  LFs separately for the five galaxy classes defined by the SED-fitting analysis. In Fig. 10, we show the total IR LFs derived from the combined PEP samples for the different SED classes (coloured filled areas). The results of the fit to a modified Schechter function (see equation 3) for each population are overplotted on the data. In fact, by following the same procedure adopted for the global LF, a parametric fit to the LFs at different redshifts has been performed also for the single populations. The  $\alpha$  and  $\sigma$  parameters, for each population, have been estimated at the redshift where the corresponding LF is best sampled (not necessarily at the lowest  $z$ -bin as for the global LF). Subsequently, the values of  $\alpha$  and  $\sigma$  have been frozen at the values found in the ‘optimal’ redshift bin, leaving only  $L^*$  and  $\Phi^*$  free to vary. In Fig. 11, analogously to Fig. 9, we show the values of  $L^*$  and  $\Phi^*$  at different redshifts for the different populations, with the best least-squares fitting curves  $[\propto (1+z)^k]$  overplotted. The best-fitting values of  $\alpha$ ,  $\sigma$ ,  $L^*$  and  $\Phi^*$  in the first redshift bin, together with the parameters describing the luminosity  $[k_{L,1}, k_{L,2}$  and  $z_{b,L}: \propto (1+z)^{k_{L,1}}$  to  $z = z_{b,L}$ ,  $\propto (1+z)^{k_{L,2}}$  at  $z > z_{b,L}$ ] and density evolution  $[k_{\rho,1}, k_{\rho,2}$  and  $z_{b,\rho}: \propto (1+z)^{k_{\rho,1}}$  out to  $z = z_{b,\rho}$ ,  $\propto (1+z)^{k_{\rho,2}}$  at  $z > z_{b,\rho}$ ] are reported in Table 8.

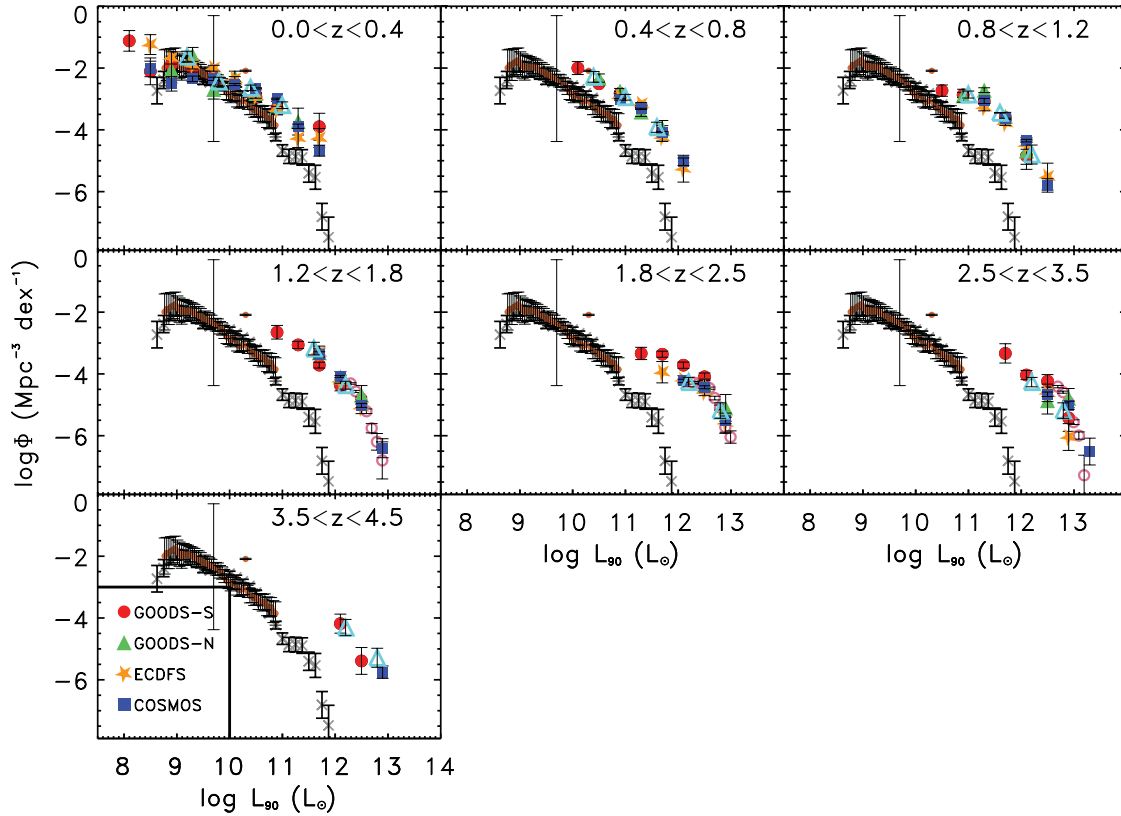


**Figure 5.** Rest-frame 90- $\mu\text{m}$  LF estimated independently from the 160- $\mu\text{m}$ -selected samples in the four PEP fields with the  $1/V_{\text{max}}$  method (with the same symbols as in Fig. 4). The diagonal crosses represent the local LF of Serjeant et al. (2004), the brown dots with error bars are the local LF of Sedgwick et al. (2011) in the *AKARI* Deep Field, while the pink open circles are the 100- $\mu\text{m}$  LF derivation of Lapi et al. (2011) in the H-ATLAS fields. The cyan open triangles show the PEP 90- $\mu\text{m}$  LF computed by Gruppioni et al. (2010) from the SDP data in the GOODS-N (not exactly the same redshift bins).

**Table 4.** Combined rest-frame 60- $\mu\text{m}$  LF.

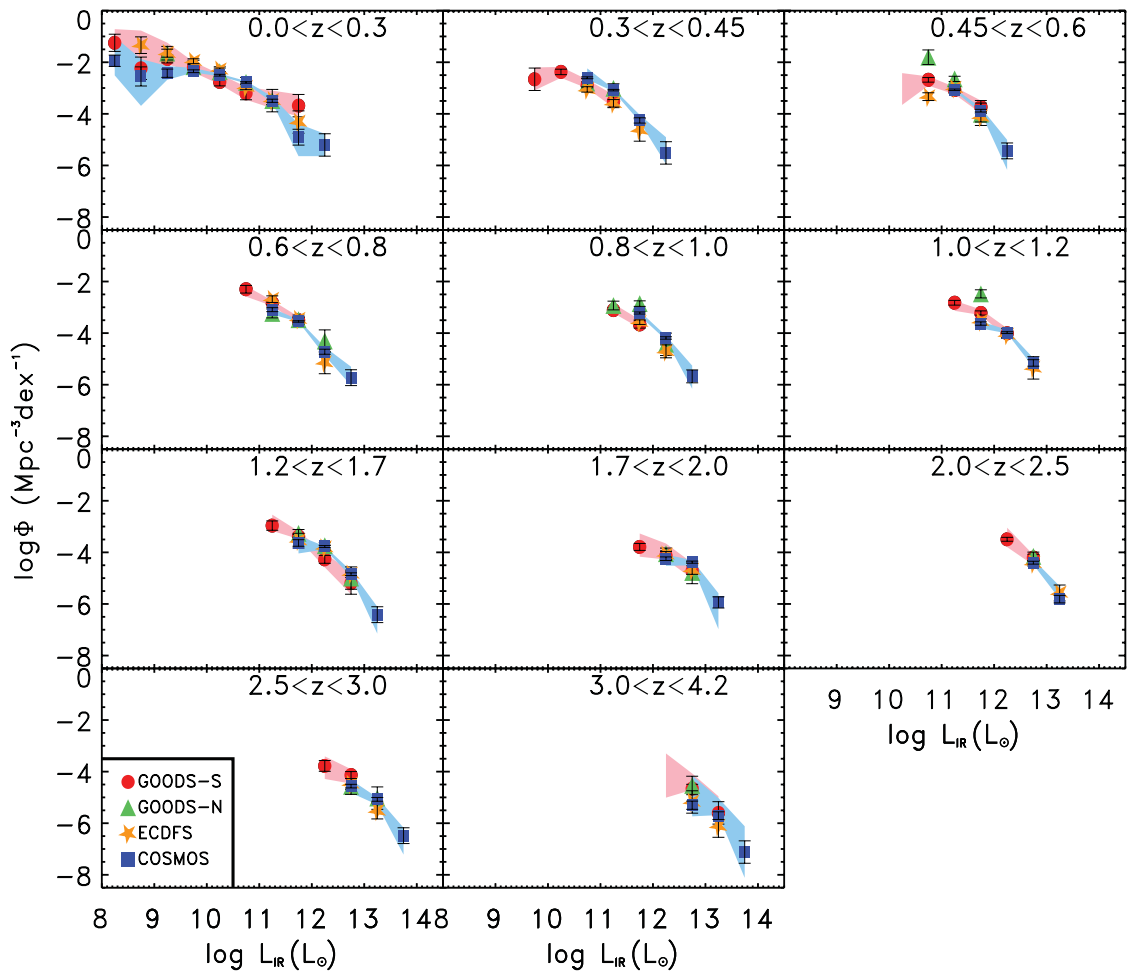
$\log(L_{60}/L_{\odot})$	$\log(\Phi/\text{Mpc}^{-3} \text{ dex}^{-1})$						
	$0.0 \leq z < 0.4$	$0.4 \leq z < 0.8$	$0.8 \leq z < 1.2$	$1.2 \leq z < 1.8$	$1.8 \leq z < 2.5$	$2.5 \leq z < 3.5$	$3.5 \leq z < 4.5$
7.5–7.9	$-1.37 \pm 0.43$						
7.9–8.3	$-1.54 \pm 0.32$						
8.3–8.7	$-1.82 \pm 0.20$						
8.7–9.1	$-1.75 \pm 0.09$						
9.1–9.5	$-2.22 \pm 0.04$						
9.5–9.9	$-2.36 \pm 0.03$	$-2.25 \pm 0.27$					
9.9–10.3	$-2.58 \pm 0.02$	$-2.70 \pm 0.12$					
10.3–10.7	$-2.77 \pm 0.02$	$-2.46 \pm 0.04$					
10.7–11.1	$-3.28 \pm 0.03$	$-3.00 \pm 0.02$	$-2.70 \pm 0.07$				
11.1–11.5	$-4.13 \pm 0.09$	$-3.41 \pm 0.02$	$-3.12 \pm 0.04$	$-3.09 \pm 0.11$			
11.5–11.9	$-4.91 \pm 0.22$	$-4.26 \pm 0.05$	$-3.61 \pm 0.02$	$-3.47 \pm 0.06$	$-3.08 \pm 0.22$		
11.9–12.3		$-5.03 \pm 0.11$	$-4.31 \pm 0.04$	$-3.95 \pm 0.03$	$-3.63 \pm 0.10$	$-3.22 \pm 0.31$	
12.3–12.70		$-6.20 \pm 0.43$	$-5.31 \pm 0.12$	$-4.73 \pm 0.05$	$-4.22 \pm 0.06$	$-4.09 \pm 0.15$	
12.7–13.1				$-5.98 \pm 0.18$	$-5.08 \pm 0.06$	$-4.76 \pm 0.13$	$-4.45 \pm 0.43$
13.1–13.5					$-6.88 \pm 0.43$	$-5.58 \pm 0.22$	$-5.39 \pm 0.43$
13.5–13.9						$-6.93 \pm 0.43$	$-6.20 \pm 0.43$

A clear result of our analysis is that the evolution derived for the global IR LF is indeed a combination of different evolutionary paths: the far-IR population does not evolve all together ‘as a whole’, as it is often assumed in the literature, but is composed by different galaxy classes evolving differently and independently. As shown in Fig. 10, the normal spiral galaxy population dominates the LF at low- $z$ , from the local Universe up to  $z \sim 0.5$ . Moving to higher redshifts, the number density of galaxies with spiral galaxy

SEDs sharply decreases, while their luminosity continues to increase, at least up to  $z \sim 1$  (see the  $\Phi^*$  and  $L^*$  parameter trends shown in Fig. 11). We note that what we observe between  $z \sim 0$  and  $z \sim 1$  for the spiral SED galaxies is an increase of  $L^*$  by a factor of  $\sim 5$ , and a decrease of  $\Phi^*$  by a factor of  $\sim 10$ . Since the two evolutions are not independent, the ‘global’ evolutionary effect results from the combination of the two. By fixing the spiral LF at a given volume density value, we find that the logarithm of

**Table 5.** Combined rest-frame 90- $\mu\text{m}$  LF.

$\log(L_{90}/L_{\odot})$	$\log(\Phi/\text{Mpc}^{-3} \text{dex}^{-1})$						
	$0.0 \leq z < 0.4$	$0.4 \leq z < 0.8$	$0.8 \leq z < 1.2$	$1.2 \leq z < 1.8$	$1.8 \leq z < 2.5$	$2.5 \leq z < 3.5$	$3.5 \leq z < 4.5$
7.9–8.3	$-1.09 \pm 0.31$						
8.3–8.7	$-1.68 \pm 0.21$						
8.7–9.1	$-2.00 \pm 0.15$						
9.1–9.5	$-2.21 \pm 0.07$						
9.5–9.9	$-2.31 \pm 0.04$						
9.9–10.3	$-2.51 \pm 0.03$	$-2.06 \pm 0.24$					
10.3–10.7	$-2.63 \pm 0.02$	$-2.57 \pm 0.05$	$-2.73 \pm 0.18$				
10.7–11.1	$-3.04 \pm 0.03$	$-2.98 \pm 0.02$	$-2.87 \pm 0.08$	$-2.65 \pm 0.22$			
11.1–11.5	$-3.91 \pm 0.07$	$-3.31 \pm 0.02$	$-3.02 \pm 0.05$	$-3.06 \pm 0.12$	$-3.34 \pm 0.20$		
11.5–11.9	$-4.61 \pm 0.15$	$-4.10 \pm 0.04$	$-3.65 \pm 0.02$	$-3.46 \pm 0.05$	$-3.36 \pm 0.10$	$-3.34 \pm 0.31$	
11.9–12.3		$-5.06 \pm 0.12$	$-4.37 \pm 0.04$	$-4.12 \pm 0.03$	$-3.80 \pm 0.08$	$-4.04 \pm 0.15$	$-4.18 \pm 0.31$
12.3–12.7			$-5.76 \pm 0.19$	$-5.02 \pm 0.06$	$-4.26 \pm 0.10$	$-4.55 \pm 0.14$	$-5.39 \pm 0.43$
12.7–13.1				$-6.47 \pm 0.31$	$-5.50 \pm 0.10$	$-5.13 \pm 0.11$	$-5.86 \pm 0.19$
13.1–13.5						$-6.61 \pm 0.43$	


**Figure 6.** Total IR LF estimated independently from the 160- $\mu\text{m}$  samples in the four PEP fields (with the same symbols as in Fig. 4). The pink and sky-blue shaded areas represent the range of values derived with 20 iterations by allowing a change in photo- $z$  in the GOODS-S and COSMOS fields, respectively.

the luminosity corresponding to that value increases by a factor of  $\sim 2.5$  between  $z = 0$  and  $z = 1$ , in good agreement with previous results, either empirical (for morphologically classified discy galaxies; Scarlata et al. 2007) or theoretical (from chemical evolution models of Milky Way-like galaxies; Colavitti, Matteucci & Murante 2008).

Over the whole redshift range 0.5–3, the ‘global’ LF is dominated by the SF-AGN population. The number density of SF-AGN is nearly constant from the local Universe up to  $z \sim 1$ –1.5, showing a slight decrease at higher redshifts, while their luminosities show positive evolution up to the highest redshifts ( $z \sim 3.5$ –4). From Fig. 10 we note a sort of bimodality in the SF-AGN LFs

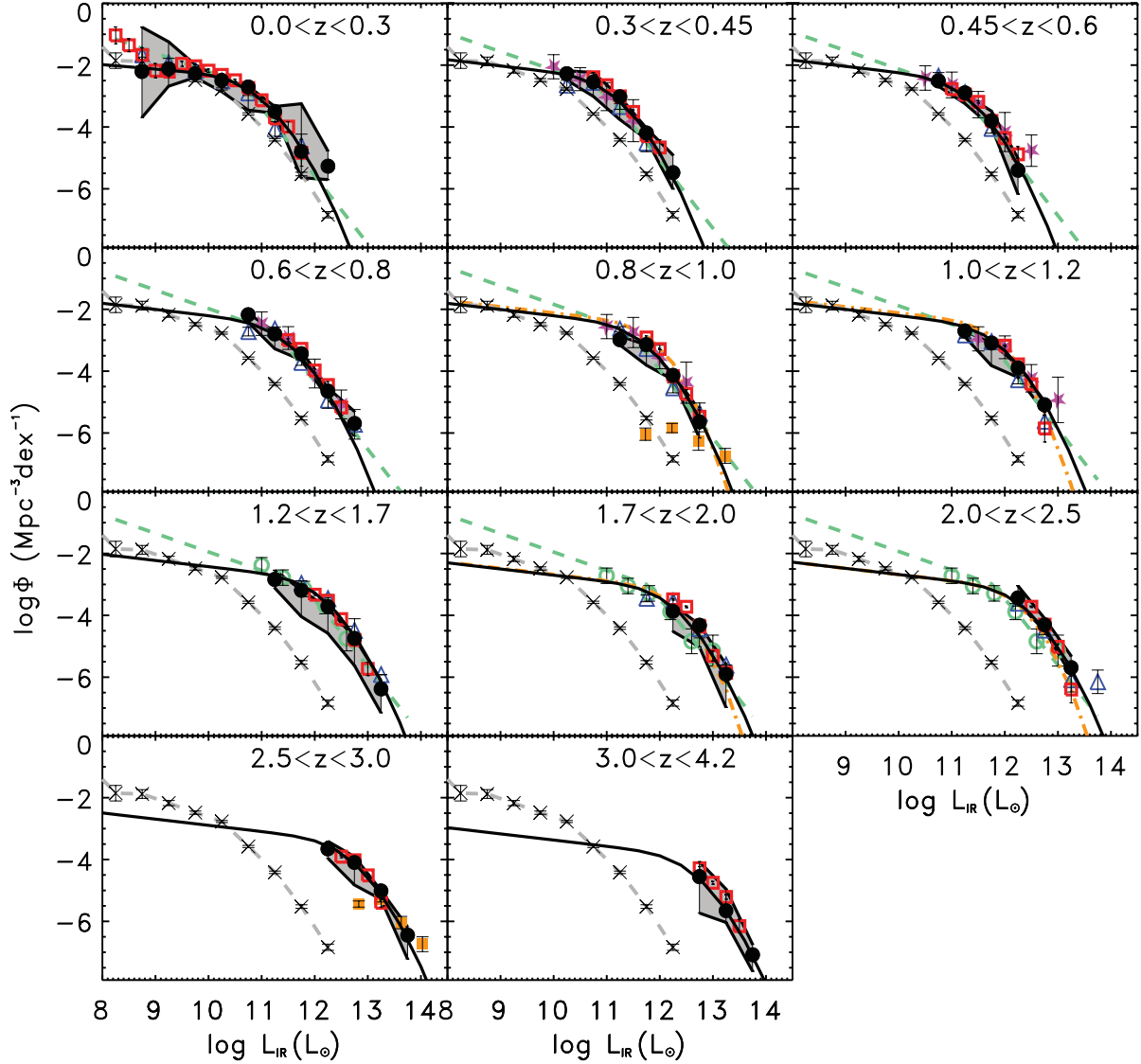


**Figure 7.** Total IR LF estimated by combining the data from the four PEP fields using the Avni & Bahcall (1980) method (black filled circles). The grey filled area shows the uncertainty locus obtained by combining the Poissonian error with the photometric redshift uncertainty derived through Monte Carlo simulations. The black solid line represents our best fit to the PEP data in the different redshift bins, corresponding to the parameters reported in Table 7. Other results from the literature are plotted for comparison (diagonal crosses connected by a grey dashed line, LLF of Sanders et al. 2003; magenta filled stars, Le Floch et al. 2005; orange filled squares, Chapman et al. 2005; orange dot-dashed line, Caputi et al. 2007; blue open triangles, Rodighiero et al. 2010a; green dashed line, Magnelli et al. 2009, 2011; green open circles, Magnelli et al. 2011). Note that the Magnelli et al. (2011) data correspond to slightly different redshift bins:  $1.3 < z < 1.8$  and  $1.8 < z < 2.3$ , respectively. We have therefore plotted the data points corresponding to the first redshift bin in our  $1.2 < z < 1.7$  panel and the data point corresponding to the second redshift bin in both our  $1.7 < z < 2.0$  and  $2.0 < z < 2.5$  panels. The red open squares are the total IR LFs derived by Vaccari et al. (in preparation) from the HerMES 250- $\mu\text{m}$ -selected COSMOS sample.

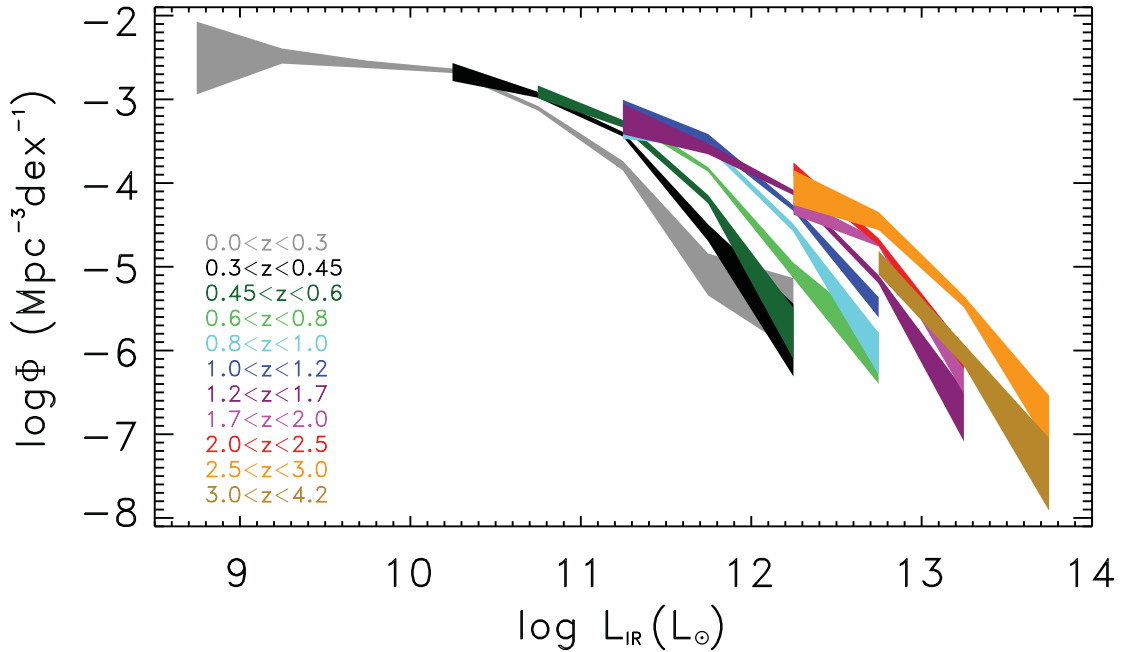
**Table 6.** PEP total IR LF.

$\log(L_{\text{IR}}/L_{\odot})$	$\log(\Phi/\text{Mpc}^{-3} \text{dex}^{-1})$										
	$0.0 \leq z < 0.3$	$0.3 \leq z < 0.45$	$0.45 \leq z < 0.6$	$0.6 \leq z < 0.8$	$0.8 \leq z < 1.0$	$1.0 \leq z < 1.2$	$1.2 \leq z < 1.7$	$1.7 \leq z < 2.0$	$2.0 \leq z < 2.5$	$2.5 \leq z < 3.0$	$3.0 \leq z < 4.2$
8.5–9.0	$-2.21 \pm 0.43$										
9.0–9.5	$-2.18 \pm 0.09$										
9.5–10.0	$-2.28 \pm 0.04$										
10.0–10.5	$-2.50 \pm 0.03$	$-2.37 \pm 0.11$									
10.5–11.0	$-2.71 \pm 0.02$	$-2.64 \pm 0.04$	$-2.61 \pm 0.08$	$-2.27 \pm 0.15$							
11.0–11.5	$-3.49 \pm 0.06$	$-3.12 \pm 0.03$	$-2.99 \pm 0.04$	$-2.89 \pm 0.05$	$-3.09 \pm 0.08$	$-2.80 \pm 0.09$	$-2.93 \pm 0.18$				
11.5–12.0	$-4.79 \pm 0.25$	$-4.29 \pm 0.10$	$-3.89 \pm 0.05$	$-3.53 \pm 0.03$	$-3.24 \pm 0.04$	$-3.17 \pm 0.06$	$-3.29 \pm 0.06$	$-3.76 \pm 0.13$			
12.0–12.5	$-5.27 \pm 0.43$	$-5.58 \pm 0.43$	$-5.50 \pm 0.31$	$-4.75 \pm 0.09$	$-4.23 \pm 0.05$	$-4.00 \pm 0.03$	$-3.81 \pm 0.03$	$-3.96 \pm 0.11$	$-3.53 \pm 0.08$	$-3.75 \pm 0.21$	
12.5–13.0				$-5.79 \pm 0.31$	$-5.74 \pm 0.25$	$-5.18 \pm 0.12$	$-4.85 \pm 0.05$	$-4.42 \pm 0.04$	$-4.40 \pm 0.04$	$-4.15 \pm 0.11$	$-4.65 \pm 0.14$
13.0–13.5							$-6.48 \pm 0.31$	$-6.01 \pm 0.22$	$-5.79 \pm 0.13$	$-5.11 \pm 0.07$	$-5.75 \pm 0.13$
13.5–14.0										$-6.54 \pm 0.31$	$-7.18 \pm 0.43$



**Table 7.** Parameter values describing the curve fitted to the total IR LF.

Redshift range	$\alpha$	$\sigma$	$\log_{10}(L^*/L_{\odot})$	$\log_{10}(\Phi^*/\text{Mpc}^{-3} \text{ dex}^{-1})$
$0.0 < z < 0.3$	$1.15 \pm 0.07$	$0.52 \pm 0.05$	$10.12 \pm 0.16$	$-2.29 \pm 0.06$
$0.3 < z < 0.45$	$1.2^a$	$0.5^a$	$10.41 \pm 0.03$	$-2.31 \pm 0.03$
$0.45 < z < 0.6$	$1.2^a$	$0.5^a$	$10.55 \pm 0.03$	$-2.35 \pm 0.05$
$0.6 < z < 0.8$	$1.2^a$	$0.5^a$	$10.71 \pm 0.03$	$-2.35 \pm 0.06$
$0.8 < z < 1.0$	$1.2^a$	$0.5^a$	$10.97 \pm 0.04$	$-2.40 \pm 0.05$
$1.0 < z < 1.2$	$1.2^a$	$0.5^a$	$11.13 \pm 0.04$	$-2.43 \pm 0.04$
$1.2 < z < 1.7$	$1.2^a$	$0.5^a$	$11.37 \pm 0.03$	$-2.70 \pm 0.04$
$1.7 < z < 2.0$	$1.2^a$	$0.5^a$	$11.50 \pm 0.03$	$-3.00 \pm 0.03$
$2.0 < z < 2.5$	$1.2^a$	$0.5^a$	$11.60 \pm 0.03$	
$2.5 < z < 3.0$	$1.2^a$	$0.5^a$	$11.92 \pm 0.08$	$-3.27 \pm 0.18$
$3.0 < z < 4.2$	$1.2^a$	$0.5^a$	$11.90 \pm 0.16$	$-3.74 \pm 0.30$

<sup>a</sup> Fixed value.

**Figure 8.** Total IR LF estimated by combining the data from the four PEP fields using the Avni & Bahcall (1980) method plotted in all the different redshift intervals considered in this study, from  $z \sim 0$  to  $z \sim 4$ . The different colour filled areas represent the  $\pm 1\sigma$  (Poissonian) uncertainty regions at different redshifts.

(at  $z < 0.45$ , where we are able to cover a larger luminosity range). This bimodality is indeed to be ascribed to the crossing of two contributions: that of the SF-AGN(Spiral) population, responsible for the faint-end steepness of the LFs, and that of the SF-AGN(SB) population, dominating the bright-end of the SF-AGN LFs and declining at low  $L_{\text{IR}}$  (not reported in the figure).

The starburst galaxy population never dominates. The redshift range where we observe the highest contribution from the starburst galaxies is at  $z \sim 1-2$ , while in the local Universe their contribution is almost negligible (i.e. their  $\Phi^*$  parameter shows an opposite trend with respect to that of spiral galaxies, see Fig. 11).

The AGN1 and AGN2 populations show a very similar evolutionary trend as a function of  $z$ , both in  $\Phi^*$  and  $L^*$ . These powerful AGN populations dominate only the very bright end of the total IR LF, although their number densities and luminosities keep increasing from the local Universe up to the higher redshifts. At  $z > 2.5$ , the AGN1 and AGN2 populations become as important as the SF-AGN one, with the total IR LF of PACS-selected sources in the redshift range 2.5–4 being totally dominated by objects containing an AGN.

### 3.6 Total IR LF in mass and sSFR bins

#### 3.6.1 Stellar masses and SFR from SED fitting

The wealth of multiwavelength data available in the cosmological fields included in our work allow us to perform a detailed SED fitting of all sources, in order to derive their most relevant physical parameters (e.g. stellar masses). To derive stellar masses, we have fitted the broad-band spectra of our sources using a modified version of MAGPHYS (da Cunha, Charlot & Elbaz 2008), which is a code describing the SEDs using a combination of stellar light and emission from dust heated by stellar populations. In particular, the MAGPHYS software simultaneously fits the broad-band UV-to-far-IR observed SED of each object, ensuring an energy balance between the absorbed UV light and that re-emitted in the far-IR regime. The main assumptions are that the energy re-radiated by dust is equal to that absorbed, and that starlight is the only significant source of dust heating. We refer to Da Cunha et al. (2008) for a thorough formal description of how galaxy SEDs are built. At each source's redshift, the code chooses among different combinations of SF histories, metallicities and dust contents, associating a wide range of

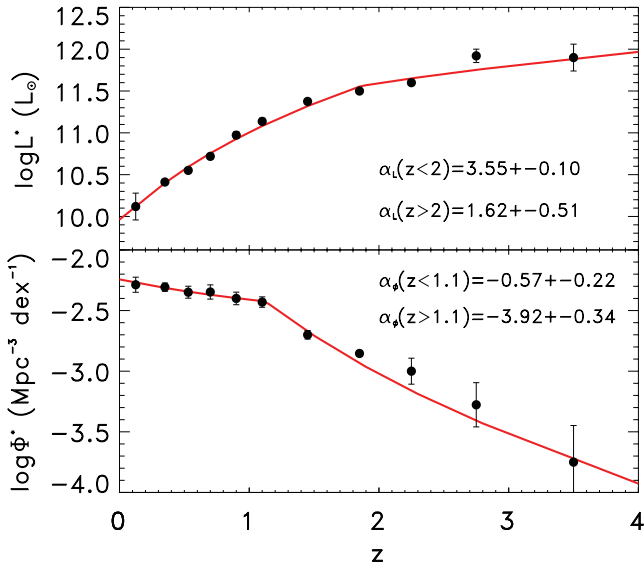


**Figure 9.** Evolution of  $L^*$  and  $\Phi^*$  as function of  $z$  ( $L^* \propto (1+z)^{3.55 \pm 0.10}$  at  $z \lesssim 1.85$ ,  $\propto (1+z)^{1.62 \pm 0.51}$  at  $z \gtrsim 1.85$ ;  $\Phi^* \propto (1+z)^{-0.57 \pm 0.22}$  at  $z \lesssim 1.1$ ,  $\propto (1+z)^{-3.92 \pm 0.34}$  at  $z \gtrsim 1.1$ ).

optical models to a wide range of infrared spectra and comparing to observed photometry, seeking for  $\chi^2$  minimization. Each SF history is parametrized in terms of an underlying continuous model with exponentially declining SFR, on top of which are superimposed random bursts (see Da Cunha et al. 2008, 2010). We note that, although the MAGPHYS assumption of exponentially declining SFR might not be the best to reproduce the SFR history of  $z > 1.5$  star-forming galaxies (i.e. exponentially increasing or increasing SFR would be better choices, as widely discussed by Maraston et al. 2010 and Reddy et al. 2012), in our specific case it does not affect the results. In fact, we do not use the MAGPHYS derived SFRs, but we compute them by integrating the best-fitting SED (resulting from Le Phare). The models are distributed uniformly in metallicity between 0.2 and 2 times the solar. Since the MAGPHYS code assumes that starlight is the only significant source of dust heating, thus ignoring the presence of a possible AGN component, Berta et al. (2013) have developed a modified version of the MAGPHYS code by adding a torus component to the modelled SED emission, combining the Da Cunha et al. (2008) original code with the Fritz, Franceschini & Hatziminaoglou (2006) AGN torus library (see also Feltre et al. 2012).

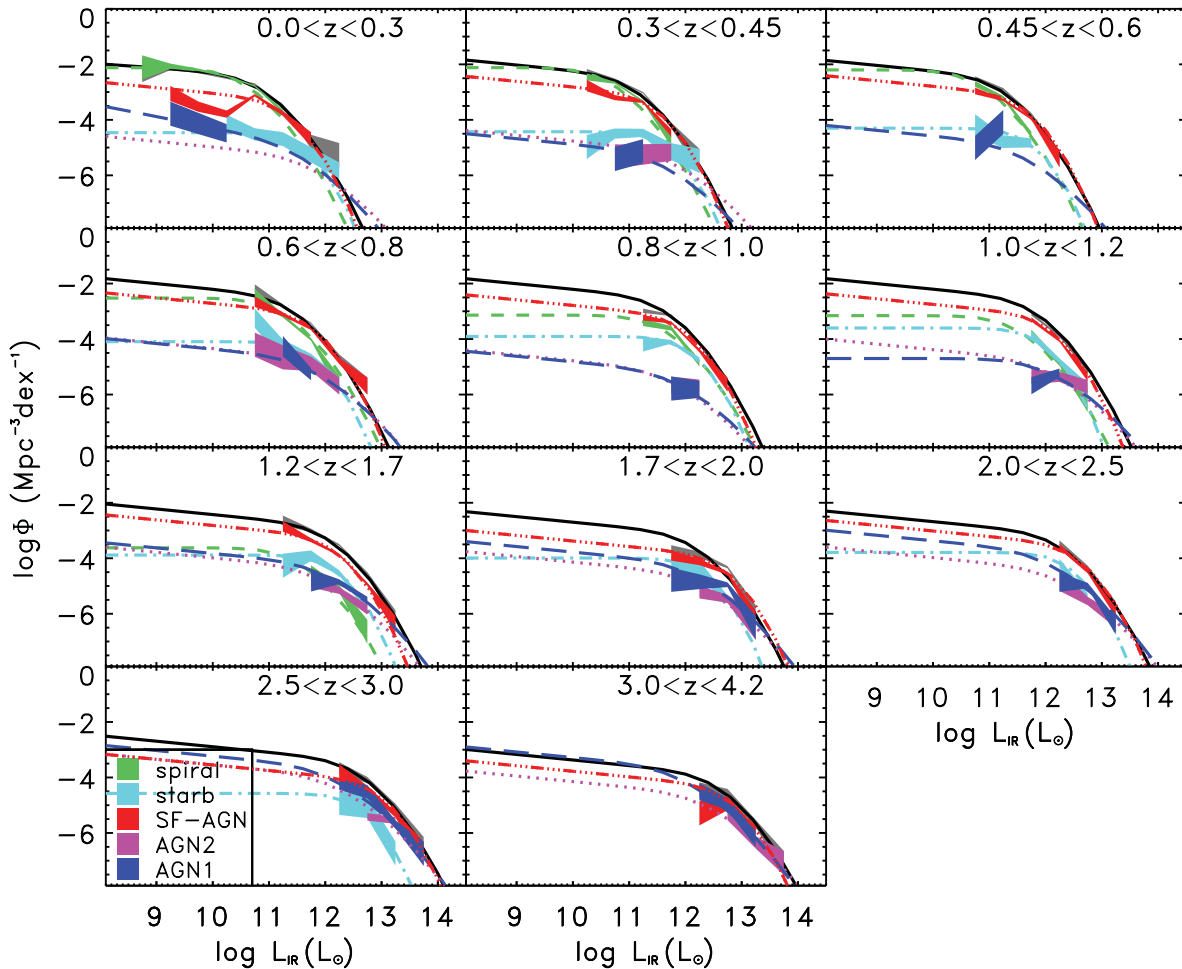


**Figure 10.** Total IR LF estimated with the  $1/V_{\max}$  method by combining the data from the four PEP fields for the different populations (their  $\pm 1\sigma$  uncertainty regions are shown as coloured filled areas: green for spirals; cyan for starbursts; red for SF-AGN; magenta for AGN2 and blue for AGN1), compared to the total LF ( $\pm 1\sigma$ , grey filled area, same as in Fig. 7). The best-fitting modified Schechter functions are also plotted, extrapolated to fainter and brighter luminosities than covered by the data (with the black curve being for the total LF and the same colours used for the filled areas as for the single populations).

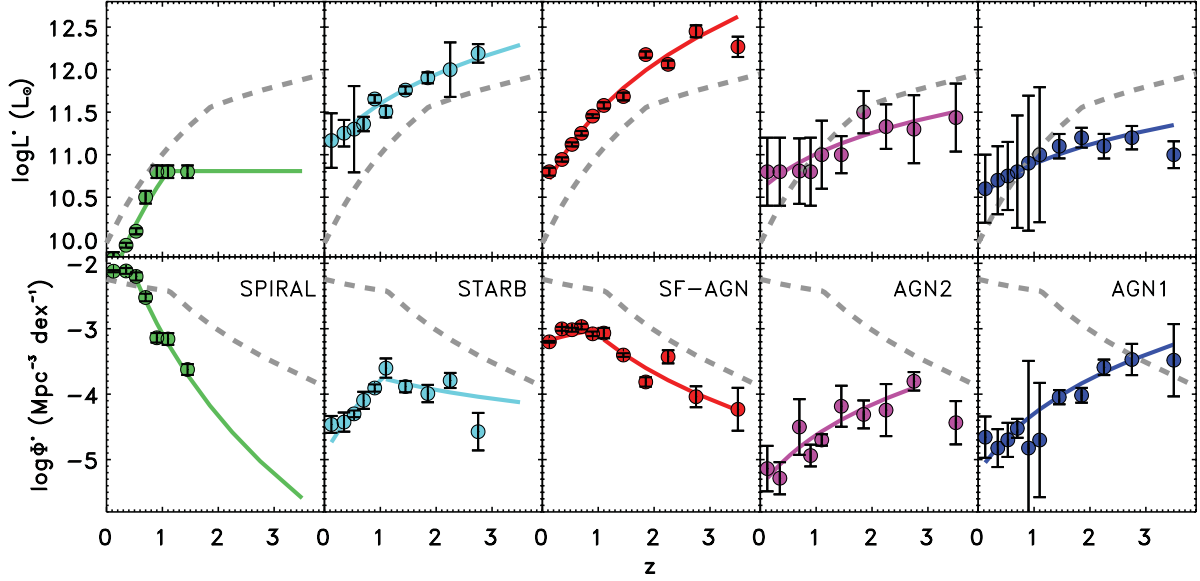


**Figure 11.** Evolution of  $L^*$  (top) and  $\Phi^*$  (bottom) as a function of redshift (in the form  $\propto (1+z)^\alpha$ ) for the different IR populations. For comparison, the  $L^*$  and  $\Phi^*$  evolution of the ‘global’ total IR LF (plotted in Fig. 9) are shown as grey dashed lines.

the quality of each fit. We must point out that the mass derivation for unobscured AGN (i.e. AGN1) is a problematic issue, therefore the masses estimated for that class of objects are the most uncertain ones. One source of uncertainty in the mass measurement for AGN1 is due to the fact that, in these objects, the UV part of the SED is likely dominated by the AGN rather than by the host galaxy. This may produce an underestimate of the mass, since, if the AGN contribution is not taken into account, the data can be fitted by a bluer, younger and smaller mass object. On the other hand, the mid-IR part of the AGN SED is dominated by dust emission from the dusty torus heated by the central black hole. If a proper decomposition into a stellar and a torus component is not performed, the use of a pure stellar template for estimating the mass from SED fitting tends to reproduce the mid-IR emission with an older, redder and larger mass object (mass sometimes larger by a factor of 2 than those derived through a decomposition procedure; Santini et al. 2012). These two effects lead to an increase in the uncertainty of the mass derivation, although they might somewhat compensate their effects for a large sample of objects. Bongiorno et al. (2012) found that for the majority of COSMOS AGN1, the average ratio between the mass derived with and without taking into account the AGN component is  $\sim 1$ , although with a large dispersion, while for  $\sim 50$  per cent the mass is underestimated by factors as high as 3–10 if the AGN contribution is not taken into account. For this reason, we obtained measurements of the stellar masses of our objects containing an AGN by means of the specific decomposition technique developed by Berta et al. (2013), to separate stellar and nuclear emission com-

ponents. Examples of the results of this decomposition applied to SF-AGN, AGN2 and AGN1 are shown in Fig. 12. Masses of AGN estimated with the original MAGPHYS and with the Berta et al. (2013) code have been compared, showing very good agreement and small dispersion around the 1–1 relation. Similarly, as further check, we have also computed stellar masses with different code (HYPERZ; Bolzonella, Miralles & Pelló 2000) and stellar library (BC03, Bruzual & Charlot 2003, instead of the CB07 used as default by MAGPHYS), finding good agreement and no systematics, too.

We have derived the SFRs from the total IR luminosities (estimated from the SED fitting described in Section 2.1) with the standard Kennicutt (1998) relation (converted to Chabrier IMF), after subtracting the AGN contribution to  $L_{\text{IR}}$ . We note that the total IR luminosity in PEP sources is usually dominated by SF, even in objects for which an AGN dominates the optical/near-IR/mid-IR part of the spectrum.

### 3.6.2 LFs in different mass bins

We compute the total IR LF for galaxies of different stellar masses:  $8.5 \leq \log(M/M_\odot) < 10$ ,  $10 \leq \log(M/M_\odot) < 11$  and  $11 \leq \log(M/M_\odot) < 12$ , by means of the standard  $1/V_{\text{max}}$  formalism, and we show the results in Figs 13 (total IR LF in different  $z$ -bins) and 14 (ratio between the LF in the mass intervals and the total IR LF). We have compared our results with the SFR function [SFR converted to IR luminosity using the Kennicutt (1998) relation] of massive ( $\log(M/M_\odot) > 10$ ) galaxies derived by Fontanot

**Table 8.** Parameter values describing the curve fitted to the total IR LF of the different SED populations.

	$\alpha$	$\sigma$	$\log_{10}(L^*/L_\odot)$	$\log_{10}(\Phi^*/\text{Mpc}^{-3} \text{dex}^{-1})$	$k_{L,1}$	$k_{L,2}$	$z_{b,L}$	$k_{\rho,1}$	$k_{\rho,2}$	$z_{b,\rho}$
	(0.0 < z < 0.3)									
Spiral	$1.00 \pm 0.05$	$0.50 \pm 0.01$	$9.78 \pm 0.04$	$-2.12 \pm 0.01$	$4.49 \pm 0.15$	$0.00 \pm 0.46$	1.1	$-0.54 \pm 0.12$	$-7.13 \pm 0.24$	0.53
Starburst	$1.00 \pm 0.20$	$0.35 \pm 0.10$	$11.17 \pm 0.16$	$-4.46 \pm 0.06$	$1.96 \pm 0.13$			$3.79 \pm 0.21$	$-1.06 \pm 0.05$	1.1
SF-AGN	$1.20 \pm 0.02$	$0.40 \pm 0.10$	$10.80 \pm 0.02$	$-3.20 \pm 0.01$	$3.17 \pm 0.04$			$0.67 \pm 0.05$	$-3.17 \pm 0.15$	1.1
AGN2	$1.20 \pm 0.20$	$0.70 \pm 0.20$	$10.80 \pm 0.20$	$-5.14 \pm 0.17$	$1.41 \pm 0.33$			$2.65 \pm 0.32$		
AGN1	$1.40 \pm 0.30$	$0.70 \pm 0.20$	$10.50 \pm 0.20$	$-5.21 \pm 0.11$	$1.31 \pm 0.02$			$3.00 \pm 0.25$		

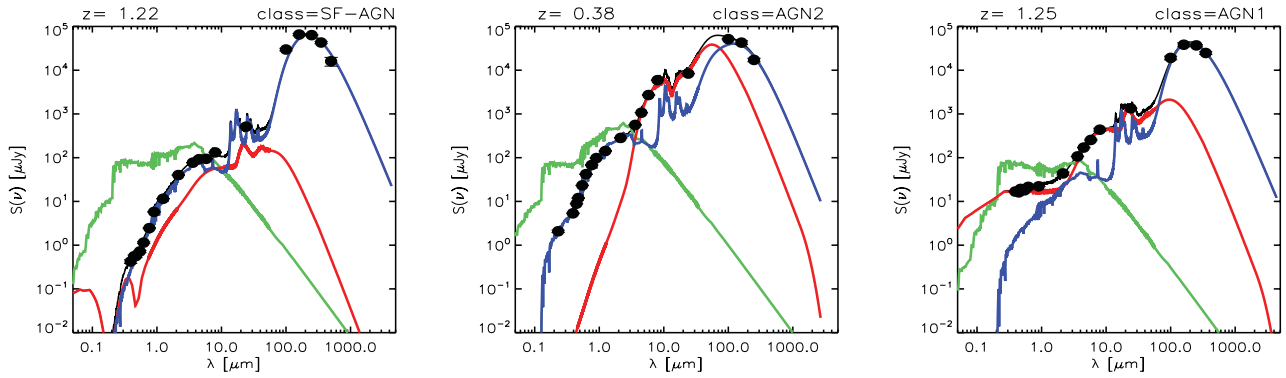


**Figure 12.** Examples of PEP AGN SEDs fitted by the *MAGPHYS* code (Da Cunha et al. 2008) modified by Berta et al. (2013) to add an AGN component from the Fritz et al. (2006) library. From left to right the result of the fit to an SF-AGN, an AGN2 and an AGN1 is shown. The stellar component unattenuated by dust is shown in green, while the dust-attenuated spectrum with dust IR re-emission is shown in blue. The AGN contribution is shown in red, while the black curve represents the total fitted spectrum, obtained from the sum of the blue and red components. Our data are represented by the black dots.

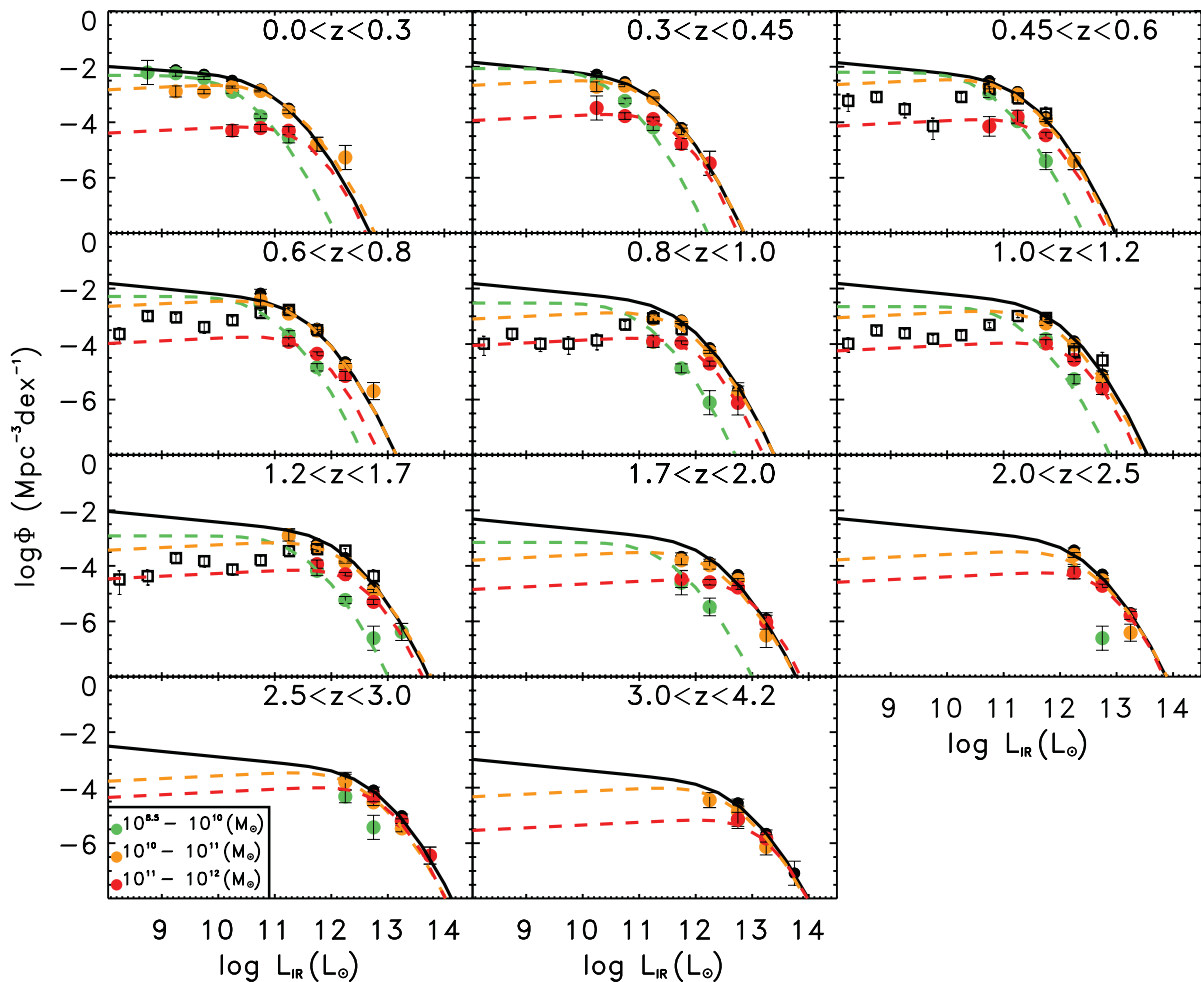


**Figure 13.** Contribution to the total IR LF from galaxies in three different mass intervals:  $8.5 < \log(M/M_{\odot}) < 10$  (green);  $10 < \log(M/M_{\odot}) < 11$  (orange) and  $11 < \log(M/M_{\odot}) < 12$  (red). For comparison, the SFR function of  $\log(M/M_{\odot}) > 10$  sources in the GOODS-S by Fontanot et al. 2012 (converted to total IR LF) is shown as black open squares.

et al. (2012) from the GOODS-MUSIC sample at redshift  $0.4 < z < 1.8$ . In the common redshift and luminosity range, we find an excellent agreement with our total IR LF, which is dominated by sources with  $10 < \log(M/M_{\odot}) < 11$ . At lower luminosities, not sampled by our data, the Fontanot et al. (2012) LFs are characterized by a double-peaked structure, interpreted in terms of

the well-known bimodality in the colour(SFR)–mass diagram. As expected from the SFR–mass relation, the knee ( $L^*$ ) of our IR LFs in different mass bins moves to higher luminosities with increasing masses [i.e. at  $0.0 < z < 0.3$ ,  $\log(L^*/L_{\odot})$  changes from  $\sim 9.5$  for  $\log(M/M_{\odot}) = 8.5-10$  sources, to  $\sim 11.3$  for sources with  $\log(M/M_{\odot}) > 11$ ].



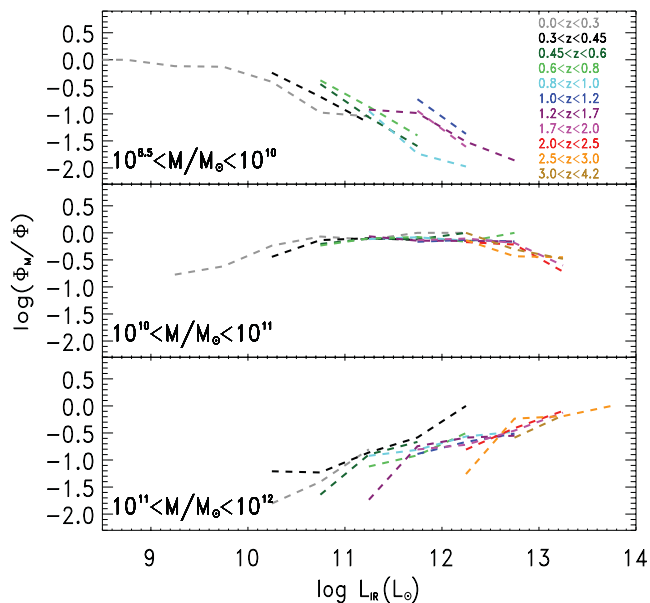


**Figure 14.** Ratio between the IR LF of galaxies in three different mass intervals:  $8.5 < \log(M/M_\odot) < 10$  (top);  $10 < \log(M/M_\odot) < 11$  (middle) and  $11 \leq \log(M/M_\odot) < 12$  (bottom), as shown in Fig. 13, and the total IR LF, plotted in all the different redshift intervals considered in this study, from  $z \sim 0$  to  $z \sim 4$ . The different colours represent the different redshifts, as explained in the plot.

The slope of the total IR LF in each mass bin is always similar to (or flatter than) the ‘global’ LF (total, including all the masses). The lower mass galaxies dominate at lower luminosities [ $\log(L/L_\odot) < 9$ ], while the most massive galaxies [ $\log(M/M_\odot) > 11$ ] contribute only at higher luminosities, even if they never dominate the LF. At all masses, the LF evolves with redshift, following the evolution of the ‘global’ LF. Fig. 14 shows that the main contribution (>50 per cent) to the total IR LF is due to intermediate-mass objects [ $\log(M/M_\odot) = 10$ –11] at all redshifts and luminosities, with their fraction remaining almost the same from  $z = 0$  to  $z \sim 4$ , simply shifting to higher luminosities. Lower mass objects [ $\log(M/M_\odot) = 8.5$ –10] contribute significantly only at  $\log(L/L_\odot) < 10$ , with their fraction just shifting to higher luminosities with redshift, but always being below 30 per cent at  $z > 0.45$  and  $\log(L/L_\odot) > 11$ . The contribution of the most massive objects [ $\log(M/M_\odot) = 11$ –12] increases with IR luminosity and redshift, becoming significant (>50 per cent) only at  $z > 1.7$  and  $\log(L/L_\odot) > 12.5$ .

### 3.7 Specific-SFR and the MS of star-forming galaxies

Having computed stellar masses and SFRs for each source, we can check how the PACS-selected sources populate the SFR–stellar mass plane and the so called main sequence (MS) of star-forming galaxies, as a function of redshift. This relation (i.e. SFR versus stellar mass) has been shown to be quite tight in the local Universe (Peng et al. 2010, 2011) and well established at redshift  $z \sim 1$  (Elbaz et al. 2007) and up to  $z \sim 2$  (Daddi et al. 2007; Rodighiero et al. 2011) and  $z \sim 3$  (Magdis et al. 2010), with normalization scaling as  $\sim (1+z)^{2.8}$  out to  $z \sim 2$ , as shown by Sargent et al. (2012) (see also Elbaz et al. 2007; Pannella et al. 2009; Rodighiero et al. 2010b; Karim et al. 2011). At  $z \sim 2$  and  $\sim 1.5$ , we assume a slope of 0.79 for the MS in the SFR versus stellar-mass plane (according to Rodighiero et al. 2011 and Sargent et al. 2012), while at  $z \sim 1$

we assume a slope of 0.9, as found by Elbaz et al. (2007), and we limit our investigation to the redshift range  $0.8 < z < 2.2$ .

By combining UV and far-IR data, Rodighiero et al. (2011) re-evaluated the locus of the MS at  $z \sim 2$ , showing that objects lying a factor of 4 above the MS (in SFR) can be considered as outliers with respect to the average locus where smoothly star-forming galaxies spend most of their lives in a secular and steady regime. In that work, off-sequence sources (characterized by very high sSFRs) are assumed to be in a starburst mode, and are found to contribute only 2 per cent of mass-selected star-forming galaxies and to account for only 10 per cent of the cosmic SFR density at  $z \sim 2$  (Rodighiero et al. 2011).

In order to check what kind of objects we could classify as on-MS and off-MS sources in our IR sample compared to previous findings, either based or not based on IR surveys (e.g. Rodighiero et al. 2011; Sargent et al. 2012), we have split our sample into off-MS and on-MS. For consistency with previous studies, we have applied the same criterion as Rodighiero et al. (2011) (0.6 dex above the MS) over the whole  $0.8 < z < 2.2$  redshift range, by using as a reference MS the relation found by Rodighiero et al. (2011) at  $z \sim 2$ , scaled as described above at  $z \sim 1.5$ , and the relation found by Elbaz et al. (2007) at  $z \sim 1$ . In Fig. 15, we show the SFR versus stellar mass distributions in three redshift bins ( $0.8 < z < 1.25$ ,  $1.25 < z < 1.8$  and  $1.8 < z < 2.2$ ), for the PACS sources included in the computation of the luminosity functions presented in this work. The colour code marks the different SED-classes to which each source belongs. We also report the typical loci of the MS at the various redshifts [scaling as  $(1+z)^{2.8}$ , as mentioned above]. Details are given in the caption to the figure. The typical far-IR selection bias (PACS-*Herschel* in this case) appears as an approximate horizontal SFR cut (Rodighiero et al. 2011, Wuyts et al. 2011), shown as thin dotted line in Fig. 15. We note that the trends of mid/far-IR SEDs with offset from the main sequence observed in Fig. 15 (and widely discussed in Section 5) are in good agreement with the results of Elbaz et al. (2011) and Nordon et al. (2012).

With the selection presented in Fig. 15 (sources qualify as ‘off-MS’ if they lie more than 0.6 dex above the observed SFR–stellar mass relation), we can compute the contribution of off-MS (also called ‘starburst’ in the literature) and on-MS (‘steady star-formers’ in the literature) sources to the total IR LFs. This is presented in Fig. 16, where the total IR LFs of on-MS and off-MS sources have been computed independently for the three redshift bins. The pink and yellow filled areas correspond to the  $\pm 1\sigma$  uncertainty regions of the total IR LFs estimated for the on-MS and off-MS populations, respectively, while the black filled area marks the global population. Our results are compared with the recent predictions by Sargent et al. (2012), a non-parametric approach that is based on three basic observables: the redshift evolution of the stellar MF for star-forming galaxies; the evolution of the sSFR of MS galaxies and a double-Gaussian decomposition of the sSFR distribution at fixed stellar mass into a contribution (assumed redshift- and mass-invariant) from MS and off-MS (i.e. starburst) activity. The evolution of the two populations found both in our data and the Sargent et al. (2012) model are very similar. Both data and predictions indicate that the bright-end of the total IR LF is dominated by off-MS sources. However, although consistent within the uncertainties, the relative contribution of off-MS sources seems to be stronger in the Sargent et al. (2012) model than observed in the present computation, where we find that the bright-ends of the PEP IR LFs are more similarly populated by MS and off-MS sources (especially at  $z \sim 2$ ). This difference can be at least partly ascribed to the sharp cut we apply to separate MS from off-MS sources, while Sargent et al. (2012)

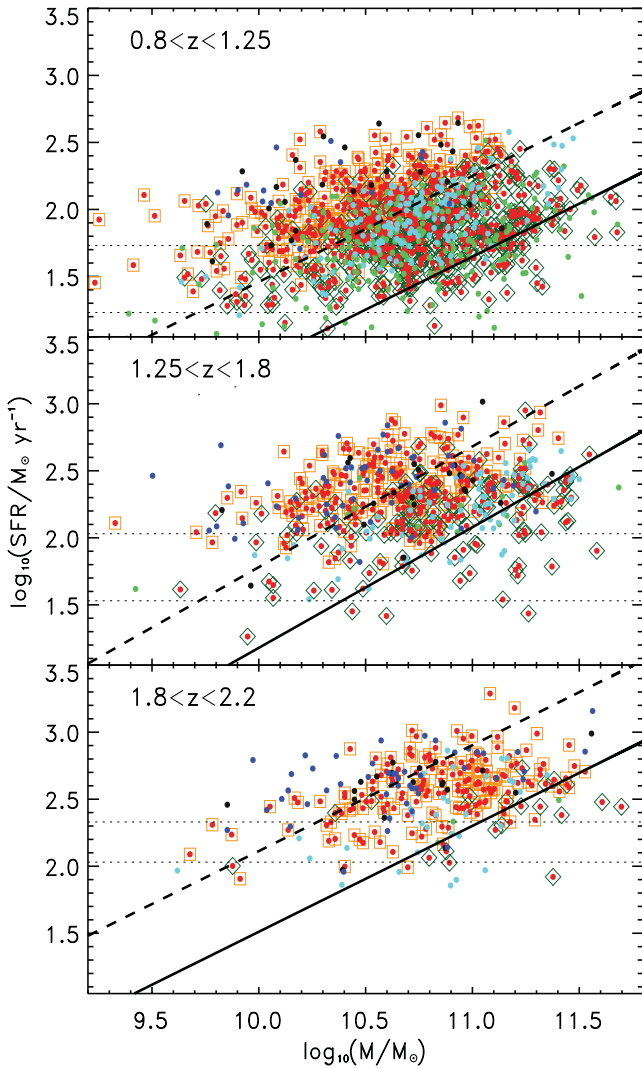


**Figure 15.** SFR versus stellar mass for our PEP 160- $\mu\text{m}$  sources (green, spiral; cyan, starburst; red, SF-AGN; magenta, AGN2; blue, AGN1), in three redshift bins (from left to right):  $0.8 < z < 1.25$ ;  $1.25 < z < 1.8$  and  $1.8 < z < 2.2$ . The relation known as MS is plotted as a solid line (from Elbaz et al. 2007 in the lower redshift bin, rescaled as  $(1+z)^{2.8}$  in the central bin and from Rodighiero et al. 2011 at  $z \sim 2$ ), while the dashed line shows the same relation 0.6 dex higher, indicating the separation between MS and above MS objects adopted by Rodighiero et al. (2011). The horizontal dotted lines show the nominal SFR limits of the GOODS-S (lower) and COSMOS (upper) samples in the different redshift intervals. The orange open squares and the dark-green open diamonds mark the two sub-classes of SF-AGN galaxies: the SF-AGN(SB) and SF-AGN(Spiral), respectively.

model the off-MS and on-MS populations with two continuous log-normal distributions centred at 0.6 dex above the MS and exactly on the MS respectively, of which the one describing the ‘starburst’ population has wings that extend into our on-MS selection region (hence attributing more sources to the starburst category than are selected in our off-MS class). Better agreement between our data and the predictions of Sargent et al. (2012) is found at the faint-end of the LFs that appear to be completely dominated by the ‘normal’ MS galaxies at all redshifts (although the total and relative contributions at  $\log(L_{\text{IR}}/L_{\odot}) < 12$  are slightly lower in the data than predicted by Sargent et al. 2012). Good agreement is also found with respect to the evolution of the cross-over luminosity (i.e.

where the contributions from on-MS and off-MS sources are equal); in the model of Sargent et al. (2012), the cross-over luminosity simply shifts to higher luminosities and lower densities (according to the luminosity and density evolution considered). Note that the model assumptions rely on results from different surveys, selected at different wavelengths, complete in mass and with good sampling of the MS. On the other hand, our selection is in SFR and our sources do not follow any clear sequence in stellar mass–SFR. These different selection effects are highly likely to lead to also some differences between our LFs and the predictions of Sargent et al. (2012).

To quantify the relative contribution of the two populations, our observed data have been fitted with a modified Schechter function, in order to integrate them and compute their comoving number and luminosity densities as functions of redshift (see the next section).

#### 4 NUMBER DENSITY AND IR LUMINOSITY DENSITY

We derive the evolution of the comoving number and luminosity density (total, see Fig 18) of the PEP sources, either belonging to the different SED classes (Fig 18, left), to the on-MS and off-MS categories (middle) and to the different mass intervals (right), by integrating the total IR LF in the different redshift bins from  $z \sim 0$  to  $z \sim 4$ . To compute the number (and IR luminosity) density, we integrate the Schechter functions that best reproduce the different populations/mass/sSFR-classes, down to  $\log(L/L_{\odot}) = 8$ . We note that here we consider lower limits the number and luminosity densities at  $3.0 < z < 4.2$ , since our LF estimate in that redshift bin is likely to be incomplete, as discussed in Section 3.3. We find that the number density of the whole IR population is nearly constant in the  $z = 0\text{--}1.2$  redshift range (slightly increasing from  $z \sim 0$  to  $z \sim 0.5$ ), decreasing at  $z > 1.2$  (see top panels of Fig. 18). When decomposing the number density according to the different SED classes, we observe that normal spiral galaxies dominate the local density, with a smaller contribution also from the SF-AGN population and a negligible one from starburst, AGN1 and AGN2. The space density of spiral galaxies decreases rapidly at  $z \geq 0.5$ , while that of SF-AGN keeps nearly constant at  $0.5 \lesssim z \lesssim 2.5$ , largely dominating in that redshift range. Starburst galaxies never dominate, while the number density of the bright AGN (both AGN1 and AGN2) increases with redshift, from  $\sim 10^{-4} \text{ Mpc}^{-3}$  at  $z \sim 0$  to  $\sim 1\text{--}2 \times 10^{-3} \text{ Mpc}^{-3}$  at  $z \sim 3$ . At higher redshifts the AGN population largely dominates the number density.

If the overall contribution to the IR luminosity density ( $\rho_{\text{IR}}$ ) from the AGN components of galaxies is small,  $\rho_{\text{IR}}$  can be considered as a proxy of the SFR density ( $\rho_{\text{SFR}}$ ). As a further check, we have therefore studied the evolution of the SF-AGN population (which dominates the distribution of sources) by dividing this class into SF-AGN(SB) and SF-AGN(Spiral) sub-classes and studying their evolution separately. Indeed, we have found different evolutionary paths for the two populations, the former dominating at higher redshifts and showing a behaviour similar to that of AGN-dominated sources (e.g. AGN1 and AGN2), the latter dominating at intermediate redshifts (between  $z \sim 1$  and 2), rising sharply from  $z \sim 2$  towards the lower redshifts and decreasing as the spiral population rises at  $z \lesssim 1$ . These evolutionary trends, in terms of number and luminosity density, have been reported in Fig. 18 as orange solid [SF-AGN(SB)] and dark-green dashed [SF-AGN(Spiral)] curves.

Galaxies following the SFR–mass relation are always dominant over the off-MS population, at all redshifts (although their space density decreases with increasing  $z$ , as well as the ‘global’ number

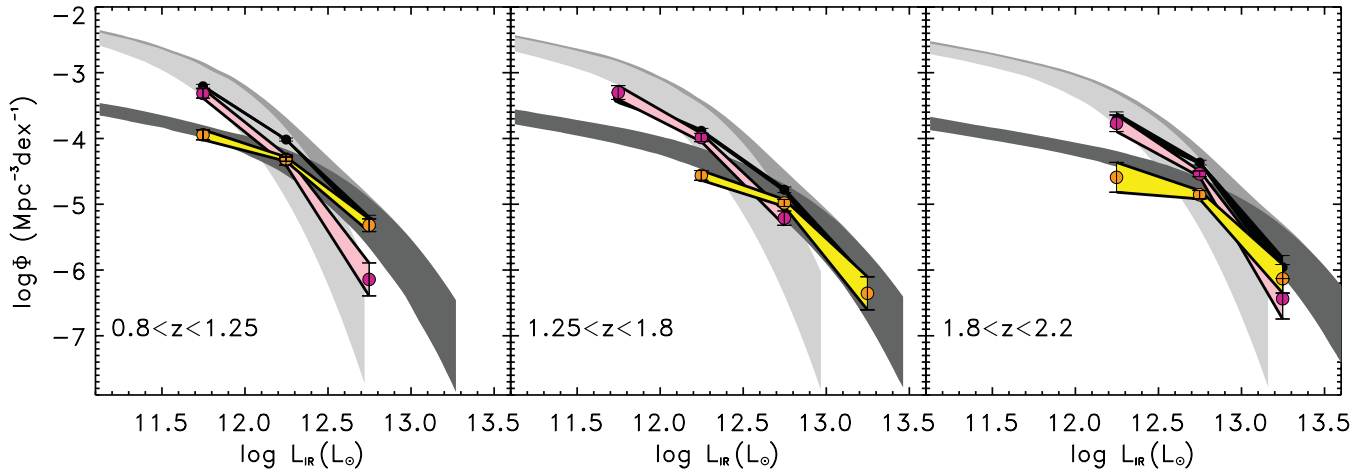


**Figure 16.** Contribution of MS ( $\pm 1\sigma$  uncertainty region: pink shaded area) and off-MS ( $\pm 1\sigma$  uncertainty region: yellow shaded area) galaxies to the total IR LF (black filled dots and area) in three different redshift bins. For comparison, the recent predictions of Sargent et al. (2012) in similar  $z$ -bins are shown as grey (total, in background), light grey (MS) and dark grey (off-MS) filled regions.

density), while the number density of the latter population remains nearly constant between  $z \sim 0.8$  and  $z \sim 2.2$ .

In all the mass bins, the trends with redshift of the galaxy number densities are similar to the ‘global’ one, decreasing at higher redshifts, although with slightly different slopes for the different mass intervals. The number densities of low-mass galaxies [ $8.5 < \log(M/M_\odot) < 10$ ], reported in the top-right panel of Fig. 18, have been computed by integrating the best-fitting modified Schechter function only to  $z \sim 2$ , since data were not enough to derive reliable fits at higher redshifts. To this redshift, these sources outnumber the higher mass ones, although they fall steeply above  $z \sim 1$ , when they reach about the same volume density of higher mass galaxies [ $10 < \log(M/M_\odot) < 11$ ]. Massive objects [ $\log(M/M_\odot) > 11$ ] never dominate (always below 5 per cent) the total number density.

The total IR LF allows a direct estimate of the total comoving IR luminosity density ( $\rho_{\text{IR}}$ ) as a function of  $z$ , which is a crucial tool for understanding galaxy formation and evolution. Although  $\rho_{\text{IR}}$  can be converted to an SFR density ( $\rho_{\text{SFR}}$ ) under the assumption that the SFR and  $L_{\text{IR}}$  quantities are connected by the Kennicutt (1998) relation, before doing that we must be sure that the total IR luminosity is produced uniquely by SF, without contamination from an AGN. The SED decomposition and separation into AGN and SF contributions show a negligible contribution to  $L_{\text{IR}}$  (<10 per cent) from the AGN in most of the SF-AGN, and an SF component dominating the far-IR even in the majority of more powerful AGN (AGN1 and AGN2). Here, we prefer to speak in terms of  $\rho_{\text{IR}}$  rather than of  $\rho_{\text{SFR}}$ , since, especially at high redshift – where the AGN-dominated sources are more numerous – the conversion of  $\rho_{\text{IR}}$  could represent only an upper limit to  $\rho_{\text{SFR}}$ . Note, however, that since this population is never dominant in our IR survey, we do not expect that contamination related to accretion activity occurring in these objects (mainly at high- $z$ ) can significantly affect the results in terms of  $\rho_{\text{SFR}}$ .

In Fig. 17, we show  $\rho_{\text{IR}}$  estimated from our total IR LF and compare it with results obtained from previous IR surveys (Le Floc’h et al. 2005; Caputi et al. 2007; Rodighiero et al. 2010a; Magnelli et al. 2011). In the common redshift intervals ( $0 \lesssim z \lesssim 2-2.5$ ), we find very close agreement with previous results based on IR data, especially with the Magnelli et al. (2011) derivation. As well as previous findings,  $\rho_{\text{IR}}$  from PEP shows the rapid rise from  $z \sim 0$  to  $z \sim 1$ , followed by a flattening at higher redshifts. The indications from

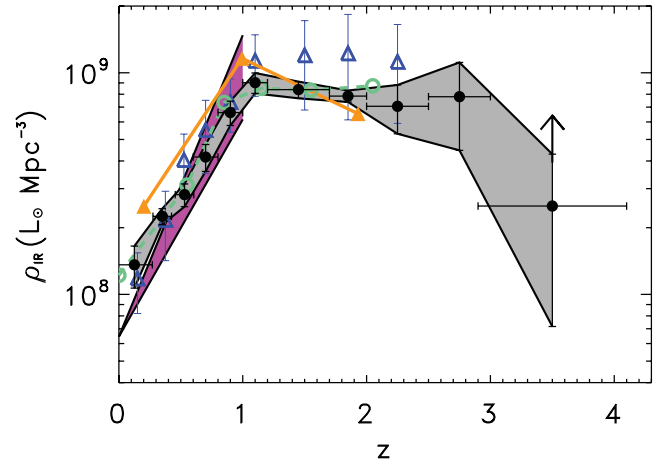


**Figure 17.** Redshift evolution of the total IR luminosity density ( $\rho_{\text{IR}}$ , obtained by integrating the modified Schechter functions that best reproduce the total IR LF down to  $\log(L/L_\odot) = 8$ ) to  $z = 4$ . The results of integrating the best-fitting curve for our observed total IR LF in each  $z$ -bin are shown as black filled circles (the grey filled area represents the  $\pm 1\sigma$  uncertainty locus) and compared with estimates from previous mid-IR surveys (magenta filled area, Le Floc’h et al. 2005; orange filled triangles, Caputi et al. 2007; blue open triangles, Rodighiero et al. 2010a and green open circles, Magnelli et al. 2011). The upward pointing arrow in the highest- $z$  bin means that, due to the large fraction of photometric redshifts and the fact that the PEP selection might miss high- $z$  sources, our  $3.0 < z < 4.2$   $\rho_{\text{IR}}$  estimate is likely to be a lower limit.

our survey are that the intermediate-redshift flattening is followed by a high-redshift decline, which starts around  $z \sim 3$ . From our data,  $\rho_{\text{IR}}$  evolves as  $(1+z)^{3.0 \pm 0.2}$  up to  $z \sim 1.1$ , as  $(1+z)^{-0.3 \pm 0.1}$  from  $z \sim 1.1$  to  $z \sim 2.8$ , and then as  $(1+z)^{-6.0 \pm 0.9}$  up to  $z \sim 4$ .

In the bottom panels of Fig. 18, we plot the different contributions to  $\rho_{\text{IR}}$  from the different SED populations (left), from the on-MS and off-MS sources (middle) and from the different mass intervals. We notice a predominance of spiral-SED galaxies only at low redshifts ( $z < 0.5-0.6$ ), when SF-AGN begin to dominate  $\rho_{\text{IR}}$  up to  $z \sim 2.5$ . The starburst SED galaxies are never the prevalent population, although their contribution to  $\rho_{\text{IR}}$  increases rapidly from the local Universe to  $z \sim 1$ , then keeps nearly constant to

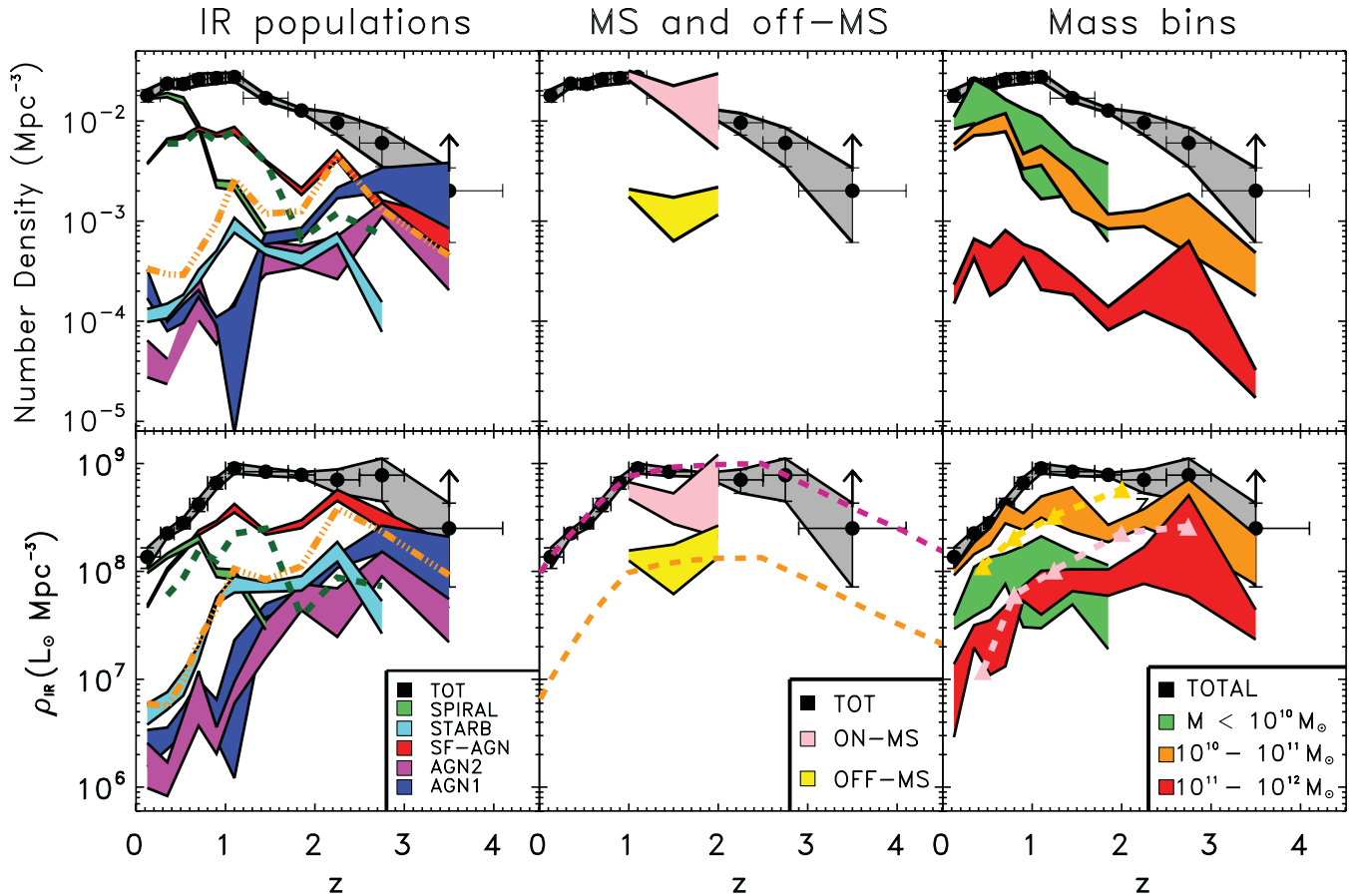


**Figure 18.** Top: evolution of the comoving number density of PEP sources up to  $z \sim 4$  (black filled circles with error bars within the  $\pm 1\sigma$  uncertainty region, represented by the grey filled area). The upward pointing arrow in the highest- $z$  bin means that our  $3.0 < z < 4.2$  estimates are likely to be lower limits. Bottom: redshift evolution of the total IR luminosity density to  $z = 4$ . To compute the number and IR luminosity density, we integrate the modified Schechter functions that best reproduce the different populations/mass/sSFR-classes, down to  $\log(L/L_{\odot}) = 8$ . The black filled circles and the grey dashed area in all the three panels represent our PEP derived  $\rho_{\text{IR}}$  and its  $\pm 1\sigma$  uncertainty region, as shown in Fig. 17. In the left-hand panels, we show the number (top) and luminosity density (bottom) of the different IR populations (green filled area, spiral; cyan, starburst; red, SF-AGN; magenta, AGN2; and blue, AGN1). The contribution of SF-AGN sources, sub-divided on the basis of their SED resemblance to spiral or starburst templates, is shown by the dark-green dashed [SF-AGN(Spiral)] and orange solid [SF-AGN(SB)] lines, respectively. In the middle panels, we show the uncertainty regions of the relative contribution to number and luminosity density of the sources on- and off- the SFR–stellar mass MS (Daddi et al. 2007; Elbaz et al. 2007), as pink and yellow filled areas, respectively. Our derivations have been compared to those of Bethermin et al. (2012) for on-MS and off-MS sources (converted from  $\rho_{\text{SFR}}$  to  $\rho_{\text{IR}}$  using the Kennicutt 1998 relation), which are represented by the purple and orange dashed lines, respectively. In the right-hand panels, we show the relative contribution to the number and luminosity density of sources with different masses (green,  $8.5 < \log(M/M_{\odot}) < 10$ ; orange,  $10 < \log(M/M_{\odot}) < 11$ ; and red,  $11 < \log(M/M_{\odot}) < 12$ ). For comparison, in the bottom-right panel, we plot also the results of Santini et al. (2009) in the GOODS-S field in similar mass intervals (light-orange triangles and dashed line:  $9.77 < \log(M/M_{\odot}) < 10.77$ ; pink triangles and dashed line:  $\log(M/M_{\odot}) > 10.77$ ).

$z \sim 2.5$ , to decrease at higher redshifts. The SF-AGN(SB) and SF-AGN(Spiral) contributions to  $\rho_{\text{IR}}$  show opposite trends, with the former sharply increasing towards the higher redshifts (dominating at  $z > 2$ ), and the latter prevailing between  $z \sim 1$  and  $\sim 2$ , then dropping at higher redshifts. AGN1 and AGN2 start dominating the IR luminosity density at  $z \gtrsim 2.5$ , with their  $\rho_{\text{IR}}$  always rising from  $z \sim 0$ , and then remaining almost constant (or slightly decreasing) towards the higher redshifts. Note how these two populations of AGN evolve similarly, as an indication of their same intrinsic nature and of the absence of any significant bias in the far-IR selection.

The contributions to  $\rho_{\text{IR}}$  of MS and off-MS sources (pink and yellow filled regions, respectively, in the bottom-middle panel of Fig. 18) keep nearly constant between  $z \sim 0.8$  and  $z \sim 2.2$ . In particular, the off-MS sources contribution keeps around 20 per cent of the total  $\rho_{\text{IR}}$  over the whole  $0.8 < z < 2.2$  redshift interval, showing no significant signs of increase (or decrease). Our results strengthen

the role of MS sources (pink shaded regions) in the build up of the stellar mass in galaxies, at all cosmic epochs, with evidence that their role is even increasing from  $z \sim 2$  to  $z \sim 1$ : their number density changes by a factor of  $\sim 2$ , while their luminosity/SFR density remains nearly constant. The importance of the off-MS sources does not show any significant signs of decreasing at lower  $z$ , their relative (with respect to the total) number (luminosity) density passing from  $\sim 9$  per cent (22 per cent) at  $z \sim 2$  to  $\sim 6$  per cent (19 per cent) at  $z \sim 1$ . These fractions are relatively different from those found by Rodighiero et al. (2011) (off-MS galaxies represent only 2 per cent of mass-selected star-forming galaxies and account for only 10 per cent of the cosmic SFR density at  $z \sim 2$ ). However, we must note that Rodighiero et al. (2011) for their analysis combined far-IR-selected (i.e. SFR-selected) and near-IR-selected (i.e.  $M_{*}$ -selected) star-forming samples, well defining the MS, while with our data (SFR-selected only), we are not able to observe any



correlation between SFR and stellar mass (see Fig. 15) and barely detect MS objects at  $z \sim 2$ .

Our results have been compared to the SFR densities (converted to  $\rho_{\text{IR}}$  using the Kennicutt 1998 relation) for on-MS and off-MS sources based on the Sargent et al. (2012) model recently derived by Bethermin et al. (2012). These are shown in Fig. 18 as purple and orange dashed lines, respectively. The predicted off-MS  $\rho_{\text{SFR}}$  agrees well with our estimate in the common redshift range, while the predicted one for MS sources is higher than that derived from our data (especially at  $z \sim 1.5$ ). As already discussed regarding the comparison with the Sargent et al. (2012) model, this discrepancy is likely to be ascribed to our difficulty to extrapolate the MS to low-SFR values and to the different selection criteria used to separate MS from off-MS sources.

In the bottom-right panels of Fig. 18, we show the contribution of the different mass populations to the luminosity density as a function of redshift. Although we detect a similar steep increase of  $\rho_{\text{IR}}$  versus redshift at  $z \lesssim 1$  in both low- and high-mass galaxies, the evolution in  $\rho_{\text{IR}}$  of galaxies with different masses is very different, reflecting the downsizing scenario, with  $\rho_{\text{IR}}$  peaking at higher redshift with increasing mass. Indeed, the IR luminosity density of intermediate-mass objects [ $\log(M/M_{\odot}) = 10\text{--}11$ ] always dominates, increasing up to  $z \sim 1$ , then remaining nearly constant at higher redshifts (at least up to  $z \sim 2.8$ ). The IR luminosity density of most massive objects increases even more rapidly with redshift (at  $z = 2$  it was approximately five times higher than today) and continues to grow up to  $z = 3$ , where their contribution to  $\rho_{\text{IR}}$  is  $\sim 30$  per cent of the total and close to that of intermediate-mass objects (which contribute  $\sim 60$  per cent at  $z > 3$ ). We compare our results with those of Santini et al. (2009), plotted in the figure as thick dashed lines [light orange:  $9.77 < \log(M/M_{\odot}) < 10.77$ ; pink:  $\log(M/M_{\odot}) > 10.77$ ; with a Chabrier IMF used to determine our masses], showing very similar trends and values for both intermediate- and higher mass galaxies. Our analysis of high-mass galaxies extends up to  $z \sim 4$ , finding that for the most massive galaxies  $\rho_{\text{IR}}$  continues to rise even at  $z \geq 2$ , with an apparent peak at  $z = 3$ . This result confirms that the formation epoch of galaxies proceeded from high- to low-mass systems.

The values of  $\rho_{\text{IR}}$  in the different redshift intervals, either the total ones or the contributions from the different classes (SED, mass, sSFR), are reported in Table 9.

## 5 DISCUSSION

In the previous sections, we have discussed the different evolutionary behaviour of different classes of sources, either divided by SED-type, mass or sSFR. In this section, we will try to understand ‘who is who’, discussing which populations are mainly on-MS or off-MS, which have the larger (smaller) masses, and how and if the relative contributions of these populations vary with redshift. From Fig. 15, we note that the off-MS sources are dominated by galaxies with AGN-type SEDs. In the lower redshift bin considered, MS sources are mainly spirals and SF-AGN(Spiral), with a small tail of these populations contributing also to the off-MS. AGN1 and AGN2 are prevalently 0.6 dex above the MS (off-MS). Although the mass estimate of AGN1 suffers from the largest uncertainties, our result suggests that the off-MS population is largely constituted by sources containing an AGN, with a higher fraction of AGN-dominated objects at higher  $z$ . This should indicate that the major merger episode likely associated with what is considered a different mode of SF (e.g. Wuyts et al. 2011 finds that off-MS galaxies are likely mergers from their Sérsic index) could also trigger an intense

Table 9. PEP total IR luminosity density.

	$0.0 \leq z < 0.3$	$0.3 \leq z < 0.45$	$0.45 \leq z < 0.6$	$0.6 \leq z < 0.8$	$0.8 \leq z < 1.0$	$1.0 \leq z < 1.2$	$1.2 \leq z < 1.7$	$1.7 \leq z < 2.0$	$2.0 \leq z < 2.5$	$2.5 \leq z < 3.0$	$3.0 \leq z < 4.2$
TOTAL	1.36 ± 0.29	2.25 ± 0.18	2.82 ± 0.32	4.17 ± 0.58	6.61 ± 0.83	9.02 ± 0.95	8.39 ± 0.73	7.85 ± 0.47	7.06 ± 1.75	7.80 ± 3.33	2.50 ± 1.78
Spiral	1.00 ± 0.04	1.39 ± 0.07	1.68 ± 0.12	2.02 ± 0.15	0.98 ± 0.09	0.94 ± 0.10	0.32 ± 0.03	0.78 ± 0.12	1.55 ± 0.32	0.40 ± 0.13	
Starburst	0.05 ± 0.01	0.06 ± 0.01	0.10 ± 0.02	0.18 ± 0.03	0.54 ± 0.04	0.77 ± 0.13	0.72 ± 0.07	0.78 ± 0.12	1.55 ± 0.32	0.40 ± 0.13	
SF-AGN	0.47 ± 0.01	1.03 ± 0.04	1.52 ± 0.06	2.28 ± 0.12	2.82 ± 0.12	3.87 ± 0.36	2.28 ± 0.09	2.75 ± 0.23	5.11 ± 0.60	3.07 ± 0.58	1.29 ± 0.49
AGN2	0.02 ± 0.01	0.012 ± 0.004	0.04 ± 0.01	0.08 ± 0.04	0.03 ± 0.01	0.08 ± 0.02	0.25 ± 0.10	0.60 ± 0.17	0.47 ± 0.22	1.21 ± 0.31	0.39 ± 0.17
AGN1	0.025 ± 0.009	0.029 ± 0.007	0.04 ± 0.01	0.07 ± 0.02	0.05 ± 0.02	0.12 ± 0.10	0.44 ± 0.06	0.59 ± 0.08	1.25 ± 0.18	2.07 ± 0.59	1.28 ± 0.82
SF-AGN(SB)	0.06 ± 0.04	0.06 ± 0.01	0.10 ± 0.01	0.23 ± 0.03	0.46 ± 0.05	1.05 ± 0.15	0.84 ± 0.06	1.12 ± 0.12	3.83 ± 0.74	2.35 ± 0.62	0.92 ± 0.75
SF-AGN(Spiral)	0.40 ± 0.02	0.60 ± 0.05	0.87 ± 0.01	1.56 ± 0.18	1.26 ± 0.16	2.23 ± 0.38	2.49 ± 0.29	0.38 ± 0.08	0.88 ± 0.55	0.73 ± 0.32	
$\log(M/M_{\odot}) = 8.5\text{--}10$	0.34 ± 0.05	0.74 ± 0.36	0.91 ± 0.44	1.11 ± 0.35	1.01 ± 0.71	1.21 ± 0.91	1.02 ± 0.52	2.28 ± 0.41	3.18 ± 0.61	4.47 ± 2.69	1.48 ± 0.71
$\log(M/M_{\odot}) = 10\text{--}11$	0.99 ± 0.08	1.65 ± 0.21	2.14 ± 0.40	3.54 ± 0.75	2.94 ± 0.52	4.05 ± 0.90	4.18 ± 1.85	2.28 ± 0.41	3.18 ± 0.61	4.47 ± 2.69	1.48 ± 0.71
$\log(M/M_{\odot}) = 11\text{--}12$	0.08 ± 0.05	0.26 ± 0.06	0.23 ± 0.12	0.31 ± 0.18	0.63 ± 0.07	0.71 ± 0.31	0.85 ± 0.20	0.82 ± 0.22	1.23 ± 0.46	2.82 ± 2.24	0.34 ± 0.10
$0.8 < z < 2.2$		1.25 < z < 1.8	1.8 > z < 2.2								
On-MS	5.71 ± 1.01	4.02 ± 1.27	7.12 ± 5.03								
Off-MS	1.41 ± 0.15	1.19 ± 0.58	2.01 ± 0.65								

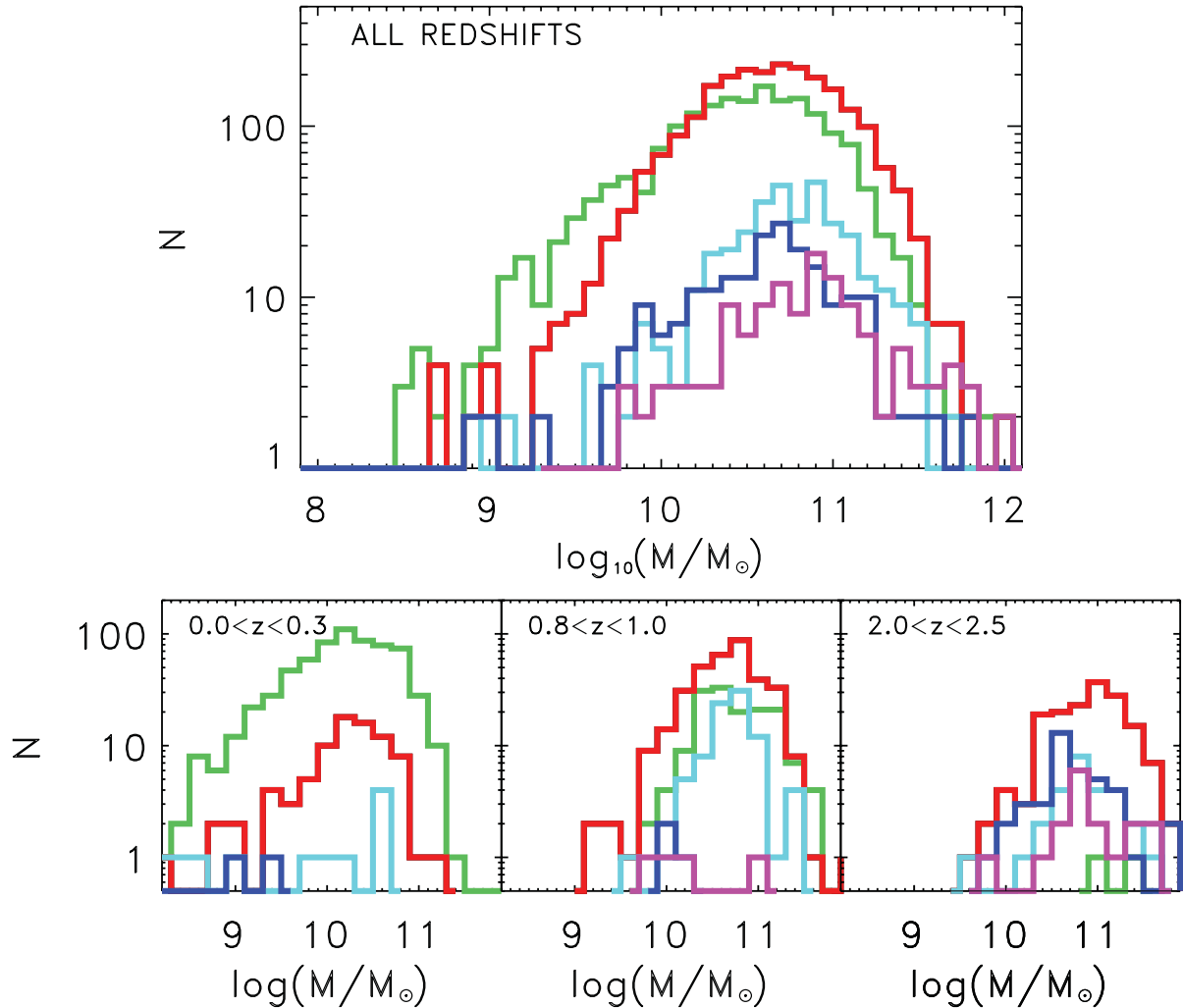


**Figure 19.** Mass distribution of the PEP 160- $\mu\text{m}$  sources in all the four PEP fields, with different colours corresponding to different SED-classes (green, spiral; cyan, starburst; red, SF-AGN; magenta, AGN2; and blue, AGN1). The top panel shows the mass distribution of the different IR populations at all redshifts, while the bottom panels report the mass distribution in three representative redshift bins ( $0 < z < 0.3$ ,  $0.8 < z < 1.0$  and  $2.0 < z < 2.5$ ).

AGN activity, whose presence strongly influences the SFR within the host galaxy. While AGN show preferentially high sSFRs, in our sample they do not seem to prefer higher mass systems (see Fig. 19). Keeping in mind that the masses in our AGN1 objects are affected by large uncertainties, we can interpret this as due to the fact that ours is a selection in SFR. Therefore, our AGN are still in an intense SF phase, where they are still accreting their stellar mass by actively forming stars. Due to the far-IR selection, in fact, we miss the further phase of quiescent, more massive population, with the SF totally quenched and all the stellar mass already formed and in place. Moreover, our result is not in conflict with the consensus in the literature (i.e. that X-ray AGN above a certain X-ray luminosity do prefer massive galaxies), since our classification is not in AGN luminosity cut, but more a cut in  $L_{\text{AGN}}/L_{\text{SF}}$  ratio. The recent result of Mullaney et al. (2012), that  $L_{\text{X}}/L_{\text{IR}}$  (which is a proxy of  $L_{\text{AGN}}/L_{\text{SF}}$ ) is on average almost independent of stellar mass, implies that our selected AGN are not necessarily hosted by very massive galaxies, as indeed we find.

Our results seem to confirm those of Santini et al. (2012), finding evidence of a higher average SF activity in AGN hosts with respect to inactive galaxies and a more pronounced level of SF enhancement in the hosts of luminous AGN (i.e. our AGN1 and AGN2).

Most of the starburst galaxies (i.e. with SEDs fitted by local “starburst” templates) are classified on-MS at any redshifts, though they are always in the region between the MS and the threshold. The starburst population seems to enhance its sSFR from  $z \sim 2$  to  $z \sim 1$ , occupying the region around the MS at higher  $z$  and shifting to higher SFRs (peaking at approximately two times the MS) at lower  $z$ . The bulk of the spiral population remains around the MS at all redshifts, although they almost disappear from our sample at  $z \sim 2$ . From Fig. 15 we also note that while the SF-AGN population as a whole occupies both the loci of MS and off-MS sources, when divided into SF-AGN(SB) and SF-AGN(Spiral), it shows a very clear segregation (suggesting a different mode of SF for the two sub-classes). In fact, SF-AGN(SB) are mainly concentrated in the off-MS region, while the bulk of the SF-AGN(Spiral) is on-MS.

If we mix together all the ‘ingredients’ presented above, we can try to give a global interpretation to our results in terms of galaxy evolution. In agreement with other *Herschel* findings (i.e. Shao et al. 2010; Lapi et al. 2011; Mullaney et al. 2012; Page et al. 2012; Rosario et al. 2012; Santini et al. 2012), we propose the following twofold evolutionary scenario for galaxies and AGN (sketched in a cartoon in Fig. 20).

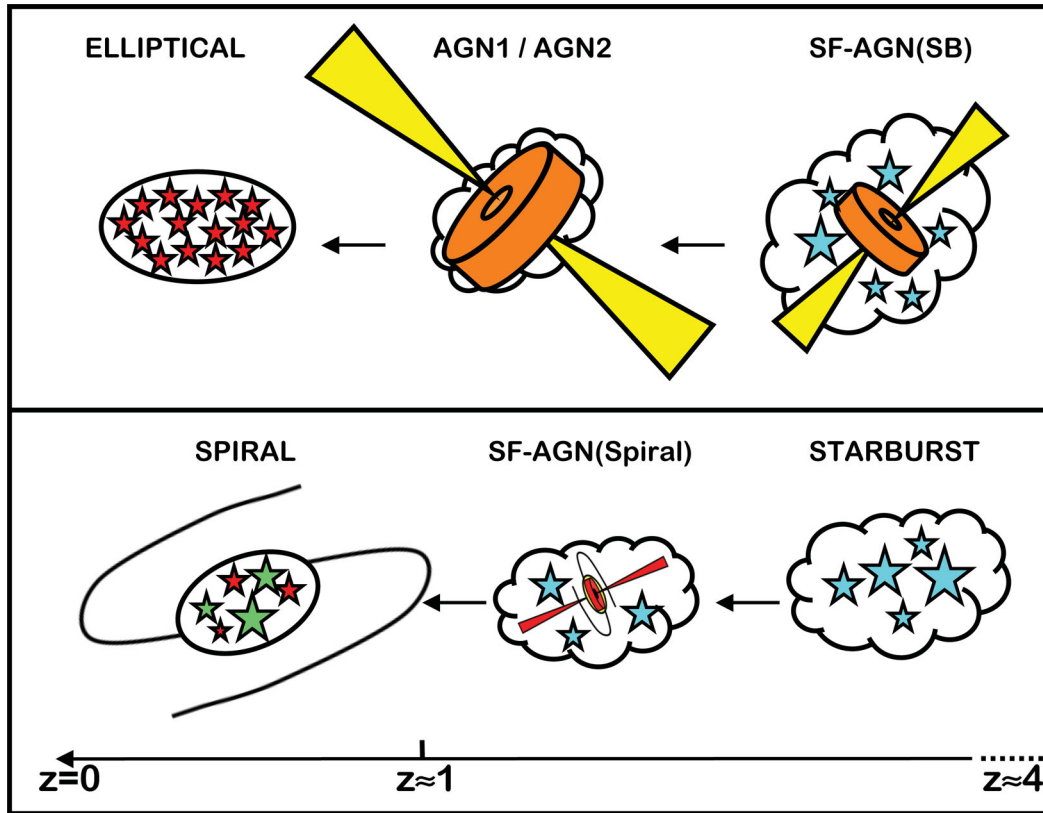


**Figure 20.** A cartoon showing a possible evolutionary scenario involving AGN and star-forming galaxies and leading to the formation, on the one hand, of local elliptical galaxies, on the other hand, of local spiral galaxies. Top: a strong starburst with a growing BH inside [SF-AGN(SB)] transforms into an AGN (either AGN1 or AGN2, depending on orientation) when the BH mass and AGN luminosity have grown enough and the SF is likely to be quenched by feedback processes. Thereafter, the galaxy evolves passively towards a local elliptical. Bottom: the initial moderate starburst (starburst, lasting a typical time of  $\sim$  few  $10^8$  yr) transforms in a less intense starburst also fuelling a low-luminosity AGN [SF-AGN(Spiral)], which starts to reveal itself when the starburst activity is fading. Once the AGN is triggered, it heats the dust resulting in an increase in the mid-IR luminosity (flattening of the SED between 3 and 8  $\mu$ m). The SF-AGN(Spiral) system could last about seven times longer than the pure starburst phase before becoming a steady spiral galaxy (spiral).

(i) On the one hand, we observe that the sources with AGN-dominated SEDs (either AGN1 or AGN2) and those with a starburst-like SED, but containing a non-dominant AGN [SF-AGN(SB)] have a peak in number and luminosity density at  $z \sim 2-2.5$ , dominating at higher redshifts and rapidly decreasing at lower  $z$ . The evolution of AGN1 and AGN2, both in luminosity and in density, is very similar, suggesting the same nature for type 1 and 2 AGN, and the unbiased power of observations in the far-IR band towards orientation/obscuration (affecting both optical and X-ray observations). While dominating the mid-IR part of the SED of these objects, the AGN is not able to explain the high observed far-IR emission, which is mostly powered by SF (as for the SF-AGN(SB) population, where the AGN never dominates the energetic output, probably due to dust-obscuration). The hosts of these AGN appear to form stars in a very efficient way, placing a large fraction of them above the known stellar mass–SFR MS (see Fig. 15). AGN1, AGN2 and SF-AGN(SB) are likely the progenitors of the elliptical galaxies observed nowadays in optical and near-IR surveys, forming through an intense burst of SF occurring during major mergers or in dense nuclear star-forming regions (Granato et al. 2001; Daddi et al. 2010; Wuyts et al. 2011), and then followed by a phase of nuclear activity during which their Super Massive Black Holes (SMBHs) grow (i.e. Hopkins et al. 2008a,b; Lapi et al. 2011). It is generally agreed that the SMBHs and their host galaxies are tightly related, with major mergers being considered the likely process responsible for

transporting large amount of gas towards the centre of the merging system, feeding the SMBH and triggering the SF activity. After the intense starburst phase, the AGN are believed to suppress the SF (i.e. Di Matteo, Springel & Hernquist 2005), so that the remnant quickly evolves to a red massive spheroid. This picture is strongly supported by the recent *Herschel* results from PEP (Rosario et al. 2012), HerMES (Page et al. 2012; Harrison et al. 2012) and H-ATLAS (Lapi et al. 2011) surveys. The latter work, in particular, has shown that the bright-end of the IR LFs and counts at high redshift ( $> 1.5$ ) are consistent with the picture (e.g. Granato et al. 2001) predicting the presence of a population of strongly obscured, star-forming galaxies with SED appreciably different from those of the local starbursts. X-ray and mid-IR spectroscopic observations (e.g. Alexander et al. 2005; Mullaney et al. 2012) of sub-mm selected sources have revealed in many of them the presence of a growing SMBH, powering an obscured AGN. In this framework, the most likely evolutionary path envisages first an SF-AGN(SB) phase (star-forming galaxy with a growing SMBH inside), then an AGN-dominated phase, and finally the formation of an elliptical galaxy in passive evolution.

(ii) On the other hand, we observe that a significant fraction of our IR-selected sources is constituted by moderately star-forming galaxies characterized by an SED similar to that of spiral galaxies, but also suggesting the presence of a low-luminosity AGN [SF-AGN(Spiral)], best fitted by local Seyfert 1.8/2 templates. The bulk

of these objects and their principal contribution to  $\rho_{\text{IR}}$  are at intermediate redshifts ( $1 \lesssim z \lesssim 2$ ), while they decrease between  $z \sim 1$  and  $z = 0$ , as the spiral population rises. Most of the SF-AGN(Spiral)-, spiral- and starburst-SED galaxies occupy the region around the SFR–stellar mass MS at any redshifts, suggesting a steady mode of SF rather than a ‘starburst’ one for these three populations, whose evolution is likely connected. Indeed, Mullaney et al. (2012) have recently shown that at least up to  $z \sim 2$ , SMBHs have grown together with their host galaxies in star-forming galaxies, irrespective of host galaxy mass and triggering mechanism. Given the number densities (Fig. 18), evolutionary trends (Fig. 11), SFRs and masses (Figs 15 and 19) of the SF-AGN(Spiral), starburst and spiral populations, we suggest that these three classes of objects might constitute different phases in the life of a galaxy undergoing secular evolution. The gas in moderate starburst galaxies, undergoing a burst of enhanced SF due either to gravitational interactions or disc instabilities (typical burst duration time of the order of a few  $10^8$  yr), might also fuel a low-luminosity AGN, which starts to reveal itself when the starburst activity is fading. Given the relatively high stellar masses found for the bulk of the SF-AGN(Spiral) [ $\log(M/M_{\odot}) \sim 10$ –11, see Fig. 15], and the almost constant  $M_{\text{BH}}/M_{*}$  ratio (of  $\sim 1-2 \times 10^{-3}$ ) recently suggested by Mullaney et al. (2012) for all the  $0.5 < z < 2.5$  star-forming galaxies, they are likely to contain relatively massive BHs ( $M_{\text{BH}} \sim 10^7$ – $10^8 M_{\odot}$ ). They can therefore have either low values of their radiative efficiency or low values of their accretion mass rate  $\dot{m}$  ( $\dot{m} = \dot{M}/\dot{M}_{\text{Edd}} < 0.01$ ). AGN with low radiative efficiency or low accretion mass rates are generally called radiatively inefficient accretion flows (Narayan et al. 1995), which include also the advection-dominated accretion flow (Narayan 1994). Low  $\dot{m}$  AGN are more difficult to detect, since they often are less luminous than their hosts. Because of this, the nuclear emission is diluted by the host galaxy’s emission and many of them are likely to be classified as ‘normal galaxies’ in most surveys if the AGN luminosity is less than that of the host (e.g. Hopkins et al. 2009). Given the relative number densities of the starburst and SF-AGN(Spiral) populations at  $1 < z < 2$ , we hypothesize a typical duration of the SF-AGN(Spiral) phase about seven times longer than the starburst one (typical burst duration  $\sim 10^8$  yr). Then, after a typical time of  $\sim 7 \times 10^8$  yr, the AGN activity stops and these objects, whose number density decreases at  $z \lesssim 1$ , are likely to become steady spiral galaxies (rapidly increasing between  $z \sim 1$  and  $z = 0$ ) at lower redshifts.

## 6 CONCLUSIONS

We have used the 70-, 100-, 160-, 250-, 350- and 500- $\mu\text{m}$  data from the cosmological guaranteed time *Herschel* surveys, PEP and HerMES, in the GOODS-S and -N, ECFDS and COSMOS, to characterize the evolution of the IR LF and luminosity density of PACS-selected sources across the redshift range  $0 \lesssim z \lesssim 4$ . Evolution is well constrained by our data up to  $z \sim 3$ , and strong hints of evolution are derived at  $3 < z < 4$ . In this work, we have:

(i) completely characterized the multiwavelength SEDs of the PEP sources by performing a detailed SED-fitting analysis and a comparison with known template library of IR populations. Sources have been classified, based on their broad-band SEDs, in five main classes: spiral, starburst, SF-AGN, AGN1 and AGN2.

(ii) computed the rest-frame LFs at 35, 60 and 90  $\mu\text{m}$  up to  $z \sim 4$  from the 70-, 100- and 160- $\mu\text{m}$  selected samples, respectively.

(iii) integrated the SEDs over  $\lambda_{\text{rest}} = 8$ –1000  $\mu\text{m}$  and computed the total IR LF up to  $z \sim 4$  and studied its evolution with redshift,

finding strong luminosity evolution  $\propto (1+z)^{3.55 \pm 0.10}$  up to  $z \sim 1.85$ , and  $\propto (1+z)^{1.62 \pm 0.51}$  between  $z \sim 1.85$  and  $z \sim 4$ , combined with a negative density evolution  $\propto (1+z)^{-0.57 \pm 0.22}$  up to  $z \sim 1.1$  and  $\propto (1+z)^{-3.92 \pm 0.34}$  at  $z > 1.1$  and up to  $z \sim 4$ .

(iv) derived the evolution of the comoving total IR luminosity density, which is found to increase as  $(1+z)^{3.0 \pm 0.2}$  up to  $z \sim 1.1$ , then to remain nearly constant [decrease as  $(1+z)^{-0.3 \pm 0.1}$ ] from  $z \sim 1.1$  to  $z \sim 2.8$ , and to decrease as  $(1+z)^{-6.0 \pm 0.9}$  up to  $z \sim 4$ .

(v) found that the evolution derived for the global IR LF is indeed a combination of different evolutionary paths: the IR population does not evolve all together ‘as a whole’, as is often assumed in the literature, but is composed of different galaxy classes evolving differently: the spiral-SED galaxies dominate  $\rho_{\text{IR}}$  only at low redshifts ( $z \lesssim 0.5$ – $0.6$ ), then SF-AGN dominate up to  $z \sim 2.5$ , while AGN1 and AGN2 start dominating the IR luminosity density only at  $z \gtrsim 2.5$ .

(vi) derived the relative contribution to  $\rho_{\text{IR}}$  of MS and off-MS sources, which keep nearly constant between  $z \sim 0.8$  and  $z \sim 2.2$ , with the MS population always dominating. The contribution to  $\rho_{\text{IR}}$  of the off-MS sources shows no significant signs of increase with  $z$  (from  $\sim 19$  per cent at  $z \sim 0.8$ – $1.25$  to  $\gtrsim 22$  per cent at  $z \sim 1.8$ – $2.2$ ).

(vii) derived very different evolutionary behaviour in terms of different contributions to  $\rho_{\text{IR}}$ , for galaxies with different masses, reflecting the downsizing scenario ( $\rho_{\text{IR}}$  peaks at higher redshift with increasing mass). Intermediate-mass objects [ $\log(M/M_{\odot}) = 10$ –11] always dominate the IR luminosity density, increasing with redshift up to  $z \sim 1$ , then remaining nearly constant at higher redshifts (at least up to  $z \sim 2.8$ ), while the contribution of most massive objects increases even more rapidly with  $z$  (at  $z \sim 2$  it was approximately five times higher than today) and continues to grow up to  $z \sim 3$ .

(viii) described a possible twofold evolutionary scenario for IR sources: on the one hand, AGN1 and AGN2, representing the same population, after an intense starburst phase (due to a major merging event, appearing as SF-AGN(SB) SED galaxies), suppress the SF (and shine as AGN) and evolve to red massive spheroids; on the other hand, the SF-AGN(Spiral) galaxies represent a phase in the life of a star-forming galaxy, following a moderate burst of SF (starburst, with SEDs like those of local starburst galaxies) and preceding the formation of a steady spiral galaxy as we observed in the local Universe.

## ACKNOWLEDGEMENTS

PACS has been developed by a consortium of institutes led by MPE (Germany) and including: UVIE (Austria); KU Leuven, CSL, IMEC (Belgium); CEA, LAM (France); MPIA (Germany); INAF-IFSI/OAA/OAP/OAT, LENS, SISSA (Italy); and IAC (Spain). This development has been supported by the funding agencies BMVIT (Austria), ESA-PRODEX (Belgium), CEA/CNES (France), DLR (Germany), ASI/INAF (Italy) and CICYT/MCYT (Spain). SPIRE has been developed by a consortium of institutes led by Cardiff Univ. (UK) and including: Univ. Lethbridge (Canada); NAOC (China); CEA, LAM (France); IFSI, Univ. Padua (Italy); IAC (Spain); Stockholm Observatory (Sweden); Imperial College London, RAL, UCL-MSSL, UKATC, Univ. Sussex (UK) and Caltech, JPL, NHSC, Univ. Colorado (USA). This development has been supported by national funding agencies: CSA (Canada); NAOC (China); CEA, CNES, CNRS (France); ASI (Italy); MCINN (Spain); SNSB (Sweden); STFC, UKSA (UK) and NASA (USA). CG and FP acknowledge financial contribution from the contracts PRIN-INAF 1.06.09.05 and ASI-INAF I00507/1 and I005110. PM thanks the University of



Trieste for the grant FRA2009. The authors thank an anonymous referee for the helpful comments that greatly improved the quality of the paper.

## REFERENCES

- Alexander D. M., Smail I., Bauer F. E., Chapman S. C., Blain A. W., Brandt W. N., Ivison R. J., 2005, *Nat*, 434, 738
- Arnouts S. et al., 2002, *MNRAS*, 329, 355
- Avni Y., Bahcall J. N., 1980, *ApJ*, 235, 694
- Balestra I. et al., 2010, *A&A*, 512, A12
- Barger A. J., Cowie L. L., Wang W., 2008, *ApJ*, 689, 687
- Berta S., 2005, PhD thesis, Univ. Padua
- Berta S., Fritz J., Franceschini A., Bressan A., Pernechele C., 2003, *A&A*, 403, 119
- Berta S. et al., 2010, *A&A*, 518, L30
- Berta S. et al., 2011, *A&A*, 532, 49
- Berta S. et al., 2013, *A&A*, 551, 100
- Bethermin M., Dole H., Cousin M., Bavouzet N., 2010, *A&A*, 516, A43
- Bethermin M., Dole H., Lagache G., Le Borgne D., Penin A., 2011, *A&A*, 529, A4
- Bethermin M. et al., 2012, *ApJ*, 757, L23
- Bolzonella M., Miralles J.-M., Pelló R., 2000, *A&A*, 363, 474
- Bongiorno A. et al., 2012, *MNRAS*, 427, 3103
- Brusa M. et al., 2009, *ApJ*, 693, 8
- Bruzual G., Charlot S., 2003, *MNRAS*, 344, 1000
- Bunker A. J., Stanway E. R., Ellis R. S., Mc Mahon R. G., McCarthy P. J., 2003, *MNRAS*, 342, L47
- Caputi K. I. et al., 2007, *ApJ*, 660, 97
- Cardamone C. N. et al., 2010, *ApJS*, 189, 270
- Chapman S. C., Blain A. W., Smail I., Ivison R. J., 2005, *ApJ*, 622, 772
- Chary R. R., Elbaz D., 2001, *ApJ*, 556, 562
- Ciliegi P., Gruppioni C., McMahon R., Rowan-Robinson M., 2001, *Ap&SS*, 276, 957
- Civano F. et al., 2011, *ApJ*, 741, 91
- Cohen J. G. et al., 2000, *ApJ*, 538, 29
- Colavitti E., Matteucci F., Murante G., 2008, *A&A*, 483, 401
- Cooper M. C. et al., 2012, *MNRAS*, 425, 2116
- Cowie L. L., Barger A. J., Hu E. M., Capak P., Songalia A., 2004, *AJ*, 127, 3137
- Cristiani S. et al., 2000, *A&A*, 359, 489
- Croom S. M., Warren S. J., Glazebrook K., 2001, *MNRAS*, 328, 150
- da Cunha E., Charlot S., Elbaz D., 2008, *MNRAS*, 388, 1595
- da Cunha E., Eminian C., Charlot S., Blaizot J., 2010, *MNRAS*, 403, 1894
- Daddi E. et al., 2007, *ApJ*, 670, 156
- Daddi E. et al., 2010, *ApJ*, 714, L118
- Di Matteo T., Springel V., Hernquist L., 2005, *Nat*, 443, 604
- Dickinson M. et al., 2004, *ApJ*, 600, L99
- Doherty M., Bunker A. J., Ellis R. S., McCarthy P. J., 2005, *MNRAS*, 361, 525
- Domínguez-Sánchez H. et al., 2011, *MNRAS*, 417, 900
- Drory N. et al., 2003, *ApJ*, 595, 698
- Dunne L. et al., 2011, *MNRAS*, 417, 1510
- Eales S. et al., 2010, *PASP*, 122, 499
- Elbaz D. et al., 1999, *A&A*, 351, L37
- Elbaz D. et al., 2007, *A&A*, 468, 33
- Elbaz D. et al., 2010, *A&A*, 518, L29
- Elbaz D. et al., 2011, *A&A*, 533, 119
- Farrar D., Afonso J., Efstathiou A., Rowan-Robinson M., Fox M., Clements D., 2003, *MNRAS*, 343, 585
- Feltre A., Hatziminaoglou E., Fritz J., Franceschini A., 2012, *MNRAS*, 426, 120
- Fontana A. et al., 2004, *A&A*, 424, 23
- Fontanot F., Cristiani S., Santini P., Fontana A., Grazian A., Somerville R. S., 2012, *MNRAS*, 421, 241
- Fritz J., Franceschini A., Hatziminaoglou E., 2006, *MNRAS*, 366, 767
- Genzel R., Cesarsky C., 2000, *ARA&A*, 38, 761
- Granato G. L., Silva L., Monaco P., Panuzzo P., Salucci P., De Zotti G., Danese L., 2001, *MNRAS*, 324, 757
- Grazian A. et al., 2006, *A&A*, 449, 951
- Griffin M. et al., 2010, *A&A*, 518, L3
- Gruppioni C., Lari C., Pozzi F., Zamorani G., Franceschini A., Oliver S., Rowan-Robinson M., Serjeant S., 2002, *MNRAS*, 335, 831
- Gruppioni C. et al., 2008, *ApJ*, 684, 136
- Gruppioni C. et al., 2010, *A&A*, 518, L27
- Harrison C. M. et al., 2012, *ApJ*, 760, L15
- Hauser M. G., Dwek E., 2001, *ARA&A*, 39, 249
- Hopkins P. F., Hernquist L., Cox T. J., Kereš D., 2008a, *ApJS*, 175, 356
- Hopkins P. F., Cox T. J., Kereš D., Hernquist L., 2008b, *ApJS*, 175, 390
- Hopkins P. F., Hickox R., Quataert L., Hernquist L., 2009, *MNRAS*, 398, 333
- Ilbert O. et al., 2004, *MNRAS*, 341, 541
- Ilbert O. et al., 2006, *A&A*, 457, 841
- Ilbert O. et al., 2009, *ApJ*, 690, 1236
- Ilbert O. et al., 2010, *ApJ*, 709, 644
- Ivison R. et al., 2010, *A&A*, 518, 245
- Juneau S. et al., 2005, *ApJ*, 619, L135
- Karim A. et al., 2011, *ApJ*, 730, 61
- Kennicutt R. C., Jr, 1998, *ApJ*, 498, 541
- Kessler M. et al., 1996, *A&A*, 315, L27
- Lapi A. et al., 2011, *ApJ*, 742, 24
- Le Fèvre O. et al., 2005, *A&A*, 439, 845
- Le Floc'h E. et al., 2005, *ApJ*, 632, 169
- Le Floc'h E. et al., 2009, *ApJ*, 703, 222
- Lilly S. J. et al., 2007, *ApJS*, 172, 70
- Lilly S. J. et al., 2009, *ApJS*, 184, 218
- Lutz D. et al., 2011, *A&A*, 532, 90
- Magdis G. E., Elbaz D., Daddi E., Morrison G. E., Dickinson M., Rigopoulou D., Gobat R., Hwang H. S., 2010, *ApJ*, 714, 1740
- Magliocchetti M. et al., 2011, *MNRAS*, 416, 1105
- Magnelli B., Elbaz D., Chary R. R., Dickinson M., Le Borgne D., Frayer D. T., Willmer C. N. A., 2009, *A&A*, 496, 57
- Magnelli B., Elbaz D., Chary R. R., Dickinson M., Le Borgne D., Frayer D. T., Wilmer C. N. A., 2011, *A&A*, 528, A35
- Maraston C., Pforr J., Renzini A., Daddi E., Dickinson M., Cimatti A., Tonini C., 2010, *MNRAS*, 407, 830
- Marsden G. et al., 2011, *MNRAS*, 417, 1192
- Mignoli M. et al., 2005, *A&A*, 437, 883
- Mullaney J. R. et al., 2012, *ApJ*, 753, L30
- Narayan R., Yi I., 1994, *ApJ*, 428, L13
- Narayan R., Yi I., Mahadevan R., 1995, *Nat*, 374, 623
- Neugebauer G. et al., 1984, *ApJ*, 278, L1
- Nordon R. et al., 2010, *A&A*, 518, L24
- Nordon R. et al., 2012, *ApJ*, 745, 182
- Oliver S. et al., 2012, *MNRAS*, 424, 1614
- Page M. et al., 2012, *Nat*, 485, 213
- Pannella M. et al., 2009, *ApJ*, 698, L116
- Papovich C. et al., 2004, *ApJS*, 154, 70
- Patel H., Clements D. L., Vaccari V., Mortlock D. J., Rowan-Robinson M., Pérez-Fourmon I., Afonso-Luis A., 2013, *MNRAS*, 428, 291
- Peng Y. et al., 2010, *ApJ*, 721, 193
- Peng Y., Lilly S. J., Renzini A., Carollo M., 2011, *ApJ*, 757, 4
- Pérez-González P. et al., 2005, *ApJ*, 630, 82
- Pilbratt G. et al., 2010, *A&A*, 518, L1
- Poglitsch A. et al., 2010, *A&A*, 518, L2
- Polletta M. et al., 2007, *ApJ*, 663, 81
- Popesso P. et al., 2009, *A&A*, 494, 443
- Pozzetti L. et al., 2010, *A&A*, 523, 13
- Pozzi F. et al., 2004, *ApJ*, 609, 122
- Reddy N. A., Pettini M., Steidel C. C., Shapley A. E., Erb D. K., Law D. R., 2012, *ApJ*, 754, 25
- Richards G. et al., 2006, *AJ*, 131, 2766
- Rieke G. H., Alonso-Herrero A., Weiner B. J., Pérez-González P. G., Blaylock M., Donley J. L., Marcellac D., 2009, *ApJ*, 692, 556
- Rodighiero G. et al., 2010a, *A&A*, 515, 8



- Rodighiero G. et al., 2010b, *A&A*, 518, L25  
Rodighiero G. et al., 2011, *ApJ*, 739, 40  
Rosario D. J. et al., 2012, *A&A*, 545, 45  
Roseboom I. G. et al., 2010, *MNRAS*, 409, 48  
Sajina A., Yan L., Fadda D., Dasyra K., Huynh M., 2012, *ApJ*, 757, 13  
Sanders D. et al., 2003, *AJ*, 126, 1607  
Santini P. et al., 2009, *A&A*, 504, 751  
Santini P. et al., 2012, *A&A*, 540, 109  
Sargent M. T., Be'thermin M., Daddi E., Elbaz D., 2012, *ApJ*, 747, 31  
Saunders W. et al., 1990, *MNRAS*, 242, 318  
Scarlata C. et al., 2007, *ApJS*, 172, 406  
Schmidt M. et al., 1968, *ApJ*, 151, 393  
Sedgwick C. et al., 2011, *MNRAS*, 416, 1862  
Serjeant S. B. J. et al., 2004, *MNRAS*, 355, 813  
Shao L. et al., 2010, *A&A*, 518, L26  
Smail I., Ivison R. J., Blain A. W., 1997, *ApJ*, 490, L5  
Smit R., Bouwens J. R., Franx M., Illingworth G. D., Labbé I., Oesch P. A., van Dokkum P. G., Pieter G., 2012, *ApJ*, 756, 14  
Smith J. D. T. et al., 2007, *ApJ*, 656, 770  
Stanway E. R. et al., 2004, *ApJ*, 607, 704  
Strolger L. et al., 2004, *ApJ*, 613, 200  
Sutherland W., Saunders W., 1992, *MNRAS*, 259, 413  
Swinbank A. M. et al., 2010, *Nat*, 464, 733  
Szokoly G. P. et al., 2004, *ApJS*, 155, 271  
van der Wel A., Franx M., van Dokkum P. G., Rix H., 2004, *ApJ*, 601, L5  
Vanzella E. et al., 2008, *A&A*, 478, 83  
Wall J. V., Pope A., Scott D., 2008, *MNRAS*, 383, 435  
Werner M. W. et al., 2004, *ApJS*, 154, 1  
Wirth G. D. et al., 2004, *AJ*, 127, 3121  
Wuyts S. et al., 2011, *ApJ*, 742, 96

This paper has been typeset from a  $\text{T}_{\text{E}}\text{X}/\text{L}^{\text{A}}\text{T}_{\text{E}}\text{X}$  file prepared by the author.